



BRNO UNIVERSITY OF TECHNOLOGY

VYSOKÉ UČENÍ TECHNICKÉ V BRNĚ

FACULTY OF ELECTRICAL ENGINEERING AND COMMUNICATION

FAKULTA ELEKTROTECHNIKY
A KOMUNIKAČNÍCH TECHNOLOGIÍ

DEPARTMENT OF RADIO ELECTRONICS

ÚSTAV RADIOELEKTRONIKY

AN OPTICAL D/A CONVERTER FOR VLC APPLICATIONS

OPTICKÝ D/A PŘEVODNÍK PRO VLC APLIKACE

DOCTORAL THESIS

DIZERTAČNÍ PRÁCE

AUTHOR

AUTOR PRÁCE

Ing. Aleš Dobesch

SUPERVISOR

ŠKOLITEL

prof. Ing. Otakar Wilfert, CSc.

BRNO 2017

ABSTRACT

The dissertation deals with the optical digital to analog converter as an alternative transmitter front-end concept for visible light communication applications. The dissertation looks into optical channel modeling and suggests a suitable modeling approach. A significant part devoted to the numerical optical channel modeling reveals the influence of emitter bit depth, emitter array topology and geometrical arrangement on communication system performance. The dissertation deals with optical digital to analog converter design based on previously acquired simulations and explores overall front-end performance. Furthermore, the thesis presents a real time demonstration of high data rate optical communication using the front-end.

KEYWORDS

LED, VLC, ODAC, channel modeling, photo diode, optical modulation, optical receiver.

ABSTRAKT

Disertační práce se zabývá optickým digitálně-analogovým převodníkem, jako alternativou optické části koncové vysílací jednotky (optický front-end) určené pro VLC (visible light communication) aplikace. Stěžejní část práce, která se věnuje numerickému modelování optického kanálu, prezentuje vliv bitové hloubky, topologie koncové části optického vysílače a geometrického uspořádání na přenášený signál. Součástí práce je návrh, realizace a ověření parametrů optického digitálně-analogového převodníku vycházející z předcházejících simulací. V poslední řadě práce obsahuje demonstraci vysokorychlostní optické komunikace s využitím navrženého VLC optického vysílače.

KLÍČOVÁ SLOVA

LED, VLC, ODAC, modelování kanálu, fotodioda, optické modulace, optický přijímač.

DOBESCH, A. An optical D/A converter for VLC applications. Brno: Brno University of Technology, Faculty of Electrical Engineering and Communication, 2017. 102 p. Supervised by Prof. Ing. Otakar Wilfert, CSc.

DECLARATION

I declare that I have written my doctoral thesis on the theme of An optical D/A converter for VLC applications independently, under the guidance of my doctoral thesis supervisor and using the technical literature and other sources of information which are all quoted in the thesis and detailed in the list of literature at the end of the thesis. As the author of the doctoral thesis I furthermore declare that, as regards the creation of this doctoral thesis, I have not infringed any copyright. In particular, I have not unlawfully encroached on anyone's personal and/or ownership rights and I am fully aware of the consequences in the case of breaking Regulation S 11 and the following of the Copyright Act No 121/2000 Sb., and of the rights related to intellectual property right and changes in some Acts (Intellectual Property Act) and formulated in later regulations, inclusive of the possible consequences resulting from the provisions of Criminal Act No 40/2009 Sb., Section 2, Head VI, Part 4.

Brno

.....

(author's signature)

ACKNOWLEDGMENT

I would like to express the deepest appreciation to my supervisor Prof. Ing. Otakar Wilfert, CSc. for the continuous support of my PhD study and related research, for his patience, motivation, and immense knowledge. His guidance helped me in all the time of research and writing of this thesis.

My sincere thanks also goes to my external supervisor Prof. Luis Nero Alves for his valuable assistance and guidance helping me all the time during the research.

Finally, I would like to thank to my family for their continuous support during my studies and for always believing in me.



Faculty of Electrical Engineering and
Communication
Brno University of Technology
Technická 12, CZ-61600 Brno Czech Republic
<http://www.six.feec.vutbr.cz>

ACKNOWLEDGMENT

The described research was performed in laboratories supported by the SIX project; the registration number CZ.1.05/2.1.00/03.0072, the operational program Research and Development for Innovation.

Brno

.....

(author's signature)



EVROPSKÁ UNIE
EVROPSKÝ FOND PRO REGIONÁLNÍ ROZVOJ
INVESTICE DO VAŠÍ BUDOUCNOSTI



Contents

INTRODUCTION	12
1 STATE OF THE ART	13
1.1 Visible light communication	13
1.2 Light sources in VLC	15
1.2.1 VLC emitter architectures	16
1.2.2 Illumination requirements	18
1.3 Optical receiver for VLC applications	20
1.3.1 Photodiode communications	20
1.3.2 Image sensor communications	20
1.4 VLC modulation techniques	22
1.4.1 Pulse modulation techniques	23
1.4.2 Advanced modulation techniques	23
1.5 Optical channel modeling	26
1.5.1 Barry's method	27
1.5.2 DUSTIN algorithm	28
1.5.3 Iterative site-based modeling	28
1.5.4 Monte Carlo ray tracing	28
1.5.5 Ceiling bounce model	28
1.5.6 Curve fitting	29
1.6 VLC performance metrics	30
1.6.1 Channel cut-off frequency	30
1.6.2 Channel delay spread	30
1.6.3 Error vector magnitude	31
1.6.4 Root mean square error	31
1.6.5 Signal to noise ratio	32
1.6.6 Bit error ratio	32
2 OBJECTIVES OF THE THESIS	33
3 VLC SYSTEM MODELING	34
3.1 VLC system models	34
3.1.1 Emitter model	34
3.1.2 Reflection model	36
3.1.3 Receiver model	37
3.2 ODAC LED array arrangements	38
3.3 ODAC-based VLC system performance investigation	41
3.4 Multi-path signal propagation model	45
3.5 Study on utilizing the ODAC concept in ITS applications	49
3.6 ODAC system performance analysis for indoor set-up conditions	55

4	ODAC FRONT-END DESIGN AND PERFORMANCE EVALUATION	64
4.1	VLC ODAC emitter	64
4.1.1	ODAC concept	64
4.1.2	ODAC hardware sample design	65
4.2	VLC optical receiver	66
4.3	Signal reconstruction error performance	67
4.3.1	Static signal reconstruction tests	67
4.3.2	Dynamic signal reconstruction tests	69
4.4	Channel impulse and frequency response	71
4.5	Linearity error performance	73
4.6	Real time FPGA-based VLC system	76
5	CONCLUSION	82
	BIBLIOGRAPHY	88
A	CURRICULUM VITAE	95
B	LIST OF PUBLICATIONS	98
C	LIST OF RESEARCH PRODUCTS	101

List of Figures

1.1	Visible light communication system	13
1.2	VLC emitter	17
1.3	Optical digital-to-analog converter	18
1.4	Light intensity human perception	19
1.5	VLC modulations	22
1.6	Basic VLC modulation techniques	23
1.7	Utilized optical OFDM modulations	24
1.8	Ideal frequency responses and bandwidth requirements for different orders of m-CAP	25
1.9	Basic optical link configurations according to the degree of directionality of the emitter and receiver. Both emitter and the receiver characteristics are outlined.	26
3.1	Normalized shape of the generalized Lambertian radiation pattern	34
3.2	Reflection model	36
3.3	Generalized receiver model	38
3.4	ODAC LED arrays	39
3.5	Near field optical relative intensity displacement	41
3.6	Spectral characteristic of the phosphorus-coated LED	42
3.7	Conceptual system diagram	42
3.8	On axis E_{RMS} performance	44
3.9	Spatial E_{RMS} performance	45
3.10	Conceptual multi-path system diagram	45
3.11	Detailed multi-path system set-up	46
3.12	E_{RMS} performance comparison of 5-bit LED arrays	48
3.13	E_{RMS} performance of 7-bit LED arrays	48
3.14	E_{RMS} performance of 8-bit LED arrays	49
3.15	Crossroad model	50
3.16	General DC channel gain H_G	52
3.17	Signal reconstruction error E_{RMS}	54
3.18	Reconstruction error ($HPA = 30^\circ, FOV 60^\circ$)	55
3.19	System model diagram	56
3.20	Detailed set-up	57
3.21	Channel impulse response (CIR), $HPA45^\circ, FOV60^\circ$	60
3.22	Four luminaires indoor set-up, $HPA 15^\circ$	61
3.23	Four luminaires indoor set-up, $HPA 45^\circ$	62
3.24	$EVM, f = 100\text{MHz}, HPA45^\circ, FOV60^\circ$	62
3.25	$EVM, f = 100\text{MHz}+200\text{MHz}, HPA45^\circ, FOV60^\circ$	63
3.26	EVM frequency dependence	63
4.1	ODAC hardware samples	65
4.2	ODAC front-end electrical driver circuit	66
4.3	Wide-band optical receiver	67
4.4	Static tests set-up	67
4.5	Static signal reconstruction error	69
4.6	Dynamic tests set-up	70
4.7	Dynamic signal reconstruction error	71

4.8	Channel impulse and frequency response	72
4.9	PLCC6 LED and filters optical spectrum characteristics	73
4.10	Blue 7.62mm LED ODAC front-end, $f = 1kHz$	74
4.11	Blue 7.62mm LED ODAC front-end, $f = 98kHz$	75
4.12	White PLCC6 LED ODAC front-end, $f = 1kHz$	75
4.13	Blue 7.62mm LED ODAC front-end, $f = 98kHz$	75
4.14	Real time FPGA-based OFDM VLC system set-up diagram	76
4.15	Experimental test bed	77
4.16	DCO-OFDM signal spectrums	78
4.17	<i>BER</i> performance for increasing distances and bitrates	79
4.18	Achievable datarates for distances from 60cm to 220cm	80
4.19	<i>EVMs</i> and measured illuminance E_v .	80
4.20	Compromise between <i>EVM</i> and clipping level at the transmitter	81

List of Tables

1	Mathematical relations allowing the calculation of the reflection function for various materials according to the angle of incidence α and the angle of observation β [12].	37
2	Transceiver design and implementation parameters	78

INTRODUCTION

In the last few years, general lighting has undoubtedly been one of the most emerging technologies. Light emitting diodes (LEDs) are gradually replacing conventional lighting devices due to their excellent intrinsic characteristics. Among these characteristics, efficacy, relatively long lifetime (the order of 100,000 hours [46]), low cost and enhanced control are perhaps the most relevant aspects which make these devices superior compared to conventional devices such as incandescence or even compact fluorescent lamps. In terms of luminous efficacy, state-of-the-art high power LEDs are now able to exceed 300lm/W for phosphorous coated devices [19]. The immense impact on the lighting industry demonstrates, for instance, the transition to pure LED technology in automotive or in general the lighting industry. A similar trend is obvious in other branches including modern architecture, healthcare, vehicle telematics, security or even agriculture. The accelerated LED production predetermines solid state lighting (SSL) as a future technology for general lighting.

LEDs, organic LEDs (OLEDs) or other LED-based devices in combination with suitable modulation techniques allows to employ them not only for lighting but also for communication purposes. The usage of LEDs as communicating devices was proposed by Nakagawa in 2000 [57]. The technological concept known as visible light communication (VLC) has been associated by the group Visible light communication consortium (VLCC). Afterwards, this communication technology via visible light is better known under the term Light-Fidelity (Li-Fi) coined by prof. Harald Haas [31]. VLC technology, similar in nature to the more mature infra-red (IR) wireless based systems, presents the advantage of exploiting the same device for both lighting and communications means. This way, LEDs are used to convey information, while performing their normal lighting function. The human eye cannot detect fast light fluctuations (more than 200Hz), being sensitive only to average luminous power. Thus, it is possible to modulate the light with fast changing signals.

The huge potential of VLC technology promises a number of practical applications in future communication systems. The connection of lighting and communication seems to be a feasible opportunity for current wireless indoor systems. The most often cited case predisposes VLC as a suitable alternative for Wi-Fi especially in all day illuminated offices. Recently, among the most discussed VLC applications belongs locating and positioning systems. Another significant VLC utilization is relevant in RF restricted areas. As regards to outdoor applications, VLC has a good chance to enhance vehicle telematics, traffic safety and fluency.

The dissertation thesis deals with a VLC system employing a nontraditional transmitter concept based on optical digital to analog conversion (ODAC). Based on a complex numerical

model the thesis examines several possible ODAC-based transmitter architectures suitable for VLC applications. The thesis deeply explores and evaluates several VLC system set-ups ready to use advanced modulation techniques in terms of channel modeling. The experimental part evaluates overall performance of two ODAC samples. Finally, the thesis demonstrates ODAC transmitter performance using a real-time VLC system designed on a field programmable gate array (FPGA).

1 STATE OF THE ART

1.1 Visible light communication

The term optical wireless communication (OWC) is a general name for a wireless communication technology that takes place in the optical domain. The general title OWC comprises a short-range IR communication, free-space optics (FSO) supposed to be utilized for significantly higher distances expanding hundreds of meters to kilometers and VLC suitable for middle-range communications between tens and hundreds of meters. VLC uses visible light as an incoherent light wave carrier simultaneously for data transfer and lighting. A conventional VLC system is depicted in 1.1 uses intensity modulation/direct detection (IM/DD) principles, similarly to former infra-red based communications systems. Basically, a VLC system consists of an emitter employing an LED device as a light emitting source. In high speed optical communication a silicon PIN photodiode typically serves for signal detection having a relatively good responsivity in the visible light area of the electromagnetic spectrum. As a transfer medium, VLC naturally exploits the atmosphere both for outdoor and indoor applications. Nevertheless, presently, the main VLC research branch is primarily focused on indoor VLC applications.

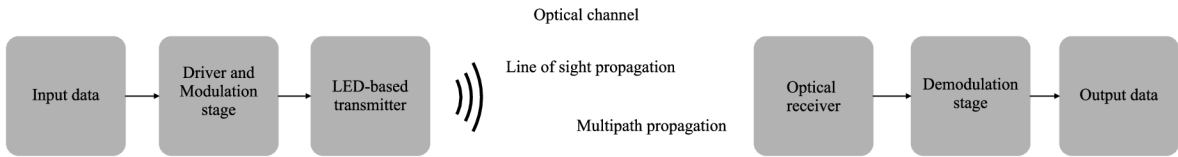


Figure 1.1: Visible light communication system

A well-known scenario of IR communication can be used substantially for VLC channel characterization. In detail, IR channel modeling based on IM/DD was presented by J. Kahn and J. Barry many years ago [10]. The fundamental difference between IR communication and VLC lies in operating wavelengths. Whilst IR communication essentially relies on a single dominant wavelength carrier, in VLC the carrier may utilize the whole visible part of the electromagnetic spectrum. In this case, VLC exhibits a different behavior compared to the former IR communication which results in certain differences on the transmitter side, on the receiver side and also in the channel modeling approach. Perhaps, a wavelength dependent optical channel may be seen as the most relevant difference between IR communication and VLC. On the other hand, VLC in most cases uses the blue component of a common phosphorus-coated LED device occupying a narrow spectral band likewise in IR communication. Other demands purely depend on the emitter and receiver architectures and parameters, thus VLC channel modeling can easily follow the IR channel modeling principles.

VLC standards, summarized in IEEE 802.15.7, describe the VLC physical layer for visible light personal area networks (VPANs). VLC standards established in Japan can be found in the document JEITA CP-1221 [6, 5]. Recently, the IEEE standard is being revised to IEEE 802.15.7r1 in order to include VLC as a part of 5G networks [37, 38].

1.2 Light sources in VLC

Advanced LED technology enabled to use light sources both for illumination and communication. The LED is a solid-state semiconductor device able to directly convert electricity to light. Basically, the LED is a source of incoherent light emitted by spontaneous emission. The fundamental milestone in LED technology is undoubtedly the conversion from the original LED indication function to illumination function. In terms of LED technology, three well known LED categories can be considered, particularly inorganic LEDs, organic LEDs and hybrid LEDs.

Inorganic LED history reaches back to the early 70's when the first inorganic LED was manufactured [48]. For a long time LEDs had the role of indicator devices. Several years back, advanced technology allowed LEDs to be utilized also for illumination purposes. Originally, a white LED was realized by closely putting together a red, blue and green LED, known as an RGB LED. The efficacy is high and the color rendering favorable. However, the major drawback of the RGB LED is their driving complexity, costs and wavelength instability arising from the operational temperature variation. A historic LED technology breakthrough was achieved by using a metal-organic vapor phase epitaxy (MOCVD) process in connection with multiple quantum wells to produce a GaN based blue LED. Therefore, the most common method to achieve white light is to use a GaN-based blue LED in conjunction with the phosphor embedded into epoxy resin. Commercially, the most used phosphor compound is probably Cerium-doped Yttrium aluminum garnet (YAG:Ce) [62]. In terms of VLC, the GaN-based LED is the major candidate for high data rate communication with a modulation bandwidth of several MHz. Moreover, reduction of an LED photo-active area means a modulation bandwidth increase. LED chip active area reduction is the essence of the latest LED technology developed purely for communication purposes, known as micro LED (mLED), offering up to 400MHz of bandwidth [65, 44].

Organic LED seems to be a promising carbon-based LED technology able to outperform conventional inorganic LEDs. This technology offers, among others, very thin, lightweight, flexible, transparent and high efficacy sources of light [47]. Generally, OLEDs can be split into two categories, small molecule LEDs (SMOLEDs) and polymer LEDs (PLEDs). However, the current high cost of OLED technology is preventing wider penetration into the general lighting market. As far as OLED performance is concerned, technology has not matured enough to overcome conventional inorganic LEDs. In terms of VLC applications, the modulation bandwidth is considerably low compared to the inorganic LED. Moreover, OLEDs suffer from lifetime shortage [29].

Hybrid LED is composed both of organic and inorganic compounds. Modern quantum dots LED (QLED) technology is considered as a promising technology of modern displays and general lighting. Basically, it is very similar to OLED technology, however, the light emitting centers consist of quantum dots, in most cases cadmium selenide (CdSe) nanocrystals sandwiched between an organic electron transport layer and a hole transport layer. Concerning QLED properties, they have saturated colors, narrow emission band, pretty high efficacy and are easily spectrally controlled by nanocrystal size. The recent manufacturing process suggests QLEDs to be stamp or ink-jet printed [60]. From the VLC perspective, QLEDs are able to compete with conventional inorganic LEDs [63].

1.2.1 VLC emitter architectures

VLC transmitter front-end (the transmitter part comprising the emitter and optionally optics) undoubtedly belongs to the key part of the whole VLC system. Thus, emitter design must be performed with necessary care. The following figure 1.2a exemplifies a typical VLC emitter. The data to be transmitted is fed to the digital-to-analog converter (DAC). The output analog signal is used to drive an LED or an LED array. LED powering is carried out by a DC bias tee. The use of a conventional DAC to drive LED front-end in VLC systems imposes several drawbacks. Perhaps the most relevant issue arises from the LED's intrinsic characteristic which is demonstrated in figure 1.2b. The output optical power is not proportional to the electrical input. This gives rise to nonlinearities which may limit overall system performance. Meeting driving requirements guarantees the stated device lifetime since constant current conditions are linked to the operating temperature which directly influences LED lifetime [35, 45].

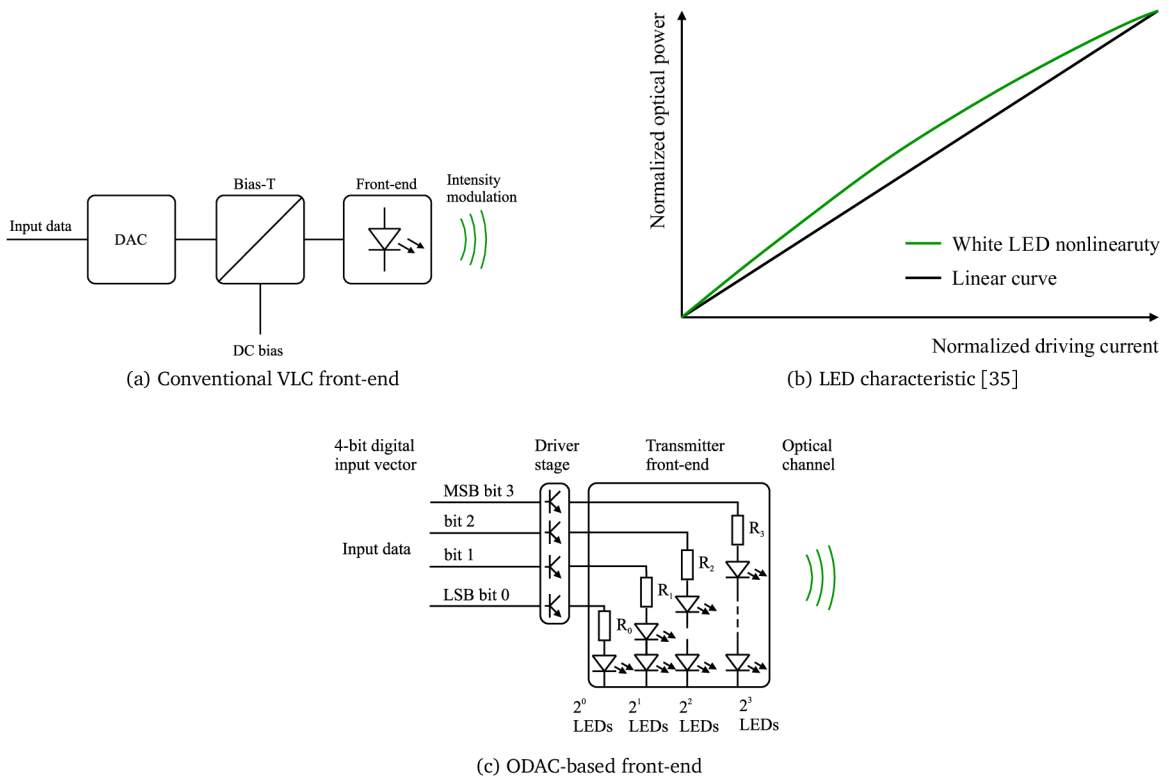


Figure 1.2: VLC emitter

An appropriate solution able to cope with the previously listed constraints can be a transmitter employing an optical digital to analog conversion (ODAC). Essentially, in ODAC, the multiple digital signals are fed to different LED groups inside an array as illustrated in figure 1.2c (for illustration a 4-bit ODAC is considered). Thus, for a communication transmitter, the electrical DAC stage can be removed and the digital outputs can be directly applied to the LED array compared to the conventional driving approach illustrated in figure 1.2a. Two ODAC architectures are possible, either using a fixed number of LEDs per bit (illustrated in figure 1.3a), or using LED groups with a different number of LEDs (depicted in figure 1.3b). In the first case, DAC operation will be achieved by combining the light output of different LED groups driven with different current levels, following the usual distribution of binary weights. In the second architecture, the LEDs are driven with the same current and the binary weights are given by the sum of LEDs in each group.

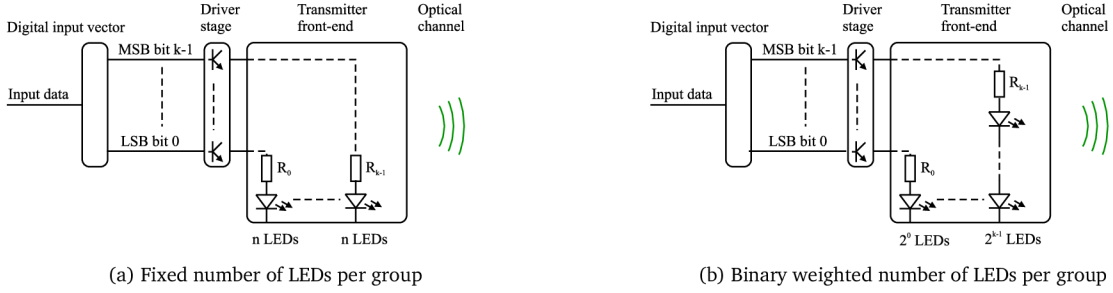


Figure 1.3: Optical digital-to-analog converter

Obviously, the latter approach is more adequate, because it imposes the same operating conditions for all devices in the array. The digital signals interfere in the optical channel and are received as a recovered analog signal on the receiver side. For lighting purposes, this technique may also support dimming. Using the ODAC concept, the non-linearity of the LEDs is effectively removed. Performance is for this case dependent on the bit depth of the converter, quantization error and channel induced effects. This technique also offers another advantage for communication. A recent trend in LEDs is their aggregation in arrays, known as chip-on-board (COB) LEDs which is in line with the proposed ODAC architecture. COB LEDs were developed as a way of increasing LED efficacy. This approach can also be explored as a means to achieve higher bandwidth. In fact, device area and bandwidth are inversely dependent parameters, the higher the area devices have, in this sense the smaller bandwidth is [52]. Despite the fact that the ODAC concept was proposed as a suitable solution how to cope with the LED driving constraints there exist no research deeply looking into the channel modeling of VLC systems employing the ODAC [26, 8].

1.2.2 Illumination requirements

Illuminance E_V and its distribution in the task area influence how effectively and conveniently people are able to perceive and effectively do visual tasks. As the VLC mainly holds the illumination function certain illumination requirements have to be met. The illumination demands to comply standard ISO 8995:2002(E) require surface illumination levels between 100 lx and 1000 lx. In areas where continuous work is carried out the maintained illuminance should be higher than 200 lux. The illuminance uniformity should not be less than 0.7 for the task illuminance and should not be less than 0.5 for immediate surrounding areas where the uniformity can be expressed as the ratio of the minimum to average value [1].

Flicker is defined as fluctuation of the brightness of light. Any potential flicker that results from light modulation for communication must be mitigated because it may invoke negative or harmful physiological changes in human beings. The maximum flickering time period (MFTP) condition should be met in order to avoid the flicker. MFTP is defined as the

maximum time period of the light intensity change which the human eye is not able to notice. There is no exact MFTP number, however, a frequency greater than 200 Hz is generally considered safe [11].

Dimming support consideration is another important aspect for VLC in terms of power savings and energy efficiency. The illumination dimming function is required while the communication function is still available. The human eye does not perceive changes in light intensity in a linear manner as illustrated in figure 1.4. Thus, the VLC system has to be carefully designed as the human eye is more sensitive to low light intensity levels [25].

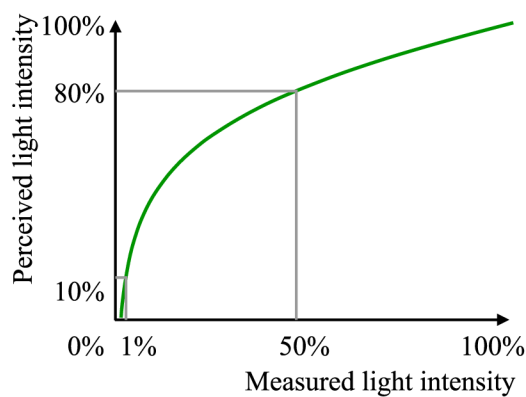


Figure 1.4: Light intensity human perception

1.3 Optical receiver for VLC applications

The receiving task in VLC systems of light conversion into an electric domain is unavoidably performed using the suitable optical detector. Similarly, as in the case of an optical transmitter the receiver plays a crucial role in the optical communication system. According to communication system demands, two major receiver types may be distinguished.

1.3.1 Photodiode communications

In photodiode (PD) communications, a key receiver element forms a PD. The PD based receiver or point receiver is well suited for high speed VLCs. A high responsivity, uniformity over the desired wavelengths, sufficient bandwidth and adding almost no noise into the communication system are crucial assumptions of high speed VLCs. In other words, the PD properties strictly depend on the material and manufacture technology. Basically, there exists the following types of photo-diodes: PIN PD, avalanche PD (APD) and PDs based on organic compounds.

PIN photodiode is perhaps the most common photodetector made of a p-n semiconductor junction. The PIN PD has a lightly n-doped intrinsic layer sandwiched between the p- and n-type regions. Applying an electric field across the intrinsic layer results in constant acceleration for the charge carriers which substantially increases the bandwidth up to several GHz. Therefore, the PIN PD is a suitable choice for high data rate applications.

Avalanche photodiode means a further step in terms of PD sensitivity. Basically, APD is a variation of the PIN PD. High bias voltage applied across the pn junction causes avalanche multiplication of the photo current. Thus, signal amplification happens inside the PD resulting in higher sensitivity compared to the PIN photodiode [54, 33].

Organic photodiode based on bulk hetero-junction is recently a fairly discussed type of a new photodetector. Similarly, as OLEDs the organic photodetector (OPD) seems to be a promising technology for the next generation. OPD is fabricated using organic compounds instead of conventional semiconductors. The uniqueness of OPD technology lies in superior responsivity compared to silicon PDs, low cost and customization (ink jet printing). On the other hand, state-of-the-art OPD suffers from lack of bandwidth, more specifically, the bandwidth is not greater than several hundreds of kHz [55].

1.3.2 Image sensor communications

Image sensor communications (ISC) is a new type of wireless optical communication which employs a camera sensor as an optical signal receiving element. Modern complementary metal-oxide-semiconductor (CMOS) image sensor technology is now affordable and capable

of capturing video at very high frame rates. Almost all modern vehicles already have an built-in camera sensor to detect oncoming vehicles or to control headlight illumination. Thus, ISC has a great potential in future automotive and road safety. Moreover, every smart device is equipped with at least one camera which makes ISC a hot candidate also for wireless personal communications or for indoor localization. On the other hand, the communication rate is limited by the sensor frame rate [18]. Therefore, new cutting-edge technology based on the optical communication image (OCI) sensor combines image pixels with communication pixels on a single chip in order to increase the ISC communication performance [30].

1.4 VLC modulation techniques

Similarly, as in conventional RF communication, in VLC exists certain demands and requirements for suitable modulation techniques. Modulation techniques widely used in OWC systems employing IM/DD are appropriate for VLC applications. However, transmitters in VLC are firstly illumination devices and then communication devices. Thus, illumination requirements have a bigger priority. In other words, the most relevant requirement arises from the need of combining lighting intensity control together with an appropriate modulation technique. Other demands are connected with mitigation of the emitter flickering effect caused by optical power fluctuation on the transmitter side. To ensure that the flickering effect is eliminated, the condition of MFTP must be fulfilled. Considering previously mentioned demands, several modulation schemes were tailored for VLC applications. Figure 1.5 depicts an overview of available modulations for VLC applications [36].

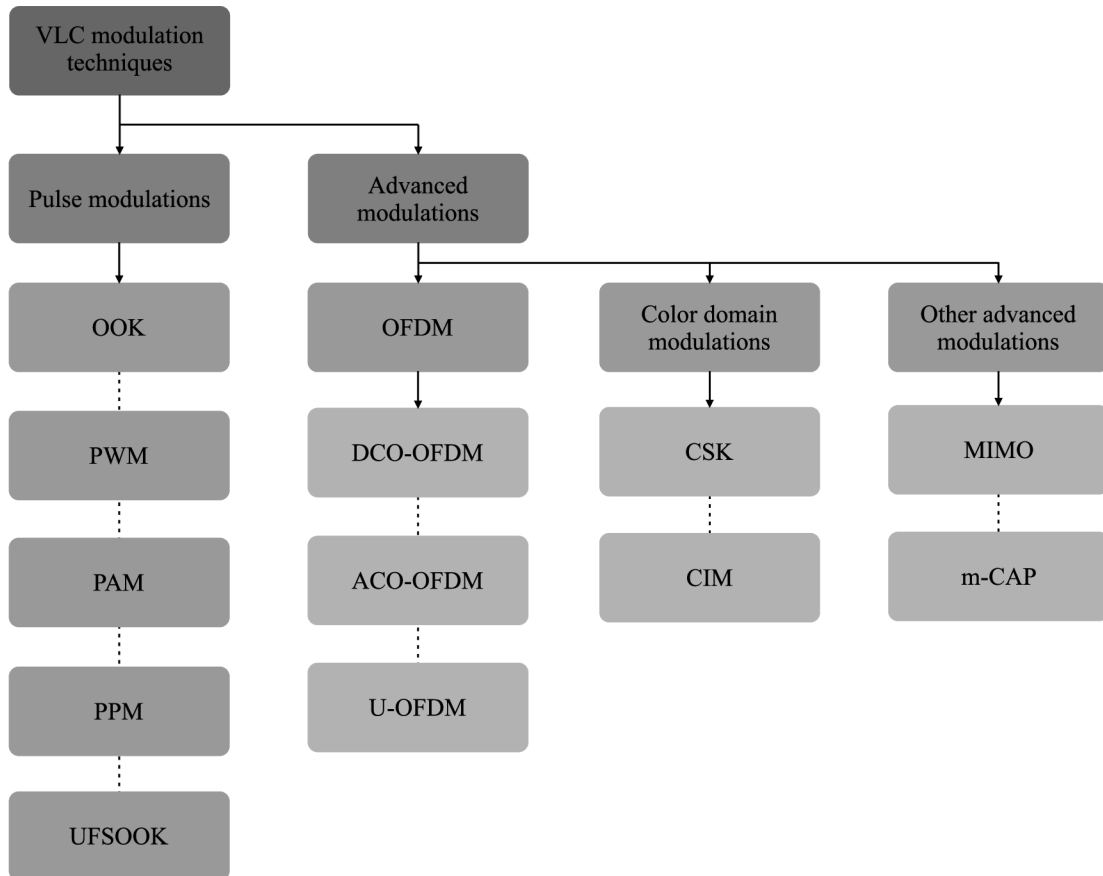


Figure 1.5: VLC modulations

1.4.1 Pulse modulation techniques

Single carrier modulation techniques are the simplest and easiest to implement for VLC. Modulation techniques such as on-off keying (OOK) illustrated in figure 1.6a, pulse width modulation (PWM), pulse amplitude modulation (PAM) or pulse position modulation (PPM) are ideal for moderate data rates. Basically, in pulse based modulation the incoming bits 0 and 1 switch LED between on and off states which results in light intensity modulation. In order to balance the DC component and to implement the system clock, Manchester coding may be used. Dimming control can be carried out by changing voltage/current level of the individual on and off symbols. Alternatively, dimming control may be implemented by changing the signal duty cycle along with the application of time compensation blocks. However, the latter approach is not convenient for VLC applications. For that reason some more effective pulse based modulation techniques were proposed. The first modulation technique tailored purely for VLC applications is variable pulse position modulation (VPPM) shown in figure 1.6b. High and low bits are distinguished by their position as illustrated in figure 1.6b. Dimming control is handled by a symbol duty cycle. Also, other modulation options derived from pulse modulations were proposed. On the other hand, phosphorus-coated LEDs suffer from lack of modulation bandwidth which requires suitable equalization methods to be employed. Maximum likelihood sequence detection (MLSD), frequency domain equalizers (FDE), nonlinear decision feed-back equalizers (DFE), and linear feed forward equalizers (FFE) are appropriate means for the equalization process which differs in the degree of performance and computational complexity [50, 17]. In order to increase the data rate, the RGB LED may also be used in wavelength division multiplex (WDM). Alternatively, more sophisticated multi carrier modulation techniques should be adopted to reach higher data rates [6, 40].

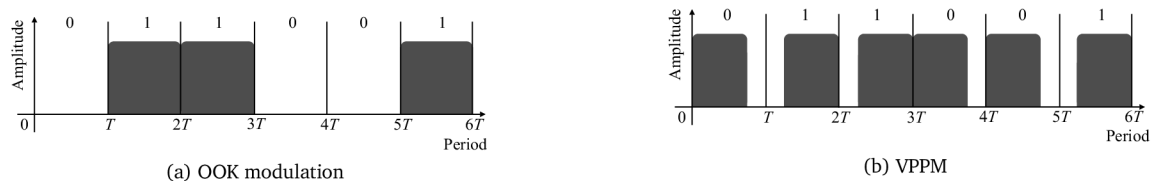


Figure 1.6: Basic VLC modulation techniques

1.4.2 Advanced modulation techniques

Multi carrier modulation schemes have been used in RF systems for many years. Perhaps, among the best known modulation schemes undoubtedly belongs discrete multi tone modulation (DMT) together with orthogonal frequency division multiplexing (OFDM). OFDM is, as a phenomenal modulation technique, superior in terms of modulation efficiency. Generally, multi carrier modulation techniques as OFDM can convert frequency selective fading

of the communication channel into flat fading by employing a simple equalizer. Moreover, OFDM supports adaptive bit and power loading able to adapt the channel utilization in terms of channel frequency response. On the other hand, it is not possible to use OFDM for optical communication without necessary modifications. A conventional OFDM signal is generally complex and bipolar. An optical OFDM signal must be represented as intensity, i.e. the signal must be unipolar and real valued. Practically, a real OFDM signal can be generated by constraining the inverse fast Fourier transform (IFFT) input to have Hermitian symmetry. Several optical OFDM modulation schemes were derived from a traditional OFDM to meet VLC requirements. DC biased optical OFDM (DCO-OFDM) is widely used in VLC. DC bias is added to the signal to achieve a unipolar OFDM output as depicted in figure 1.7a. However, the large peak-to-average power ratio (PAPR) of the OFDM signal limits the overall communication system performance.

A real unipolar OFDM signal can be obtained by utilizing Fourier transformation properties. Asymmetrically clipped optical OFDM (ACO-OFDM) (shown in figure 1.7b) is another proposed variant of an optical intensity OFDM modulation technique. The principle of ACO-OFDM is to skip the even subcarriers by only loading the odd subcarriers with useful information. The bipolar signal is clipped at the zero level as depicted in figure 1.7b. Provided the odd subcarriers are non zero at the IFFT input, the clipping noise affects the even subcarriers. Consequently, only odd carriers are available to carry the data [9].

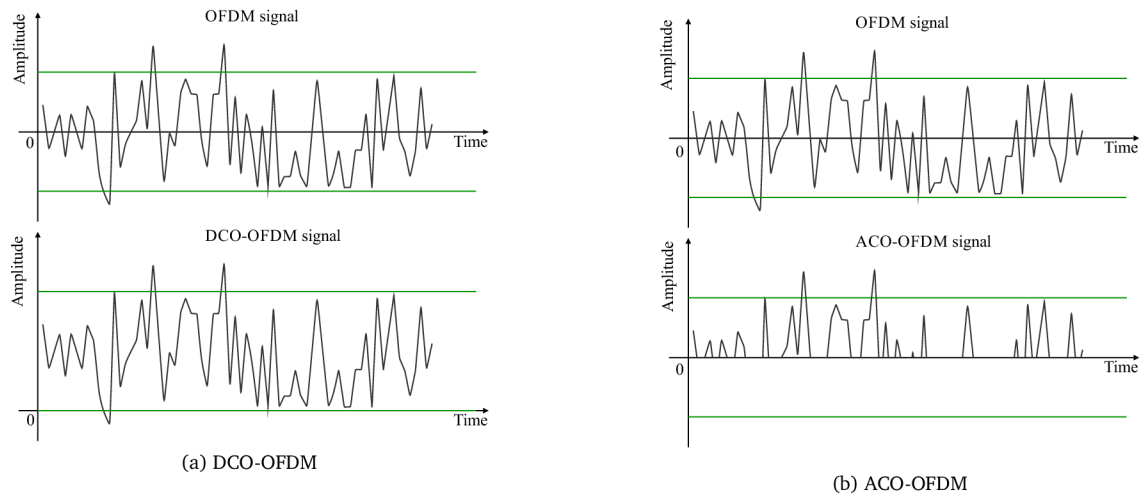


Figure 1.7: Utilized optical OFDM modulations

Unipolar OFDM (U-OFDM) and Flip-OFDM are principally identical. Hermitian symmetry is applied on the M-QAM input symbols. The bipolar OFDM signal obtained afterwards is expanded into two time-domain frames in U-OFDM with similar sizes to the original OFDM frame. The first frame is the same as the original frame where the second frame is a flipped replica of the original one. A unipolar OFDM waveform may be achieved by zero-level clipping without the need of any DC biasing. On the receiver side, each second frame is sub-

tracted from the first frame of the same pair in order to reconstruct the original bipolar OFDM frame. The spectral efficiency of U-OFDM is half of the spectral efficiency of DCO-OFDM as two U-OFDM frames are required to convey the same information conveyed. OFDM was modified in many studies to comply Li-Fi specifications [51].

A novel modulation approach with future potential employs a multi-band carrier-less amplitude and phase (m-CAP) modulation. The modulation m-CAP may outperform optical OFDM in terms of system complexity. Unlike OFDM, m-CAP does not use Fourier transform. The carrier frequencies in m-CAP are generated by finite impulse response (FIR) filters. Figure 1.8 depicts ideal frequency responses and bandwidth requirements for different orders of m-CAP [32].

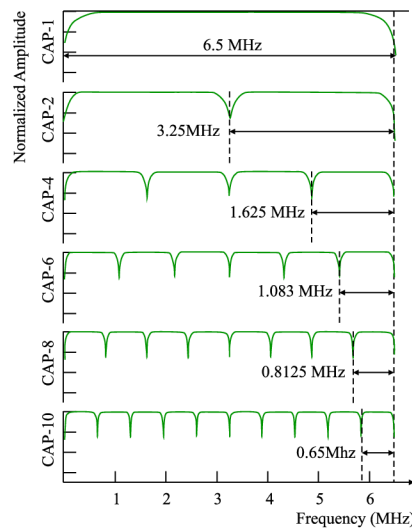


Figure 1.8: Ideal frequency responses and bandwidth requirements for different orders of m-CAP

The IEEE 802.15.7 standard suggests a color shift keying (CSK) modulation suitable for VLC applications [6]. Principally, CSK is similar to frequency shift keying (FSK). The only difference is in symbol representation, specifically, each symbol corresponds to a certain wavelength according to the XY color coordinates from the chromatic CIE 1931 color space. The intensity output color in CSK is constant. However, the relative intensities between the colors are changed. Thus, the instantaneous light of the multicolored LED is unstable. Color intensity modulation (CIM) was proposed to enhance the communication capacity without any illumination property constraints [7].

Among advanced modulation techniques, recently more and more discussed, clearly belongs multiple-in, multiple-out (MIMO) systems. Optical MIMO systems follow the essence of RF MIMO systems either in combination with OFDM or not [13].

1.5 Optical channel modeling

Optical link modeling can be performed using several approaches. To be more specific, it is possible to exploit for instance energy, statistical or a deterministic model. Probably the best-known way of optical link modeling uses a deterministic ray model from the perspective of energy distribution over a channel.

It is possible to divide a general configuration of optical links into the following types based on the geometrical relationship between the emitter and receiver. Figures 1.9 depict basic optical links in terms of directionality between the emitter and receiver. Directed optical links illustrated in figures 1.9a and 1.9d applies high directionality for the purpose of maximizing power efficiency. However, such a system requires precise aiming of both communication devices (emitter and receiver). Figures 1.9c and 1.9f exemplify the non-directed approach. This set-up exploits wide angles of both emitter and receiver in order to cover the desired area. A combination of the former optical links, called hybrid links, uses different variations of directed and non-directed optical links. Naturally, this approach benefits from the combination of both set-ups. Another criteria for optical links can be determined from the perspective of obstacles between the emitter and receiver. In the line of sight (LoS) case, the receiver is able to directly see the emitter whereas in the non-LoS case the optical link relies solely on reflections. The non-LoS scenario is illustrated in figures 1.9d, 1.9e and 1.9f. With regard to optical links outdoor applications rely on a particular LoS set-up. A different situation applies to indoor links, where reflections play a key role in the signal path.

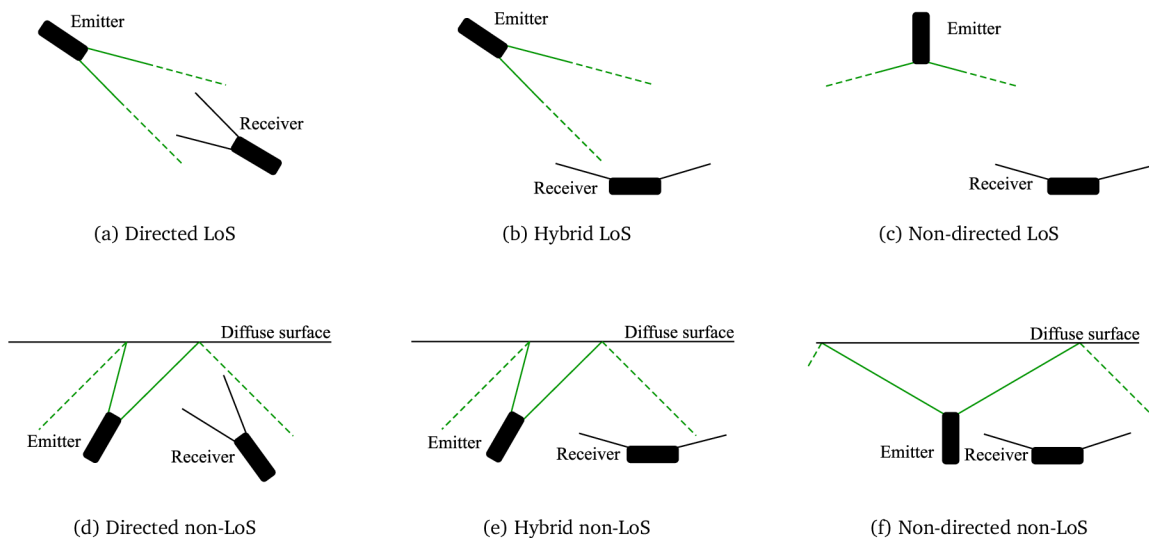


Figure 1.9: Basic optical link configurations according to the degree of directionality of the emitter and receiver. Both emitter and the receiver characteristics are outlined.

A natural property of wireless communication is multipath signal propagation. Thus, VLC also complies with multipath propagation which is crucial especially in enclosed areas when compared to the outdoor environment. Provided low data rates are used (for instance, service data transfers) the signal from a reflected path may improve the quality of the received signal. Conversely, while using high data rates the reflected signal paths induce destructive interference due to the channel impulse response resulting in signal fading.

A significant factor directly affecting the VLC system robustness is the nature of the surrounding environment. Particularly, the most vulnerable is the outdoor scenario. The system receiver is oftentimes exposed to direct sunlight and that results in receiver saturation and inability of correct signal recovery. The presence of dust, vapors and precipitation in the atmosphere might also be critical for open space VLC in terms of signal attenuation. Other pertinent effects affecting signal quality is undoubtedly light pollution. Ambient light, street lamps, and billboards may interfere with the communication system. Therefore, the VLC system must be designed with respect to specific applications in order to suppress unfavorable ambient interference.

System modeling comprises the transmitter model, the channel model and the receiver model. These models directly affect signal propagation and signal recovery. On the transmitter side, the parameters to consider are orientation of LEDs, radiation characteristic and their half power angles (*HPA*) - off-axis angle where the optical power drops by half. The receiver will have the following parameters: modeling the orientation of the photodetector, its field of view (*FOV*), and its responsivity. The general optical channel consists of the direct path between the transmitter and receiver and the multipath due to reflections. The following lines review the possible approaches for IM/DD optical channel modeling which can be conveniently employed for VLC channel modeling.

1.5.1 Barry's method

As a crucial approach in optical channel modeling can be definitely deemed the recursive method introduced by J. Barry [10]. Generally, an optical channel could be completely characterized by its channel impulse response (CIR). In others words, the channel is described by the contribution from the direct path and contributions from the reflected paths modeling channel dispersion as it is stated in equation (1.1). In practice, the proposed Barry's model assumes an empty room split into small tiles representing pure Lambertian reflectors. The sum of contributions from the direct path and reflected paths then generate the overall CIR $h(t)$.

$$h(t) = \sum_{r=1}^{\infty} h^{(r)}(t), \quad (1.1)$$

where $h^{(0)}(t)$ (further written as $h^{\text{LoS}}(t)$) denotes LoS contribution from the direct path,

$h^{(r)}(t)$ means the response of $r - th$ reflection and t states for discrete time.

The method theoretically enables to evaluate an arbitrary order of reflections. Nevertheless, for higher reflection orders Barry's method becomes computationally demanding. Thus, other algorithms improving the original one were proposed.

1.5.2 DUSTIN algorithm

The latter method for calculating multi path dispersion on indoor wireless diffuse channels uses a modified recursive method in order to speed up the simulation processes. This algorithm reduces both the number of operations and memory requirements. More specifically, this method uses time steps rather than the number of reflections [42]. The DUSTIN algorithm can be split into three stages: initialization, wall processing and calculation of the receiver response. The algorithm is intrinsically parallel computing capable and able to compute any number of reflections.

1.5.3 Iterative site-based modeling

This simulation approach improves the recursive method from the perspective of an indoor environment. The method presents a completely deterministic solution allowing fast, accurate channel characterization of complex environments. Dividing the whole environment into separate "boxes" the iterative site-based approach is able to model an interior comprising furniture, people, etc. Additionally, this method is much less time-consuming compared to the classical recursive method able to compute an arbitrary number of reflections [16].

1.5.4 Monte Carlo ray tracing

This method employs a statistical Monte Carlo algorithm for the purpose of CIR modeling. Many rays on the emitter side are generated with a probability distribution equal to its radiation pattern. After each bounce the rays are re-emitted with the probability distribution of the surface. Finally, all the rays are collected on the receiver side [43]. The Monte Carlo ray tracing approach is commonly used in higher level programs, for instance in Zemax. In such a case, CIR is possible to be extracted based on a 3D complex model [56].

1.5.5 Ceiling bounce model

A ceiling bounce model was proposed as an ideal candidate able to easily and accurately model non-directed IR channels. A closed-form expression for CIR relies on the transmitter and the receiver to be collocated in planes parallel to the floor and directed towards the ceiling. The CIR of the ceiling bounce is then obtained by knowing just two parameters, specifically, RMS delay spread D_{RMS} and optical path loss [15].

1.5.6 Curve fitting

The iterative modeling approach is not practical when a fast channel study is required. Then, CIR obtained by fitting the curve on previously measured statistical data may be more convenient. The authors suggest that LoS channel gain follows a modified gamma distribution with parameters depending on the transmitter and receiver spatial relation. Similarly, the channel gain for LoS channels including all reflections follows the modified Rayleigh distribution. In this case, the impulse response characterization requires only knowledge of the distance separating the transmitter, receiver and room parameters [14].

Alternatively, a statistical model of the optical indoor channel may be estimated based on CIR parameters, more specifically, on RMS delay spread D_{RMS} and mean excess delay μ distribution parameters which are involved in the CIR curve fitting [49].

1.6 VLC performance metrics

Transmission inaccuracy is a natural consequence of every wireless communication system. Overall system performance impacts the transmitter, receiver and channel impairments. Especially, optical channel imperfections have a key influence on transmission performance with respect to signal distortion. In order to evaluate VLC system performance, several performance metrics commonly used in RF wireless communication are proposed.

1.6.1 Channel cut-off frequency

Channel impulse response in discrete time can be expressed by $h(t)$. A channel frequency response H_f can be obtained using discrete-time Fourier transform (DFT) of $h(t)$ as follows:

$$H_f = \sum_{n=-\infty}^{\infty} h(t)e^{-j2\pi n f}. \quad (1.2)$$

The channel cut of frequency $H_{f-3\text{dB}}$ in sense of -3dB drop can be then expressed by [41]:

$$|H_{f-3\text{dB}}|^2 = 0.5 |H_f|^2. \quad (1.3)$$

1.6.2 Channel delay spread

The channel RMS delay spread is a commonly used metric of the time dispersion in wireless channels. The delay spread of the channel is considered as an accurate predictor of SNR penalties caused by intersymbol interference (ISI) due to the channel multipath signal propagation [39]. The channel RMS delay spread D_{RMS} can be computed from CIR by using equation (1.4).

$$D_{\text{RMS}} = \sqrt{\frac{\left(\int_{-\infty}^{\infty} (t - \mu)^2 h^2(t) dt\right)}{\int_{-\infty}^{\infty} (h^2(t) dt)}}, \quad (1.4)$$

where the mean excess delay μ is given by [39]:

$$\mu = \frac{\int_{-\infty}^{\infty} t h^2(t) dt}{\int_{-\infty}^{\infty} h^2(t) dt}. \quad (1.5)$$

CIR and D_{RMS} are considered to be deterministic quantities. In other words, the positions of the transmitter, receiver and intervening reflectors are fixed. This fact is in contrast to the time-varying RF channels where D_{RMS} is rather a statistical variable.

1.6.3 Error vector magnitude

The error vector magnitude (*EVM*) as a statistic variable is specified in digital communication as a modulation quality metric. *EVM* measures the difference between a measured signal and a reference signal as expressed in equation (1.6).

$$EVM = \sqrt{\frac{\sum_{t=1}^M \|Z(t) - R(t)\|^2}{\sum_{t=1}^M \|R(t)\|^2}}, \quad (1.6)$$

where R is a reference signal (an ideal base band signal) sampled at the chip rate, Z is a measured signal sampled at the chip rate with time offset and frequency offset being removed, M is the data length and t means the t -th signal sample.

If the difference is noise, then *EVM* is estimated as the square root of the noise-to-signal ratio (*SNR*). *EVM* is a statistic because of the randomness of the noise. If there is no noise, $EVM=0$. Assuming that noise has a Gaussian distribution, the *EVM* variance σ_{EVM}^2 can be calculated as follows:

$$\sigma_{EVM}^2 = \frac{\sigma_n^2}{\sigma_s^2} (2 - \pi/2)/M, \quad (1.7)$$

where σ_n^2 and σ_s^2 denote the signal power and the signal noise, respectively.

As can be extracted from equation (1.7) the *EVM* variance σ_{EVM}^2 depends on *SNR* and the length of the data. Thus, *SNR* can be expected as *EVM* which means that the *EVM* accuracy is related to the *EVM* value itself [61].

1.6.4 Root mean square error

Occasionally, the *EVM* error performance metric is not a straightforward evaluation method in terms of channel impairments and distortion effects. In such cases, the relative root mean square error E_{RMS} may be a fair performance metric able to evaluate the signal affected by the communication channel. The normalized versions $v(t)$ and $\bar{v}(t)$ of the original (transmitter side) and reconstructed (receiver side) signals, respectively are compared. Also, assuming that the receiver starts processing as soon as the first signals reach the photodetector, it is necessary to consider the delayed replica of the original signal in order to have a fair error evaluation. In this respect, a delayed replica of the original signal $v(t)$ was use for this purpose. The term Δt is the minimum time delay measured for each receiver position, that is, corresponding to the smallest direct path between transmitters and receiver. The relative root mean square error E_{RMS} is calculated as follows:

$$E_{\text{RMS}} = \frac{\sqrt{\frac{1}{T} \int_{\Delta t}^{T+\Delta t} (v(t - \Delta t) - \bar{v}(t))^2 dt}}{\sqrt{\frac{1}{T} \int_{\Delta t}^{T+\Delta t} (v(t - \Delta t))^2 dt}}. \quad (1.8)$$

1.6.5 Signal to noise ratio

SNR belongs among the most meaningful metrics in telecommunications. *SNR* is defined as the ratio of desired signal power level P_{Sig} and noise performance P_{n} as expressed in equation (1.9).

$$SNR = \frac{P_{\text{Sig}}}{P_{\text{n}}}. \quad (1.9)$$

1.6.6 Bit error ratio

Bit error ratio (*BER*) is used as the fundamental performance metric in digital communications. Basically, *BER* represents the probability estimation if a bit is received incorrectly due to noise. Mathematically, *BER* can be written as a ratio of bits received with error n_{Err} and the total number of received bits n_{Total} as expressed in equation (1.10).

$$BER = \frac{n_{\text{Err}}}{n_{\text{Total}}}. \quad (1.10)$$

2 OBJECTIVES OF THE THESIS

VLC is a highly perspective area of modern wireless communication. Unlike the conventional transmitter front-end, the ODAC concept is able to cope with LED driving constraints with no need of electrical DAC in the transmitter stage. Therefore, ODAC is an ideal candidate to participate with advanced modulation schemes, for instance OFDM-based modulation tailored for VLC.

The dissertation thesis is focused on analyzing and designing a VLC system using ODAC array as the transmitter front-end. Although the ODAC concept has already been proposed, there exists no study which deeply explores VLC channel modeling. Furthermore, there exists no research dealing with real time VLC systems employing the ODAC concept as the transmitter front-end. The most relevant dissertation objectives can be summarized as follows:

Dissertation objectives

1. Based on previous findings, the first aim is to create a suitable simulation model for studying multipath optical signal propagation of VLC systems employing the ODAC concept. In further steps, the VLC simulation model will be used to determine a suitable ODAC architecture with respect to transmitter dimensions and transmitter bit resolution.
2. The following objective is to design an ODAC-based VLC system using the previously developed simulation model. In this second objective the overall system performance will be revealed.
3. The third aim is to design an ODAC emitter hardware implementation and evaluate the overall performance of the ODAC sample. The key ODAC emitter parameters as well as a practical demonstration of a real time communication ODAC-based system will be explored.

3 VLC SYSTEM MODELING

This chapter describes in detail the VLC system model able to study the ODAC communication system performance in terms of transmitter architecture, multi-path optical signal propagation and geometrical relations between the transmitter, optical channel and the receiver. The proposed numerical model is based on the modified Barry's method implemented in the MATLAB environment. A suitable ODAC emitter architecture is chosen based on preliminary simulation results. Furthermore, several optical channel scenarios are demonstrated in order to explore the ODAC communication system performance.

3.1 VLC system models

The proposed VLC system model may be split into three fundamental parts, more specifically, into the emitter model, the reflection model and the receiver model. In the following lines, the mathematical definition of the individual models is described.

3.1.1 Emitter model

In VLC the transmitter is formed by a source of radiation which operates in the visible area of the electromagnetic spectrum. As a general rule, in VLC domain the system transmitter always employs LEDs or an array of LEDs as a visible light source. Due to the relatively short switching time the LEDs are ideal for further modulation and high speed data transfers. System transmitting active areas for LoS links as well as for non-LoS links could be ideally modeled with a generalized Lambertian model. More specifically, optical transmitting intensity distribution is a cosine function of angle.

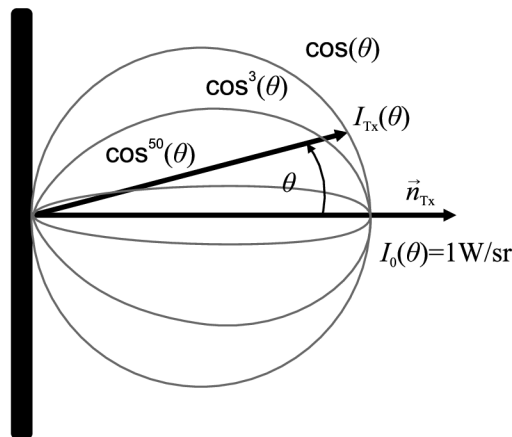


Figure 3.1: Normalized shape of the generalized Lambertian radiation pattern

Figure 3.1 illustrates a typical generalized model of such an emitter area with rotating symmetry. Practical approximation of $I_{\text{Tx}}(\theta)$ can be expressed by the following formula (3.1):

$$I_{\text{Tx}}(\theta) = I_0 \cos^n(\theta), \quad (3.1)$$

where θ is the viewing angle of transmitter, I_0 is radiant intensity normal to the LED source, n characterizes the directivity index of the LED, defined by the HPA $\theta_{1/2}$ ($n = 1$ corresponds to a traditional Lambertian source). From the definition $I_{\text{Tx}}(\theta_{1/2})/I_0$ at the half angle is 0.5. Mathematically, n can be then derived from (3.2):

$$\cos^n(\theta_{1/2}) = 0.5, \quad (3.2)$$

which yields (3.3):

$$n = \frac{\ln(0.5)}{\ln(\cos(\theta_{1/2}))}. \quad (3.3)$$

Assuming that the LED intensity pattern can be approximated by the generalized Lambertian model, the equation which describes optical power P_{Tx} emitted by an LED into the hemisphere can be written as (3.4):

$$I_{\text{Tx}}(\theta) = \frac{n+1}{2\pi} P_{\text{Tx}} \cos^n(\theta) \quad \text{for } \theta \in [-\pi/2, \pi/2]. \quad (3.4)$$

The coefficient $(n+1)/2\pi$ ensures that integrating $I_{\text{Tx}}(\theta)$ over the solid angle of the hemisphere results in the source power P_{Tx} . In order to simplify the notation, the general transmitter function H_{Tx} derived from (3.4) is further denoted as follow (3.5):

$$H_{\text{Tx}}(n, \theta) = \frac{n+1}{2\pi} \cos^n(\theta) \quad \text{for } \theta \in [-\pi/2, \pi/2]; \vec{n}_{\text{Tx}}, \quad (3.5)$$

where \vec{n}_{Tx} is emitter normal vector [20, 10, 39].

3.1.2 Reflection model

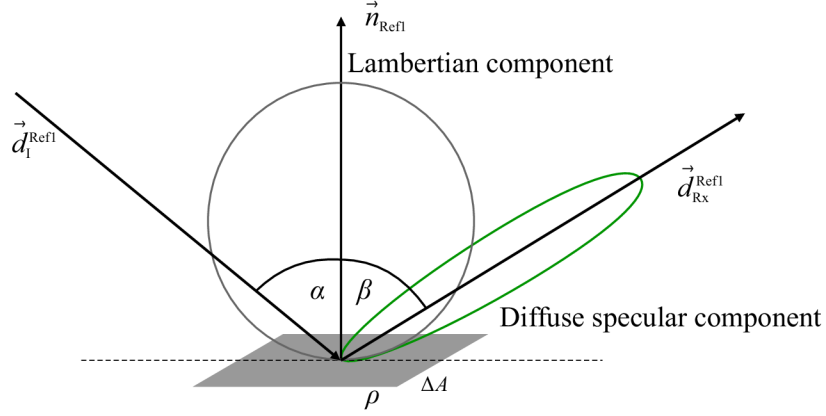


Figure 3.2: Reflection model

Reflection and/or diffusion occurs when the transmitted light wave meets a surface whose dimensions are larger when compared to the wavelength. The nature of the reflection depends on several factors, in particular the surface roughness, the angle of incidence and wavelength. Basically, there are two types of reflection related to wavelength of incident radiation which can be considered: i) specular reflection, for perfectly smooth surfaces; and ii) diffuse specular reflection, for surfaces with some degree of roughness. The nature of diffuse specular reflections depends on the angle of incidence wave and have elaborate models. On the other hand, ideally, diffuse reflectors can be modeled as pure Lambertian sources. Figure 3.2 illustrates a general reflection model with radiation symmetry with respect to first order reflection normal vector \vec{n}_{Ref1} . Diffuse reflectors can be approximated using Lambert's model which yields the following reflection function R_{Lambert} (3.6):

$$R_{\text{Lambert}}(\rho, \Delta A, \|\vec{d}_I^{\text{Ref1}}\|, \alpha, \beta) = \frac{\rho \Delta A}{\pi \|\vec{d}_I^{\text{Ref1}}\|^2} \cos(\alpha) \cos(\beta) \quad \text{for } \vec{n}_{\text{Ref}}, \quad (3.6)$$

where R_{Lambert} represents reflection function, ρ is the surface reflection coefficient, \vec{d}_I^{Ref1} and $\|\vec{d}_I^{\text{Ref1}}\|$ represents the incident direction and distance, respectively. Symbol ΔA is the surface element area and α , β are angles of incidence and reflection, respectively.

In general, the character of most real surfaces is a combination of both diffuse and specular contributions. For these cases, Phong model R_{Phong} represents an appropriate choice able to represent a good trade between accuracy and complexity. In Phong's model the diffuse component is modeled by the Lambert model, while the specular component is represented by a function which depends on the angle of incidence α and the observation angle β . The

Phong model is described by the following equation (3.7) [12]:

$$R_{\text{Phong}}\left(\rho, \Delta A, \left\| \vec{d}_I^{\text{Ref1}} \right\|, \alpha, \beta\right) = \frac{\rho \Delta A}{\pi \left\| \vec{d}_I^{\text{Ref1}} \right\|^2} \times \cos(\alpha) [r_d \cos(\beta) + (1 - r_d) \cos^n(\beta - \alpha)] \quad \text{for } \vec{n}_{\text{Ref}}, \quad (3.7)$$

where r_d is the percentage of incident optical signal reflected diffusely.

The following table demonstrates reflection functions of common materials:

Material	Reflection function
Painted wall	$R_{\text{Lambert}}\left(\rho, \Delta A, \left\ \vec{d}_I^{\text{Ref1}} \right\ , \alpha, \beta\right) = \frac{\rho \Delta A}{\pi \left\ \vec{d}_I^{\text{Ref1}} \right\ ^2} \cos(\alpha)$
Floor tiles	$R_{\text{Phong}}\left(\rho, \Delta A, \left\ \vec{d}_I^{\text{Ref1}} \right\ , \alpha, \beta\right) = \frac{\rho \Delta A}{\pi \left\ \vec{d}_I^{\text{Ref1}} \right\ ^2} \cos(\alpha) [0.6 \cos(\beta) + (1 - 0.6) \cos^6(\beta - \alpha)]$
Computer box	$R_{\text{Phong}}\left(\rho, \Delta A, \left\ \vec{d}_I^{\text{Ref1}} \right\ , \alpha, \beta\right) = \frac{\rho \Delta A}{\pi \left\ \vec{d}_I^{\text{Ref1}} \right\ ^2} \cos(\alpha) [0.001 \cos(\beta) + (1 - 0.001) \cos^3(\beta - \alpha)]$
Glass	$R_{\text{Phong}}\left(\rho, \Delta A, \left\ \vec{d}_I^{\text{Ref1}} \right\ , \alpha, \beta\right) = \frac{\rho \Delta A}{\pi \left\ \vec{d}_I^{\text{Ref1}} \right\ ^2} \cos(\alpha) [0.6 \cos(\beta) + (1 - 0.6) \cos^{13}(\beta - \alpha)]$
Monitor screen	$R_{\text{Phong}}\left(\rho, \Delta A, \left\ \vec{d}_I^{\text{Ref1}} \right\ , \alpha, \beta\right) = \frac{\rho \Delta A}{\pi \left\ \vec{d}_I^{\text{Ref1}} \right\ ^2} \cos(\alpha) [0.39 \cos(\beta) + (1 - 0.39) \cos^{10}(\beta - \alpha)]$
White ceramic	$R_{\text{Phong}}\left(\rho, \Delta A, \left\ \vec{d}_I^{\text{Ref1}} \right\ , \alpha, \beta\right) = \frac{\rho \Delta A}{\pi \left\ \vec{d}_I^{\text{Ref1}} \right\ ^2} \cos(\alpha) [0.06 \cos(\beta) + (1 - 0.06) \cos(\beta - \alpha)]$

Table 1: Mathematical relations allowing the calculation of the reflection function for various materials according to the angle of incidence α and the angle of observation β [12].

3.1.3 Receiver model

Figure 3.3 depicts a general model of receiving surface with an axis symmetry with respect to \vec{n}_{Rx} where \vec{n}_{Rx} is the receiver normal vector. The detected signal impinges a photo-detector active area A_{Rx} after traveling a distance expressed by $\left\| \vec{d}_{\text{Rx}} \right\|$ (with $A_{\text{Rx}} \ll \left\| \vec{d}_{\text{Rx}} \right\|^2$) between transmitter and receiver.

In order to simplify the channel model notation, the generalized function of the receiver H_{Rx} can be written as (3.8):

$$H_{\text{Rx}}\left(\left\| \vec{d}_{\text{Rx}} \right\|, \psi\right) = \frac{T(\psi) g(\psi) A_{\text{Rx}}}{\left\| \vec{d}_{\text{Rx}} \right\|^2} \cos(\psi) \text{rect}\left(\frac{\psi}{\text{FOV}}\right) \quad \text{for } \vec{n}_{\text{Rx}}, \quad (3.8)$$

where ψ is the viewing angle of the receiver, $T(\psi)$ is the filter transmission (not shown in figure 3.3), $g(\psi)$ concentrator gain (not shown in figure 3.3), FOV is the receiver field of view and the $\text{rect}(x)$ function is the receiver FOV bounding function, given by (3.9).

$$\text{rect}(x) = \begin{cases} 1 & \in |x| \leq 1 \\ 0 & \in |x| > 1 \end{cases} \quad (3.9)$$

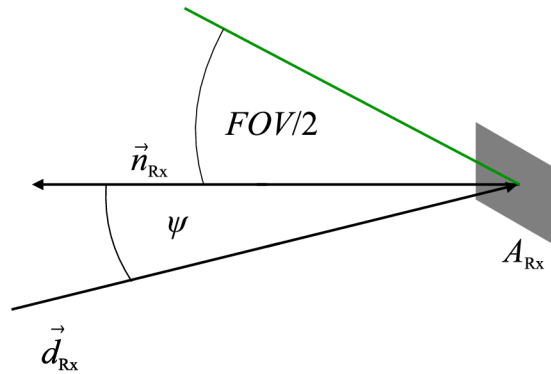


Figure 3.3: Generalized receiver model

3.2 ODAC LED array arrangements

Figure 3.4 shows the five varied LED arrays under consideration. These arrays had different symmetries and bit depths, ranging from 5 to 8 bits. Each array was composed of k LED groups where k represented the bit depth of the LED array. The proposed ODAC LED arrays followed the binary weighted architecture. Inside each group, the number of LEDs depended on the symmetries of the topology. For the 5-bit depth LED array, the array had horizontal and vertical symmetries, thus the number of LEDs was always a multiple of 4 for each bit level. In the present case, with bit depth equal to 5, the total number of LEDs was 124, as illustrated in figure 3.4a. The LED arrays for 7 and 8-bit depths were one axis symmetric. The number of LEDs inside the array was directly given by $2^k - 1$ as shown in figures 3.4b and 3.4c.

Figure 3.4d presents a special 8-bit ODAC emitter type employing PLCC6 LEDs. The key distinction between the previous ODAC emitter models lies in the hardware design itself. Whilst the first sizable LED array models used discrete 5mm LEDs, the last proposed LED array exploited PLCC6 LEDs. Specifically, the PLCC6 LED comprises three LED chips in one package which significantly reduces the array dimensions and may improve optical intensity displacement in the near field radiation area as well. Thus, possible signal distortion induced by the array layout at a small distance in front of the emitter may be eliminated.

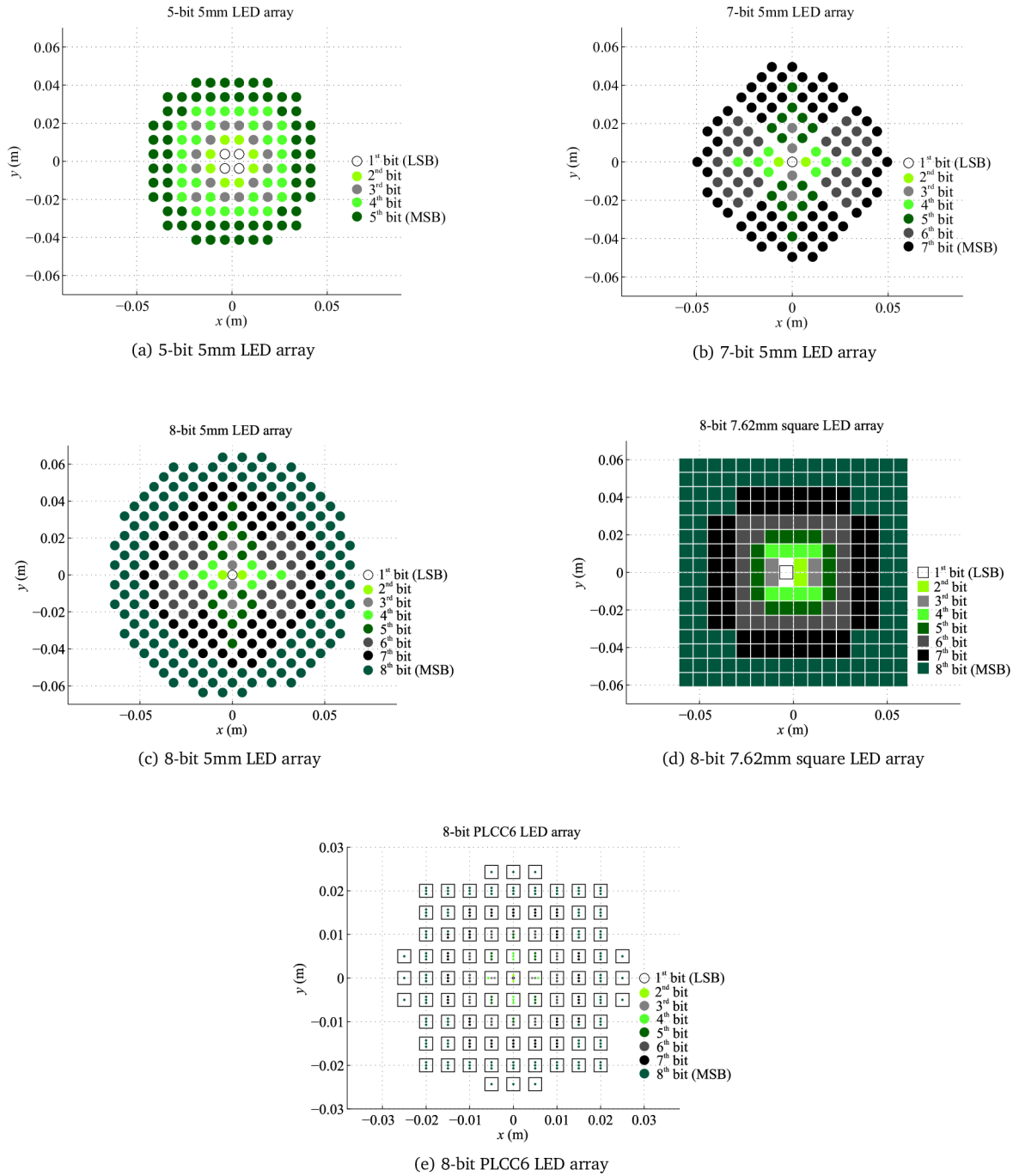
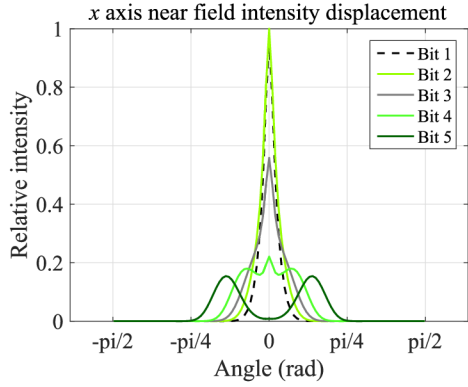


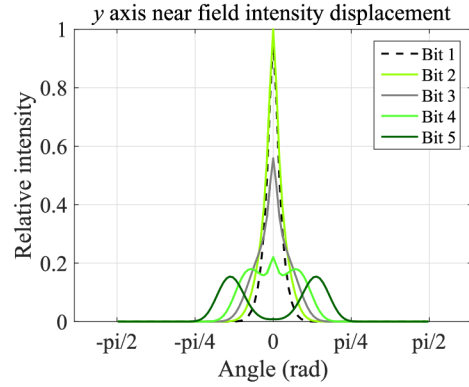
Figure 3.4: ODAC LED arrays

Figure 3.5 shows near field optical intensity displacement of all proposed LED arrays for both x and y axis. The LED array near field boundary, where the optical intensity was captured, was defined as $D = 2s$ where s states for LED array dimension in the given axis. For modeling purposes, 5mm LEDs used standard HPA of 15° , 7.62mm square LEDs had 90° HPA and PLCC6 LEDs were modeled with HPA of 60° . Obviously, LED arrays composed of the LEDs having smaller HPA posed certain optical intensity non-uniformity which might lead to

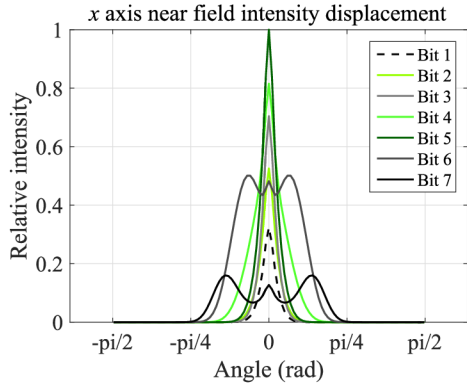
excessive optical signal distortion. On the other hand, LED arrays of higher *HPAs* exhibited finer near field optical intensity displacement.



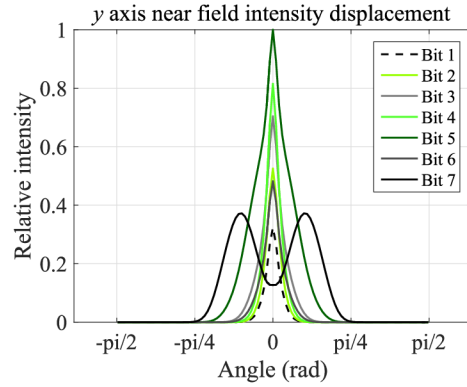
(a) 5-bit 5mm LED array x axis



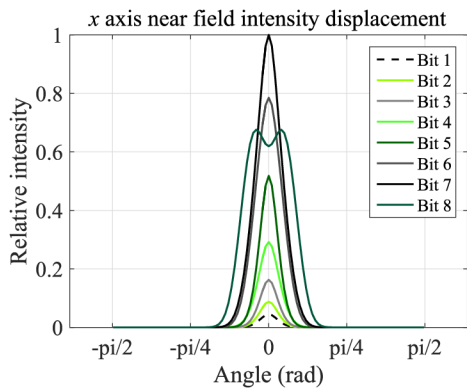
(b) 5-bit 5mm LED array y axis



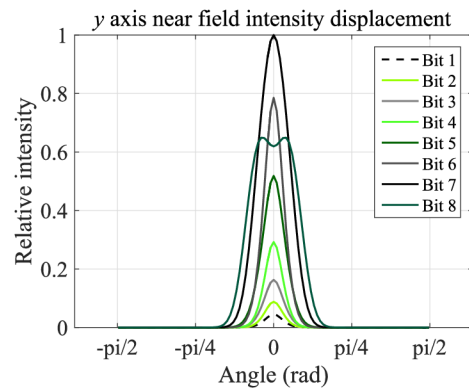
(c) 7-bit 5mm LED array x axis



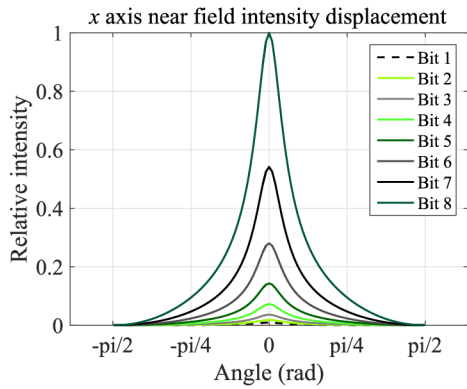
(d) 7-bit 5mm LED array y axis



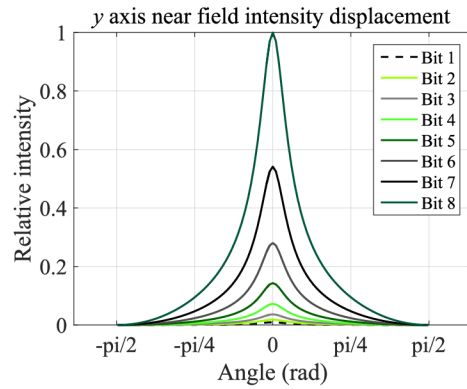
(e) 8-bit 5mm LED array x axis



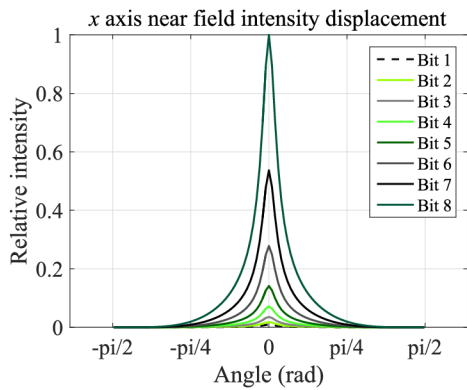
(f) 8-bit 5mm LED array y axis



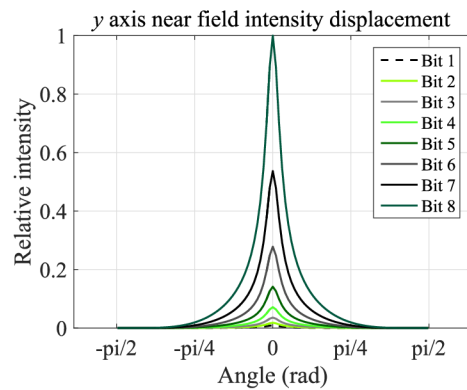
(g) 8-bit 7.62mm square LED array x axis



(h) 8-bit 7.62mm square LED array y axis



(i) 8-bit PLCC6 LED array x axis



(j) 8-bit PLCC6 LED array y axis

Figure 3.5: Near field optical relative intensity displacement

3.3 ODAC-based VLC system performance investigation

Geometrical arrangement, an appropriate LED array topology and bit resolution play key roles in overall performance of the VLC system employing the ODAC-based transmitter. Thus, the following simulation examines error performance of five formerly proposed ODAC LED arrays. It was assumed that the VLC system under consideration operated with one dominant wavelength, i.e. only the blue component participated in the communication (slow yellowish re-emitted component was filtered on the receiver side). A typical spectral characteristic of such white LED is illustrated in figure 3.6 where both essential blue and the yellow peaks can be seen.

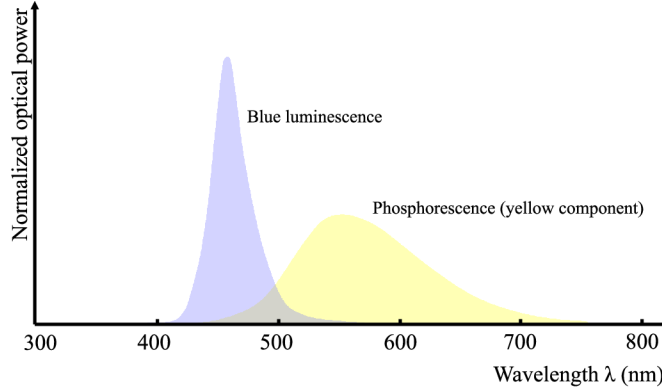


Figure 3.6: Spectral characteristic of the phosphorus-coated LED

Figure 3.7 depicts system conceptual diagram considering only a direct LoS communication path to examine LED arrays in terms of bit depth and array topology. On the transmitter side, an arbitrary waveform generator (AWG) produced a digital signal $v(t)$, represented by a set of k digital bit streams $B(t)$, which were used to modulate k independent groups of LEDs in an LED array. Quantization at the transmitter side was assumed to follow the standard approach: for k LED groups, the signal dynamic range was divided into $2^k - 1$ equal amplitude intervals. Assuming that the digital signals $B(t)$, all had the same amplitude and that the LEDs were driven uniformly for all k groups, the digital weights were set by the number of LEDs in each group, that is, following a binary weight distribution. The transmitted bit streams were then combined on the optical channel and reach the input of the receiver (in this case, represented by a simple transimpedance amplifier (TIA)). The recovered signal $\bar{v}(t)$ was a reconstructed replica of $v(t)$ with approximation error dependent on the bit depth of the array (the number of LED groups, k) and the LED array topology. In a perfect channel, exempt from reflections, delays and constrained FOV , the approximation error would be lower bounded by $LSB/2$, where the least significant bit (LSB) represented the strength of the least significant bit.

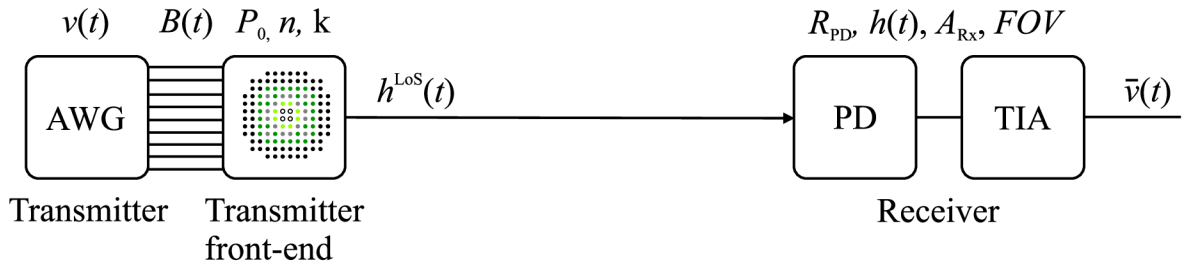


Figure 3.7: Conceptual system diagram

Assuming that the channel impulse response of a single LED is expressed by $h(t)$, the reconstructed signal can be determined by adding the convolutions of the signals $B(t)$ with the LED's individual impulse responses, as stated in (3.10):

$$\bar{v}(t) = R_{\text{PD}} P_0 \sum_{m=1}^k \sum_{n=1}^{2^m-1} B_m(t) \star h_{m,n}(t), \quad (3.10)$$

where P_0 is total optical power, the PD was modeled with active area A_{RX} and responsivity R_{PD} , m denotes order of the LED group in the LED array and n is associated with the number of LEDs for each group m . For slow varying signals, the channel impulse response has negligible impact on signal reconstruction. For these cases, equation (3.10) can be simplified, assuming that the contribution from the LoS path and the multiple reflections add together at an instant of time, and CIR $h(t)$ is a single Dirac impulse, with strength given by the addition of the DC channel gain H in this case only from the direct LoS path, as follow (3.11):

$$\bar{v}(t) = R_{\text{PD}} P_0 \sum_{m=1}^k \sum_{n=1}^{2^m-1} B_m(t) H_{m,n}. \quad (3.11)$$

The DC channel gain for each LED in the array H can be directly computed as LoS contribution H^{LoS} using equations (3.4) and (3.8) according to equation (3.12),

$$H = H^{\text{LoS}} = H_{\text{Tx}}(n, \theta) H_{\text{Rx}}(\|\vec{d}_{\text{Rx}}\|, \psi). \quad (3.12)$$

Equation (3.11) states that for slowly varying signals the approximated signal error depends only on the geometrical features of the set-up, including the *FOV* receiver, the *HPA* LED, the distance between transmitter and receiver, and the presence of reflecting elements. It is necessary to say that the proposed model neglected influence of any noise contributors in order to explore formerly mentioned geometrical dependencies.

As a suitable performance metric able to evaluate signal reconstruction error, the relative root mean square error E_{RMS} was chosen. The normalized versions of transmitted signal $v(t)$ and recovered signal $\bar{v}(t)$ on the receiver side were assumed. ODAC performance assessment used periodic signals to simplify comparison between the original signal and the recovered one. It was assumed that the receiver will start working immediately as the first signals hit the photo-detector. It was necessary to consider the delayed replica of the original signal to have a fair error evaluation. In this case, a delayed replica of the original signal $v(t - \Delta t)$ was used for this purpose. The term Δt is the minimum delay measured for each receiver position, that is, corresponding to the smallest direct path between transmitters and receiver. The term T corresponds to a signal period. The relative root mean square error E_{RMS} is then expressed by equation (3.13).

$$E_{\text{RMS}} = \frac{\sqrt{\frac{1}{T} \int_{\Delta t}^{T+\Delta t} (v(t - \Delta t) - \bar{v}(t))^2 dt}}{\sqrt{\frac{1}{T} \int_{\Delta t}^{T+\Delta t} (v(t - \Delta t))^2 dt}}. \quad (3.13)$$

Figure 3.8 depicts on-axis E_{RMS} dependence on distance x ($y = 0$) between transmitter and receiver. It was assumed that the optical signal travels directly to the receiver having FOV 60° with responsivity $R_{\text{PD}} = 0.8$ V/W. It is apparent that near field optical intensity inhomogeneity resulted in error in front of the transmitter. It can be extracted that the narrow LED HPA resulted in enormous E_{RMS} for near field area. Moreover, insufficient transmitter resolution was a consequence of another excessive error. However, compact PLCC6 LED array dimensions posed certain improvement in front of the transmitter and even over the full length. Figure 3.9 depicts E_{RMS} performance for the receiver being swept over the rectangle area of $6\text{m} \times 2\text{m}$. As can be seen, the results demonstrate E_{RMS} performance in terms of angular displacement and confirms previous error performance behavior for confined LED $HPAs$.

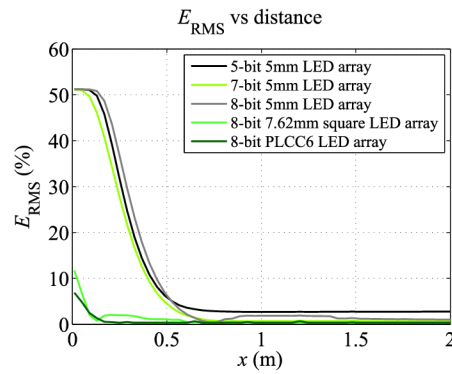
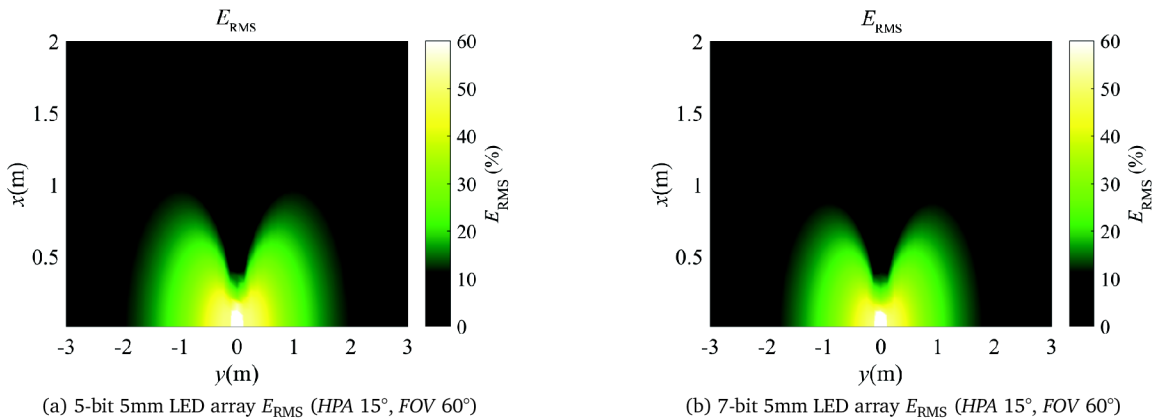


Figure 3.8: On axis E_{RMS} performance



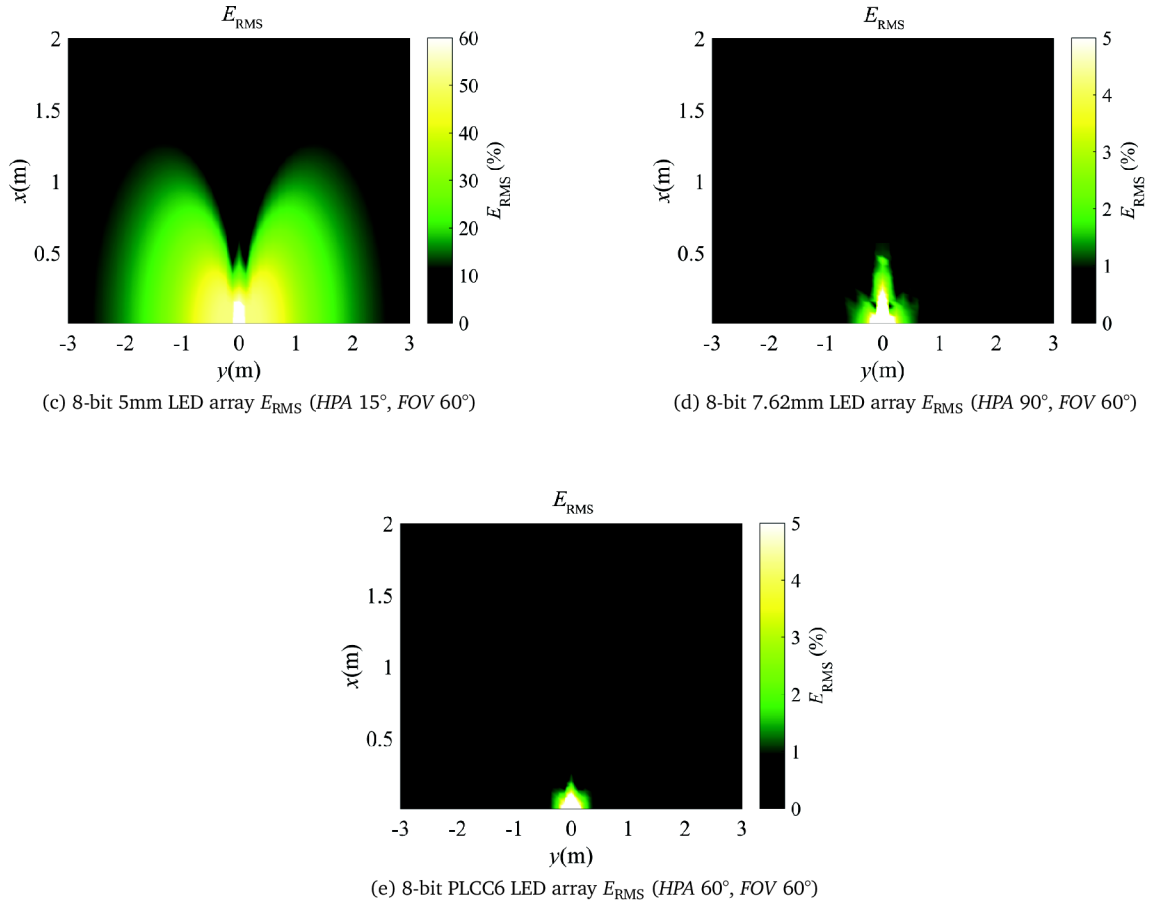


Figure 3.9: Spatial E_{RMS} performance

3.4 Multi-path signal propagation model

Figure 3.10 shows a conceptual VLC system diagram considering both direct LoS communication path and one reflection path. A detailed geometrical set-up under consideration can be seen in figure 3.11.

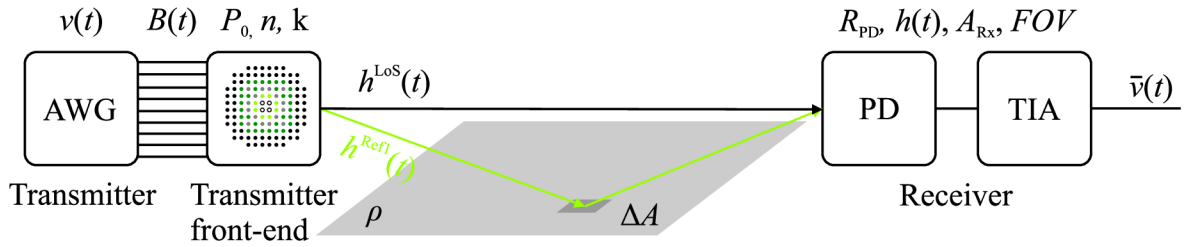


Figure 3.10: Conceptual multi-path system diagram

Figure 3.11 depicts the multi-path system set-up considering one reflection path. The transmitter comprises the LED array, assembled at a height h_{TX} above ground (xy plane), with heading defined by the normalized vector \vec{n}_{TX} . The optical signal traveled through the

optical channel between transmitter and receiver, undergoing path attenuation and reflections from the ground surface. For simulation purposes a single reflection scenario from the ground was assumed. The reflection coefficient was set to $\rho = 0.15$, the single reflection presented a dark ground with a high absorption (worn asphalt was assumed). The receiver was positioned equidistantly at different places in plane xy , with a height h_{Rx} above ground and normalized vector \vec{n}_{Rx} pointing always to the center of the LED array. The DC channel gain for each LED in array H can be separated into two components; the first due to the LoS H^{LoS} contribution and the second one H^{Ref1} due to multiple reflections on the ground surface, given by (3.14).

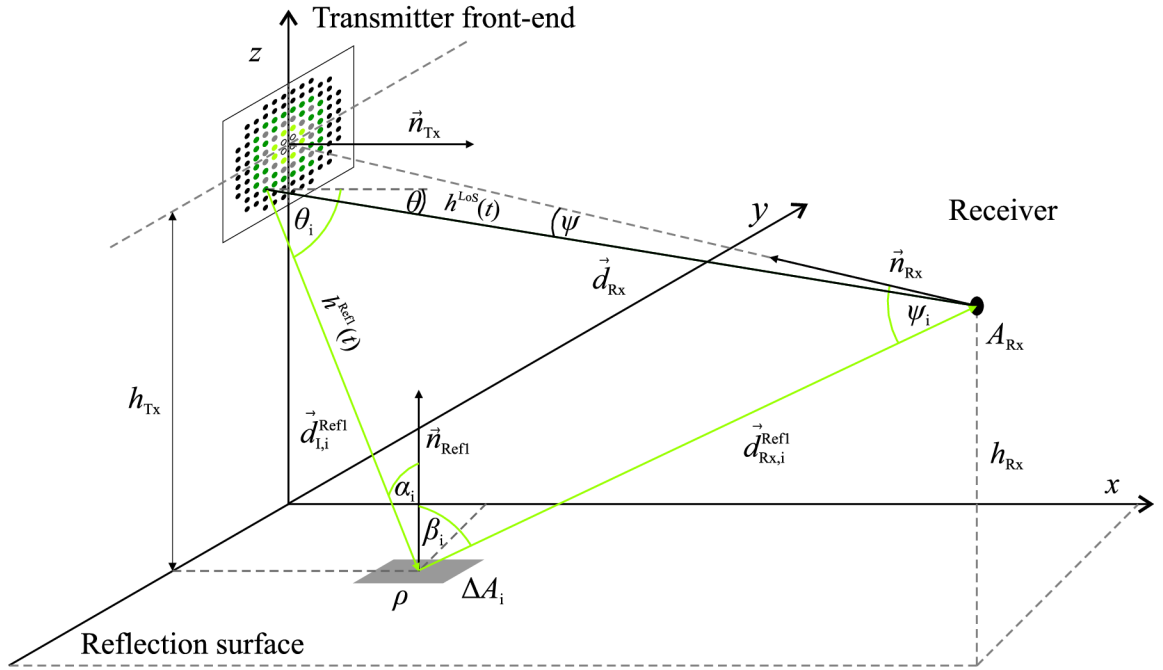


Figure 3.11: Detailed multi-path system set-up

$$H = H^{\text{LoS}} + H^{\text{Ref1}}. \quad (3.14)$$

The gain of the signal arriving to the receiver through the first reflected path H^{Ref1} can be computed using equations (3.4), (3.8) and the appropriate reflection model, in this case Lambertian, given by equations (3.6) or (3.7), which yields (3.15). For the scenario under consideration, worn asphalt was modeled as a pure Lambert radiator.

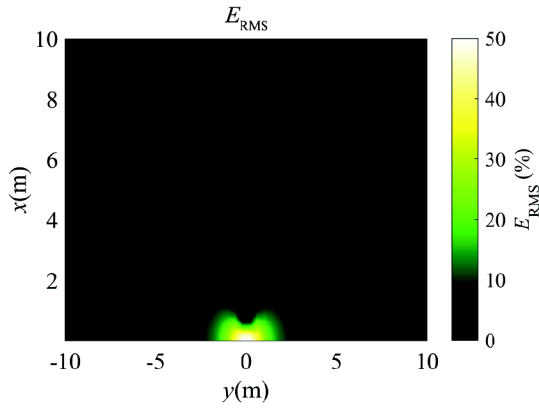
$$H^{\text{Ref1}} = \sum_{i=1}^{G_{\text{Ref1}}} H_{\text{Tx}}(n, \theta_i) H_{\text{Rx}}\left(\left\|d_{\text{Rx},i}^{\text{Ref1}}\right\|, \psi_i\right) R_{\text{Lambert}}\left(\rho, \Delta A_i, \left\|d_{\text{Tx},i}^{\text{Ref1}}\right\|, \alpha_i, \beta_i\right), \quad (3.15)$$

where G_{Ref1} specifies the number of grid elements ΔA used to approximate the reflection contributions from the ground surface, $\left\|d_{\text{Tx},i}^{\text{Ref1}}\right\|$ stands for the distance from the transmitter

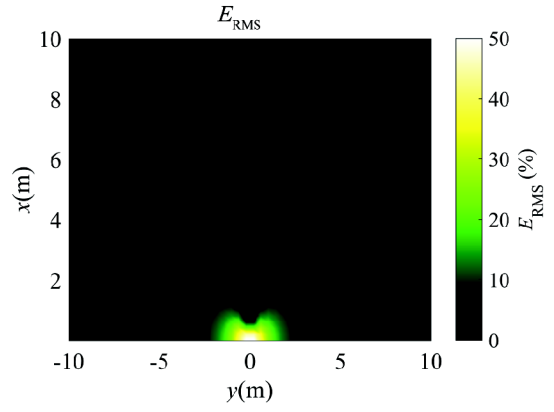
to the first reflection surface, $\left\|d_{\text{Rx}}^{\text{Ref1}}\right\|$ states for the distance from the first reflection surface to the receiver and index i is associated with the number of first reflection paths. Finally, the reconstructed signal can be computed using equation (3.11), thus combining the contribution of every LED in the array, plus the geometrical dependencies of the optical signal propagation.

The relative root mean square error E_{RMS} was selected as the performance metric suitable to the previously used to evaluate the reconstruction error in the VLC system using the ODAC concept. For that purpose the scaled versions $v(t)$ and $\bar{v}(t)$ of the original and reconstructed signals, respectively, were considered. Performance evaluation was based on periodic signals in order to simplify the comparison between the original and reconstructed signal versions.

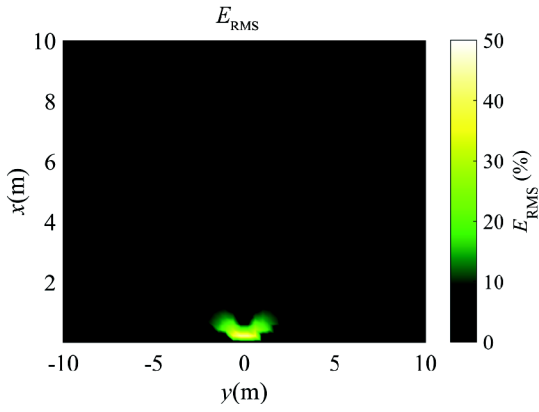
As indicated in equation (3.13) the relative root mean square error E_{RMS} will depend on the positioning of the receiver with respect to the transmitter. The 5mm conventional LEDs under consideration used narrow *HPA* of 15° (suitable for higher communication distances thanks to their high directivity) and total optical power P_0 . The effect of the *FOV* for testing purposes was considered taking 30° and 60° . The figures 3.12, 3.13 and 3.14 show the results for the far field VLC scenario (xy plane 10m x 20m) with the three different LED arrays 5, 7 and 8-bit, respectively. The performance comparison between the LoS scenario and one reflection scenario for 5-bit set-up was made. The simulation proved that an indirect path improves the system performance in front of the transmitter, assuming slow data rates. Furthermore, figures 3.12c and 3.12d show the effect of receiver *FOV*. The achieved results showed that the minimum achieved error was 7.3%, 1.9% and 0.8%, for the 5, 7 and 8-bit depth arrays, respectively. Obviously, the error E_{RMS} decreased with bit depth likewise in the case of electrical DACs (EDACs). As can be expected, the error area in the transmitter near field proportionally increased with the number of LEDs in the array which is a natural consequence of larger emitter dimensions. Nevertheless, the results were also dependent on LED arrangement as shows the simulation for the 7-bit LED array. Specifically, the appropriate LED array arrangement (7-bit LED array model) may exhibit similar error displacement in front of the transmitter when compared to the 5-bit LED array. The error performance in front of the transmitter may also be further improved by increasing the LED placement density inside the LED array. Based on preliminary results, the 8-bit ODAC emitter seems to be the most suitable option for the next study. Thus, the next steps dealing with channel impulse response employ merely 8-bit ODAC front end versions [20].



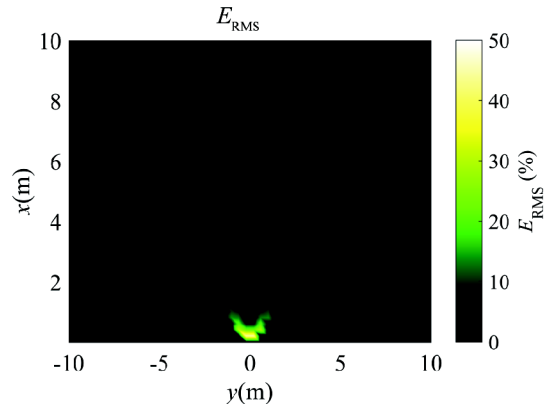
(a) 5-bit 5mm LED array E_{RMS} (LoS, HPA 15°, FOV 30°)



(b) 5-bit 5mm LED array E_{RMS} (LoS, HPA 15°, FOV 60°)

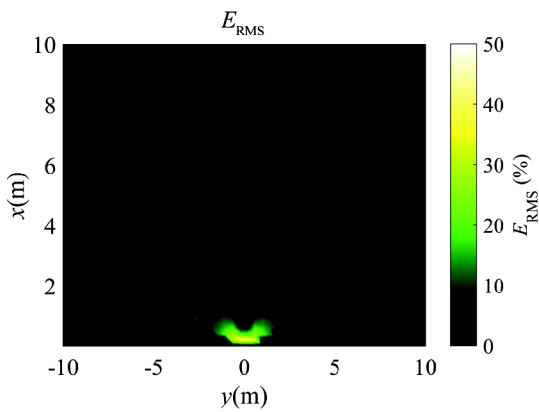


(c) 5-bit 5mm LED array E_{RMS} (LoS+Ref1, HPA 15°, FOV 30°)

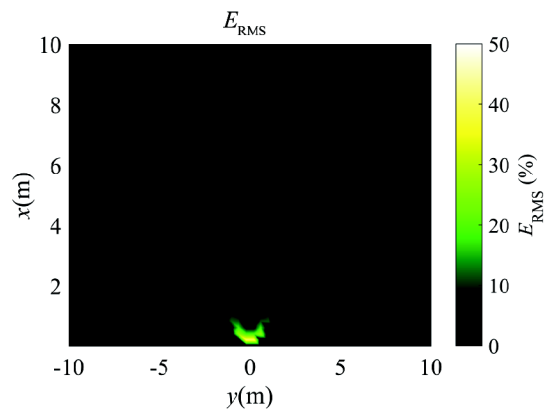


(d) 5-bit 5mm LED array E_{RMS} (LoS+Ref1, HPA 15°, FOV 60°)

Figure 3.12: E_{RMS} performance comparison of 5-bit LED arrays



(a) 7-bit 5mm LED array E_{RMS} (LoS+Ref1, HPA 15°, FOV 30°)



(b) 7-bit 5mm LED array E_{RMS} (LoS+Ref1, HPA 15°, FOV 60°)

Figure 3.13: E_{RMS} performance of 7-bit LED arrays

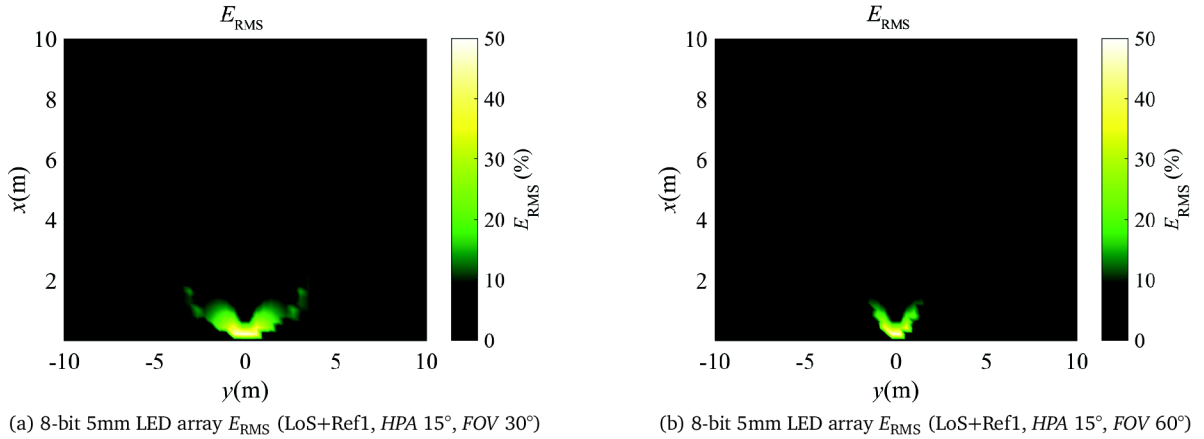


Figure 3.14: E_{RMS} performance of 8-bit LED arrays

3.5 Study on utilizing the ODAC concept in ITS applications

The previous chapter investigated the effects on signal reconstruction error due to geometrical considerations of the set-up assuming low data transmission scenarios. The five variants of the ODAC transmitters were evaluated from the perspective of the front-end bit depth. This chapter extends previous conclusions to the case of high data rate signal transmission, where the channel impulse response (CIR) becomes of paramount importance. This section explores the performance of ODAC front-end adapted into a traffic light head in order to enable transferring information from the infrastructure to a vehicle (I2V) as a part of an intelligent transportation system (ITS). The performance of such a scenario is shown by reconstructing error as a function of emitter placement, LED's half power angle (HPA) and receiver's field of view (FOV). The assumed set-up scenario considered two traffic light heads placed above the ground plane here represented by an asphalt road. The obtained results revealed that ODAC performance strictly depended on geometrical deployment. Moreover, increasing signal frequency additionally introduced noticeable signal distortion.

Figure 3.15 depicts a system model of I2V VLC using ODAC-based LED traffic lights placed into a standardized 300mm signal head case. The emitter consisted of multi-unit signal heads comprising the near right-side head at a height 2.1m and the through head placed at 5.2m above the xz ground plane. The illustrated traffic lights placement complies with standards ČSN 36 5601-1 and ČSN 73 6021 [2, 3].

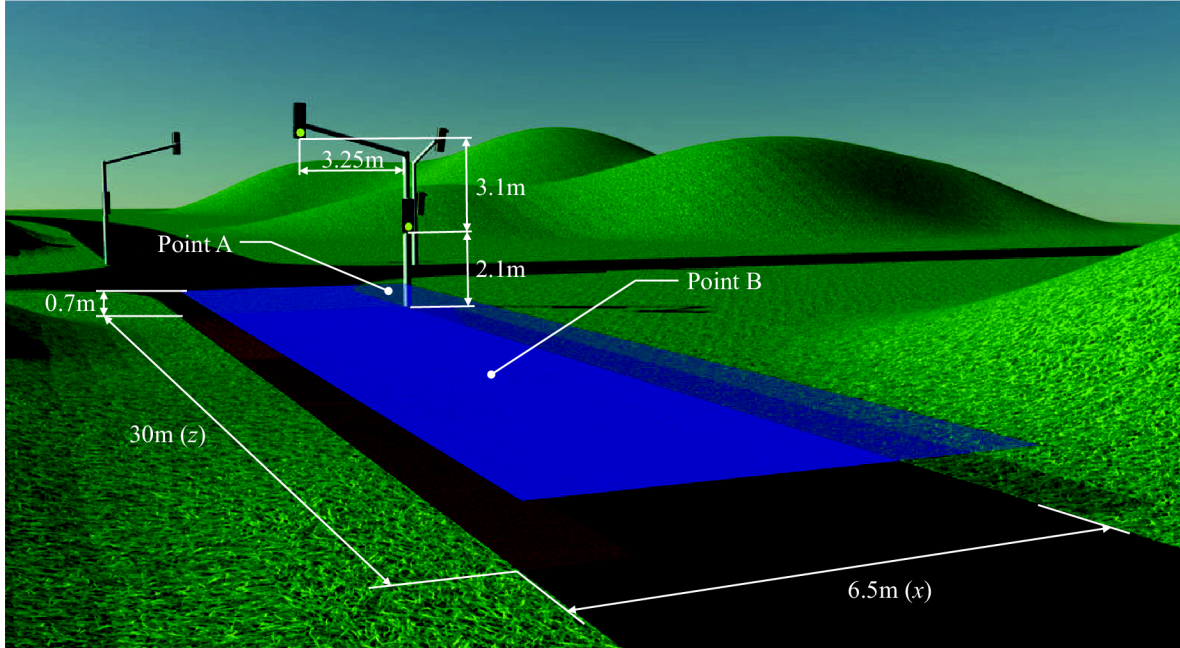


Figure 3.15: Crossroad model

The road dimensions meet the standard ČSN 73 6110, more specifically, the ground plane width x was set to 6.5m and the road length z under consideration to 30m illustrated as a red-colored rectangle [4]. Moreover, the proposed road area represented a reflection surface for the following simulation purposes. A blue-colored rectangle depicted in figure 3.15 illustrates a receiver plane at height 0.7m corresponding to headlight height of a typical vehicle.

The simulation set-up corresponded to the multi-path conceptual VLC system diagram illustrated in 3.10. The foregoing analysis assumed that a single wavelength was used for communication purposes. The devised set-up considered two 8-bit 5mm LED arrays. Each LED array was composed of LED groups which represented the bit depth of the array. The number of LEDs inside the array was directly given by $2^k - 1$, due to a symmetrical axis. The transmitter used two LED arrays with dominant wavelength 505nm, assembled at a height of 2.1m and 5.5m above ground (xz plane), with heading defined by the vector \vec{n}_{Tx} . Green lights of the traffic head were chosen in order to simplify the simulation. All the LED arrays transmitted the same information synchronously. The optical signal traveled through the optical channel between transmitter and receiver, undergoing path attenuation and reflections from the ground. For simulation purposes, a single reflection scenario from the ground surface was assumed. The reflection coefficient was set to $\rho = 0.08$, equal to the reflection coefficient of a worn asphalt surface, assuming a wavelength at 505nm [34]. The receiver was positioned at different places inside a rectangular ground plane 6.5m by 30m with a heading vector \vec{n}_{Rx} as illustrated in figure 3.15. The CIR of a single LED $h(t)$ can be

separated into two components, the first one due to the LoS contribution, and the second owing to the first order reflections on the ground surface.

$$h(t) = h^{\text{LoS}}(t) + h^{\text{Ref1}}(t). \quad (3.16)$$

The LoS contribution $h^{\text{LoS}}(t)$ can be computed directly using equation (3.17):

$$h^{\text{LoS}}(t) = H_{\text{Tx}}(n, \theta) H_{\text{Rx}}\left(\left\|\vec{d}_{\text{Rx}}\right\|, \psi\right) \delta\left(t - \Delta t_{\text{LoS}}\right), \quad (3.17)$$

where $\delta(\cdot)$ represents the Dirac delta function, Δt_{LoS} is time delay of the path between the transmitter and receiver given by the length of the path divided by the propagation speed (in this case, the speed of light). The signal arriving at the receiver after one reflection can be computed using equations (3.8), (3.5) and the reflection model R_{Lambert} given by equation (3.6). For the scenario under consideration, the ground surface was modeled as a pure Lambertian surface. The contribution from the first reflection path $h^{\text{Ref1}}(t)$ is expressed by (3.18):

$$h^{\text{Ref1}}(t) = \sum_{s1} \sum_{i=1}^{G_{\text{Ref1}}} H_{\text{Tx}}(n, \theta_i) H_{\text{Rx}}\left(\left\|\vec{d}_{\text{Rx},i}^{\text{Ref1}}\right\|, \psi_i\right) \times \\ R_{\text{Lambert}}\left(\rho, \Delta A_i, \left\|\vec{d}_{\text{I},i}^{\text{Ref1}}\right\|, \alpha_i, \beta_i\right) \delta\left(t - \Delta t_{\text{Ref1},i}\right), \quad (3.18)$$

where $s1$ specifies the number of reflection surfaces under consideration (for this purpose $s1=1$), G_{Ref1} specifies the number of grid elements ΔA used to approximate the reflection contributions and Δt_{Ref1} is the time delay associated with the path between transmitter, reflecting surface and receiver, computed as before.

As a proven performance metric to evaluate the signal reconstruction, the relative root mean square error E_{RMS} was used as stated in (3.13). The testing signal $v(t)$ was modeled by a sampled sinusoidal waveform with frequencies 1MHz and 10MHz. The sample rate of the generated signal complied with the Nyquist criterion. Figure 3.16 shows the general DC channel gain H_G expressed by (3.19) where a means the number of all transmitter arrays under consideration (in this case two emitter arrays).

$$H_G = \sum_a \sum_{m=1}^k \sum_{n=1}^{2^{m-1}} \left(H_{m,n}^{\text{LoS}} + H_{m,n}^{\text{Ref1}}\right). \quad (3.19)$$

Figure 3.17 shows the reconstruction error distribution over the receiver plane (blue rectangle in figure 3.15) for different emitter *HPA* and receiver *FOV*. Results, for signal frequency 1MHz and 10MHz, displayed larger error in front of the receiver. This is a natural property of the ODAC concept inducing distortion in the near field of the ODAC LED array. Signal

restoration in the emitter near field was also limited by receiver's narrow *FOV* as illustrated in figures 3.17a, 3.17b, 3.17e and 3.17f. Higher emitter *HPA* positively influenced the reconstruction error especially close to the traffic heads as depicted in 3.17b, 3.17d, 3.17f and 3.17h. Needless to say, the signal frequency itself increased the overall reconstruction error. Noticeable error fringes, in all figures, were a product of signal interference in the optical domain between the two traffic head emitters.

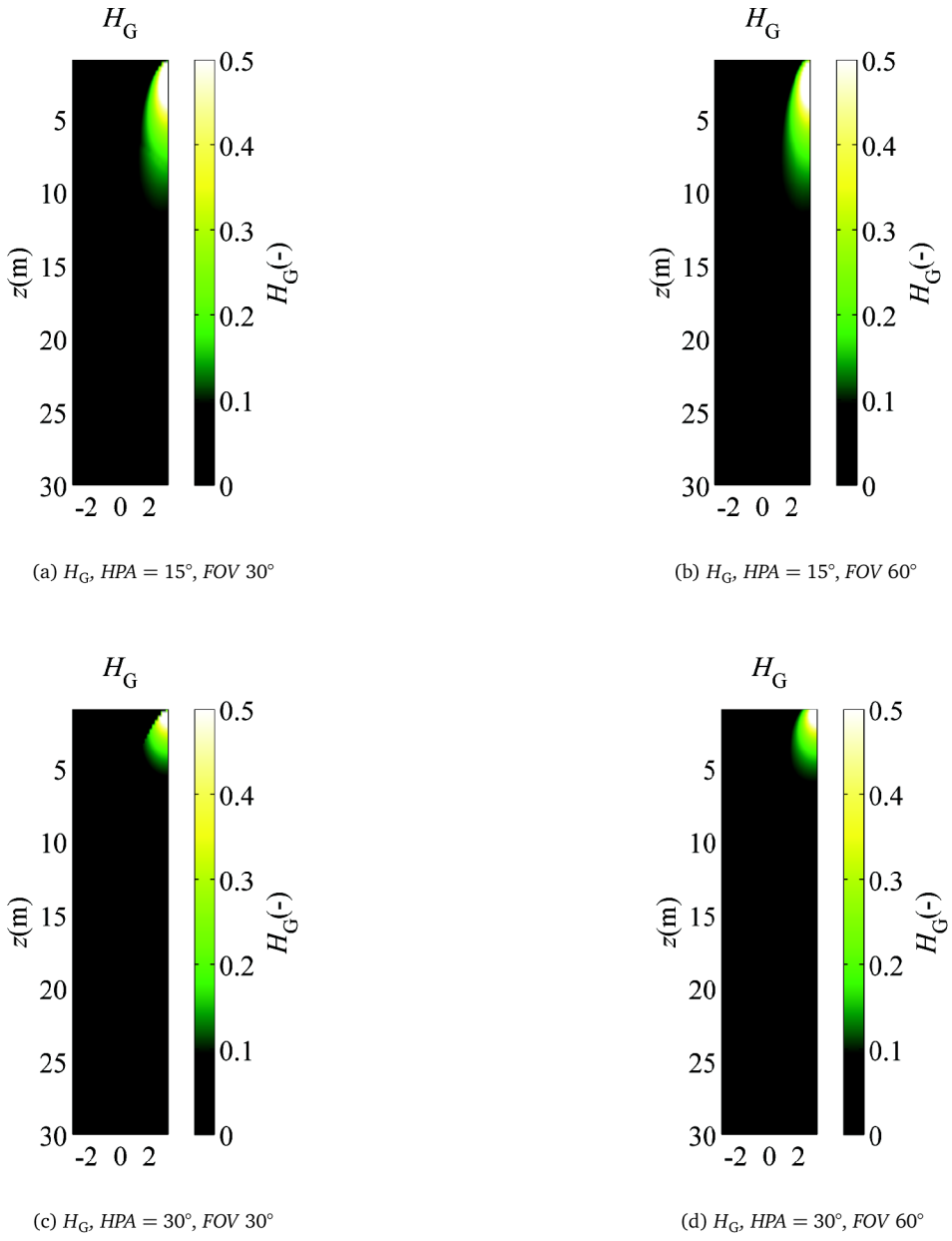
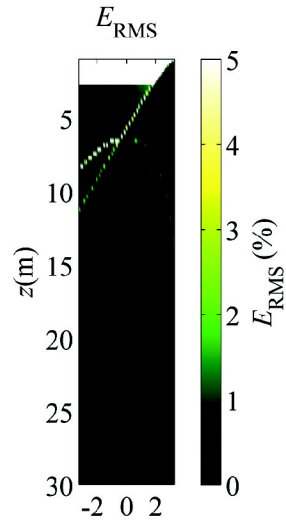
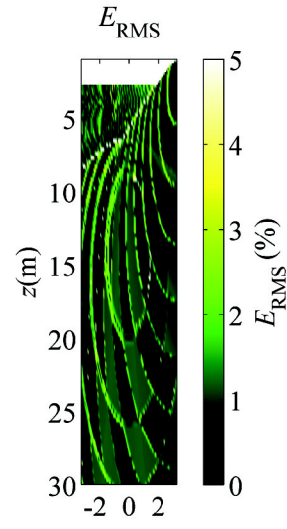


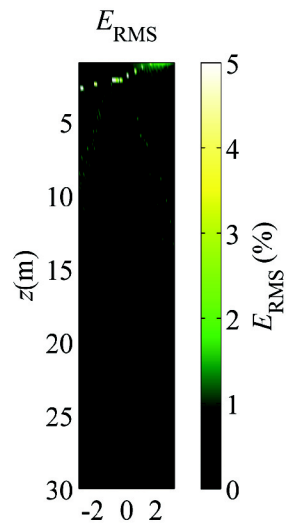
Figure 3.16: General DC channel gain H_G



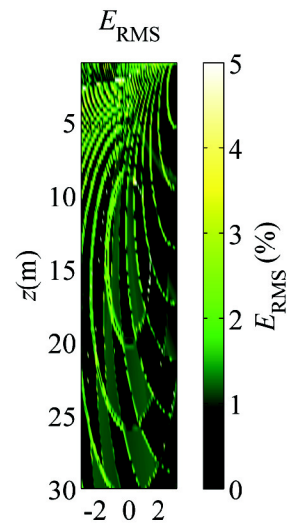
(a) 1MHz HPA = 15°, FOV 30°



(b) 10MHz HPA = 15°, FOV 30°



(c) 1MHz HPA = 15°, FOV 60°



(d) 10MHz HPA = 15°, FOV 60°

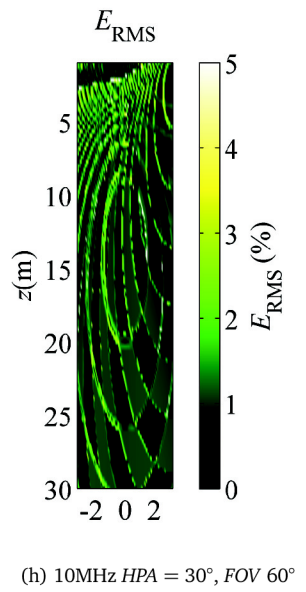
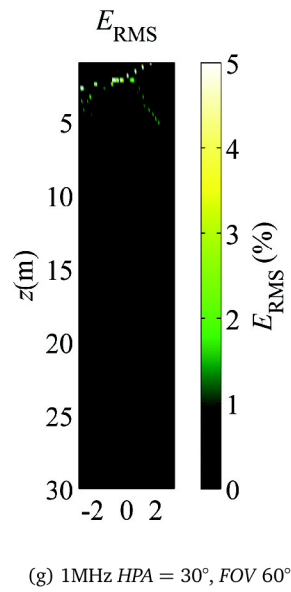
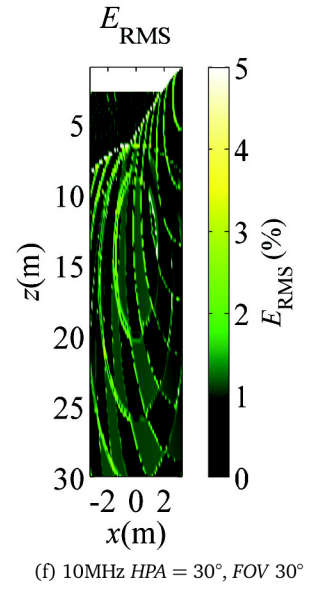
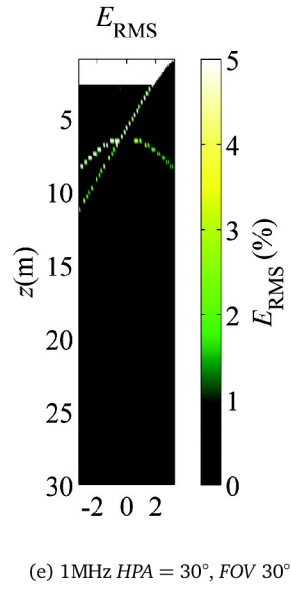


Figure 3.17: Signal reconstruction error E_{RMS}

Figure 3.18 shows the signal reconstruction error for determined points at the receiver plane (Point A and point B drawn in figure 3.15).

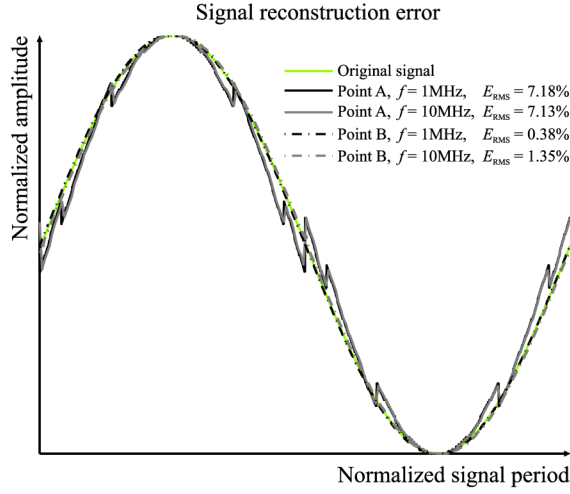


Figure 3.18: Reconstruction error ($HPA = 30^\circ$, $FOV 60^\circ$)

This section analyzed performance of the ODAC concept adapted to traffic lights representing a VLC system in ITS. The performance was evaluated using the relative error computed between the original signal and the reconstructed one. The presented results revealed ODAC performance for different emitter $HPAs$ (15° and 30°) and receiver (30° and 60°). ODAC performance was rigidly influenced by receiver geometrical set-up, emitter and receiver relevant parameters as well as the testing signal frequency [22].

3.6 ODAC system performance analysis for indoor set-up conditions

This part explores ODAC performance degeneration effects caused by the geometrical set-up and CIR for indoor conditions. In former sections relating to this topic, the effects on signal reconstruction error due to geometrical considerations of the set-up, assuming low data transmission scenarios, were investigated [20, 21]. The outdoor VLC model of the ITS crossroad using a similar performance evaluation metric was revealed in [22]. This section extends previous conclusions to the case of high data rate signal transmission, where the channel impulse response becomes of paramount importance. The assumed set-up scenario considered four luminaries in an empty room of $4m \times 4m \times 3m$ (length, width, and height). The modeling approach took into consideration the effects of the emitter HPA , the receiver FOV and channel impulse response, assuming a multi-path propagation model able to consider up to two reflection paths.

Figure 3.19 shows the conceptual diagram of the VLC system model under consideration. On the transmitter side, an arbitrary waveform generator produced a digital signal $v(t)$, represented by a set of k digital bit streams $B(t)$, which were used to modulate k independent groups of LEDs in an LED array. Quantization at the transmitter side was assumed to follow the standard approach: for k LED groups, the signal dynamic range was divided into $2^k - 1$

equal amplitude intervals. Assuming that the digital signals $B(t)$, all had the same amplitude and that the LEDs were driven uniformly for all the k groups, the digital weights were set by the number of LEDs in each group - following a binary weight distribution.

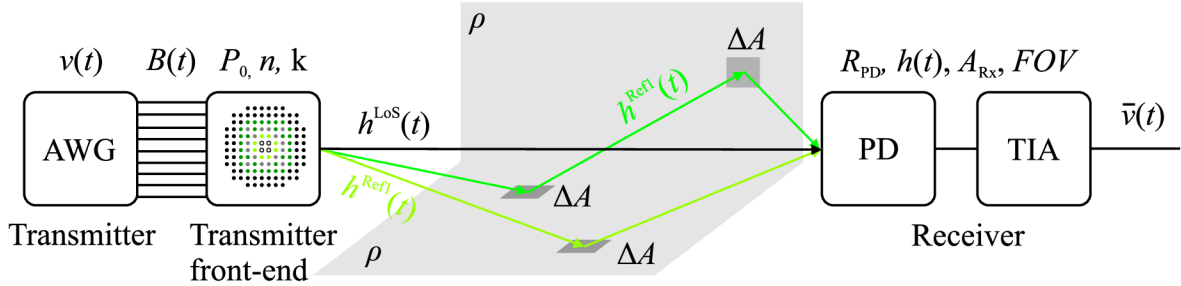


Figure 3.19: System model diagram

The transmitted bit streams were then combined on the channel and reach the input of the receiver (in this case, represented by PD and simple TIA). The recovered signal $\bar{v}(t)$ was a reconstructed replica of $v(t)$ with approximation error dependent on the bit depth of the array (the number of LED groups, k), and channel degradation effects. In a perfect channel, exempt from reflections, delays and constrained FOV , the approximation error would be lower bounded by $LSB/2$, where LSB represented the strength of the least significant bit. Assuming the channel impulse response $h(t)$ of one LED, the reconstructed signal could be determined by adding the convolutions of the signals $B(t)$ with the LED's individual impulse responses, as stated in (3.10). A detailed geometrical set-up under consideration can be seen in figure 3.20.

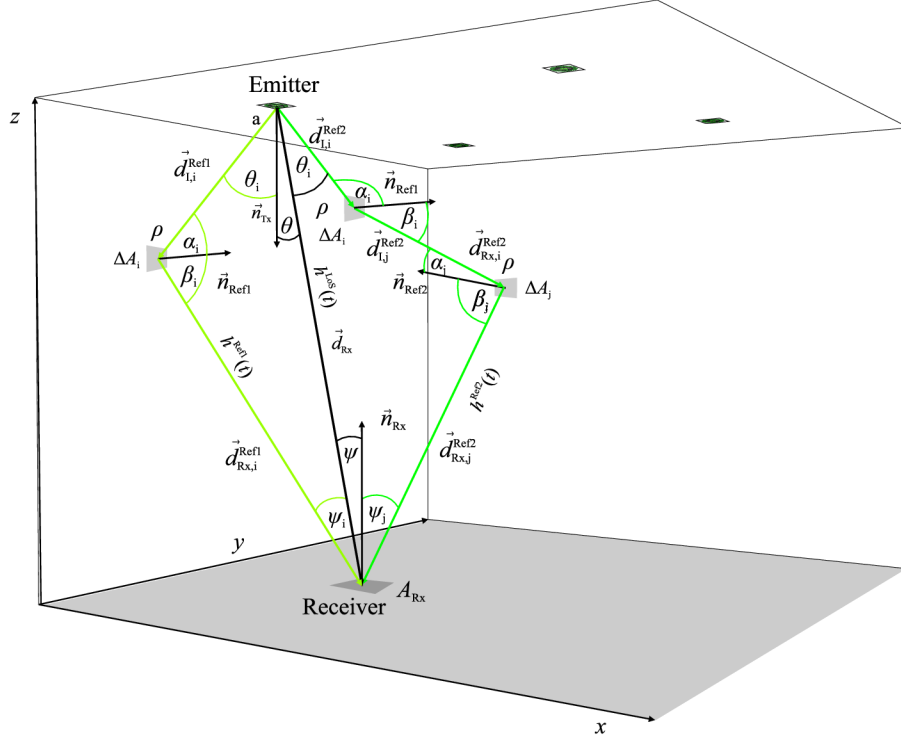


Figure 3.20: Detailed set-up

As stated in equation (3.10) the reconstruction error will depend on the optical channel, this implies dependence on the CIR, the geometrical arrangement between transmitter and receiver, and the presence of reflecting elements. The assumed set-up considered four 8-bit depth LED array luminaries. Each LED array was formed by k LED groups, where k represents the bit depth of the array. Inside each group, the number of LEDs depended on the symmetries of the topology. For one axis symmetric 8-bit depth LED arrays, the overall number of LEDs inside the array was directly given by $2^k - 1$. For the present case, the number of LEDs inside each array was 255 (bit 0 = 1 LED, bit 1 = 2 LEDs, bit 3 = 4 LEDs, (...), bit 7 = 128 LEDs), having a single symmetrical axis.

The transmitter used four LED arrays, located at a height z (3m) above the ground plane (xy plane), with heading given by the normalized vector \vec{n}_{Tx} . All LED emitters under consideration sent the same information synchronously. The optical signal which went through the optical channel was affected by path attenuation and reflection from the walls. Simulation assumed a double reflection scenario from surrounding walls and the ceiling. The reflection coefficient of dominant wavelength 475 nm was set to $\rho = 0.8$, which corresponds to white paint on a plaster surface [58]. The receiver was swept at 10,000 different positions inside a 4m by 4m square on the ground plane ($z = 0$), with a heading vector \vec{n}_{Rx} . The CIR $h(t)$ can be divided into three components; the first one owing to the LoS contribution, the second

and third, due to the first and second order reflections from walls, respectively.

$$h(t) = h^{\text{LoS}}(t) + h^{\text{Ref1}}(t) + h^{\text{Ref2}}(t). \quad (3.20)$$

The LoS contribution $h^{\text{LoS}}(t)$ can be directly computed using equation (3.17). The signal impinging the receiver after the first reflection is possible to compute using equations (3.18) and including a suitable reflection model. For simulation purposes, a white plaster wall was modeled as a pure Lambertian radiator. The second reflection contribution can be expressed using the same analogy as in the former case. The second reflection contribution $h^{\text{Ref2}}(t)$ is given by equation (3.21).

$$h^{\text{Ref2}}(t) = \sum_{s1} \sum_{s2} \sum_{i=1}^{G_{\text{Ref1}}} \sum_{j=1}^{G_{\text{Ref2}}} H_{\text{Tx}}(n, \theta_i) H_{\text{Rx}} \left(\left\| \vec{d}_{\text{Rx},j}^{\text{Ref2}} \right\|, \psi_j \right) R_{\text{Lambert}} \left(\rho, \Delta A_i, \left\| \vec{d}_{\text{L},i}^{\text{Ref2}} \right\|, \alpha_i, \beta_i \right) \times \\ R_{\text{Lambert}} \left(\rho, \Delta A_j, \left\| \vec{d}_{\text{L},j}^{\text{Ref2}} \right\|, \alpha_j, \beta_j \right) \delta(t - \Delta t_{\text{Ref},ij}), \quad (3.21)$$

where $s2$ specifies the number of reflection surfaces undergoing the second order reflection, G_{Ref2} specifies the number of second order grid elements, \vec{d}_i^{Ref2} means incident direction of the second order reflection, $\vec{d}_{\text{Rx}}^{\text{Ref2}}$ is the direction from the second reflection surface to the receiver, Δt_{Ref2} is the time delay associated with the path between transmitter, reflecting surfaces and receiver, and index j is associated with the number of second reflection paths, computed as before.

The numerical computation process can be conveniently modified in order to investigate the symmetric nature of the set-up. Hence, symmetric configurations required simulation of one luminaire, where the other luminaires were rotated replicas of the first. Eventually, the recovered signal could be obtained using equation (3.10). Particularly, the signal was a combination of the contribution from each LED in the array and geometrical dependencies of the optical signal propagation. The procedure to compute CIR followed the standard time histogram approach, where each time bin accumulated all contributions with similar delay. The time bin resolution of the CIR was in this way linked to the area grids used for reflection modeling, having in mind that each bin interval must satisfy the constraint $c\Delta t > \sqrt{\Delta A}$ [10]. In practice, a CIR computation for simulation purposes was based on a modified iterative algorithm arising from Barry's study on CIR modeling implemented by using MATLAB software. More specifically, the MATLAB parallel computing toolbox, in this case using 10 pools, was employed in order to reasonably carry out demanding CIR computations of the second reflection order for 10,000 reflection elements and receiver positions.

In wireless communication systems the *EVM* is perhaps the most common figure of merit. In this case, *EVM* was chosen as the suitable metric to evaluate the overall performance of the setup under consideration. Needless to say, the setup does not include any modulation

scheme, as commonly found in RF transceiver performance testing. The evaluation rather used EVM as a measure of difference between the measured signal and the reference signal, as defined in equation (3.22). Basically, EVM corresponds to previously used E_{RMS} . The normalized reference signal $v(t)$ and the recovered signal $\bar{v}(t)$ on the receiver side were assumed. The time offset and frequency offset was removed where M is data length.

$$EVM = \sqrt{\frac{\sum_{t=1}^M \|\bar{v}(t) - v(t)\|^2}{\sum_{t=1}^M \|v(t)\|^2}}. \quad (3.22)$$

The simulation set-up assumed the modeling approach described in the previous sections of the thesis. The signal $v(t)$ was modeled by a quantized sinusoidal waveform with frequencies ranging from 1MHz to 100MHz. The sample rate of the generated signal was set to comply with the Nyquist criterion, in this case to 10GHz. Obviously this is not achievable with present commercial LEDs but it may disclose some relevant considerations for devices currently under development (mLEDs bring bandwidth up to 400MHz). The achieved results are depicted in figures 3.21 to 3.23. Figures 3.21b, 3.21c and 3.21d show the CIR for each group of LEDs inside the array for three different receiver positions illustrated in 3.21a. Specifically, figure 3.21b depicts the CIR in the room corner, figure 3.21c and figure 3.21d illustrate CIRs under one luminaire and in the middle of the room, respectively. It is worth noting that the CIR at different positions inside the room will exhibit different contributions due to multiple reflections. These CIR dependencies gave rise to reconstruction errors which became more pronounced as the signal frequency increased. This study investigated the effects of path delays on the received signal using the ODAC concept.

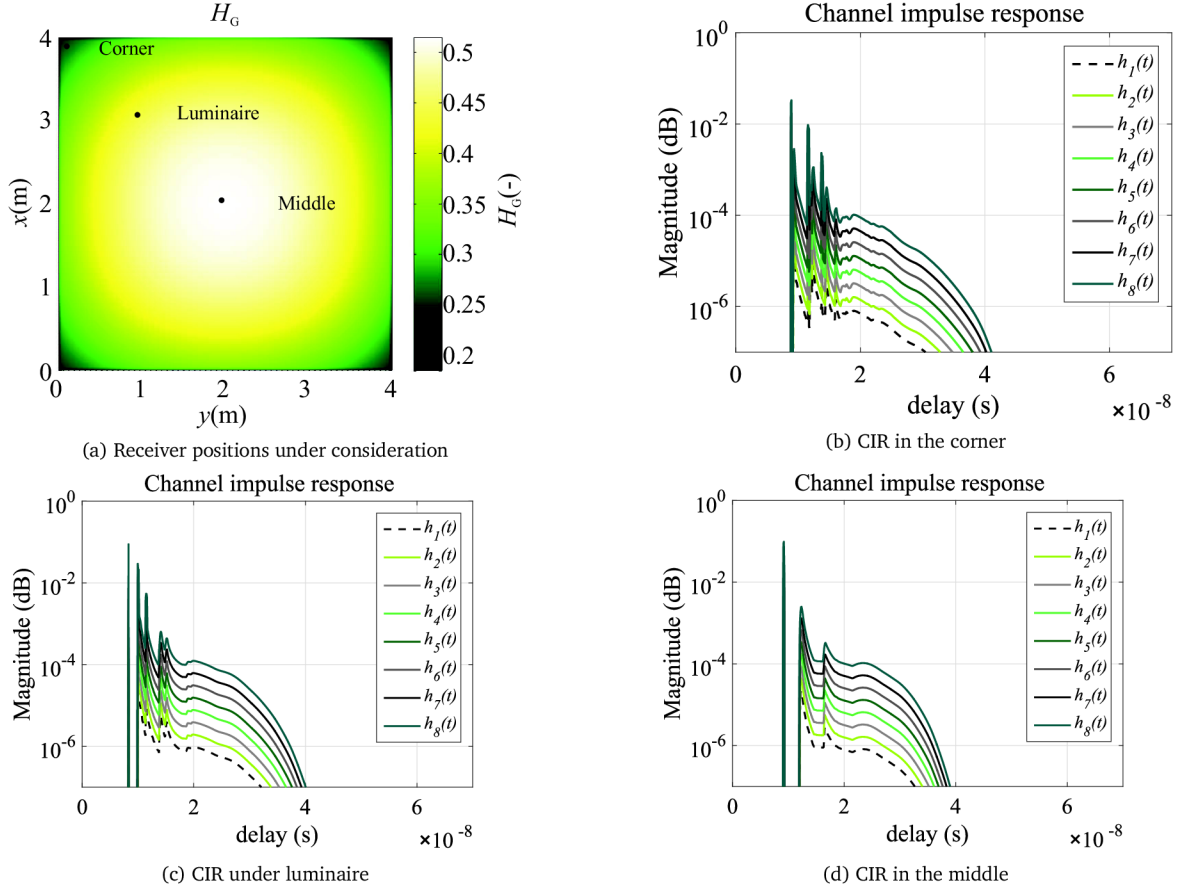


Figure 3.21: Channel impulse response (CIR), $HPA45^\circ$, $FOV60^\circ$

Figures 3.22 and 3.23 show the general DC channel gain H_G , here defined as the sum of all LED CIRs from directed and reflected paths as stated in equation (3.23) and the reconstruction error distribution for the receiver in different positions over the ground plane. The EVM was computed using equation (3.22), for two different frequencies, 1MHz and 100MHz, with different transmitters $HPAs$ and receivers $FOVs$. As in previous contributions, the DC channel gain depended strongly on HPA and FOV , having a major influence with larger HPA , meaning sources with wide radiation patterns. Usually this is the case for lighting systems where light uniformity is of paramount importance for better user comfort in terms of rendering conditions.

$$H_G = \sum_a \sum_{m=1}^k \sum_{n=1}^{2^{m-1}} \left(H_{m,n}^{LoS} + H_{m,n}^{Ref1} + H_{m,n}^{Ref2} \right), \quad (3.23)$$

where H^{Ref2} means DC channel gain of the second reflection path.

Figure 3.22 shows what can be expected for confined sources with reduced HPA . As can be seen, the reconstruction error did not change much for different receiver $FOVs$, which corresponded to better conditions for transmission. Also noticeable, there were some interference

patterns arising from the multiple sources and reflecting surfaces, which became more evident for higher frequencies. These patterns resulted from wave interference phenomena, as for frequencies close to 100MHz, the wavelength became comparable to the room dimensions. Figure 3.23 shows the *EVM* for sources with high *HPA* (45°). For this case, the error dependence on the receiver *FOVs* was self-evident, showing different behaviors for 1MHz and 100MHz. This was due to the relevance of the delay terms for both frequencies. The errors also increased with frequency as before, but in this case the *EVM* reached nearly 50%.

The main conclusion which can be extracted from these results is that under standard lighting conditions, communication impairments for systems employing the ODAC concept became relevant as the frequency increased. These problems can be mitigated by using photo-detectors with reduced *FOVs* or even concentrator lenses at the receiver side.

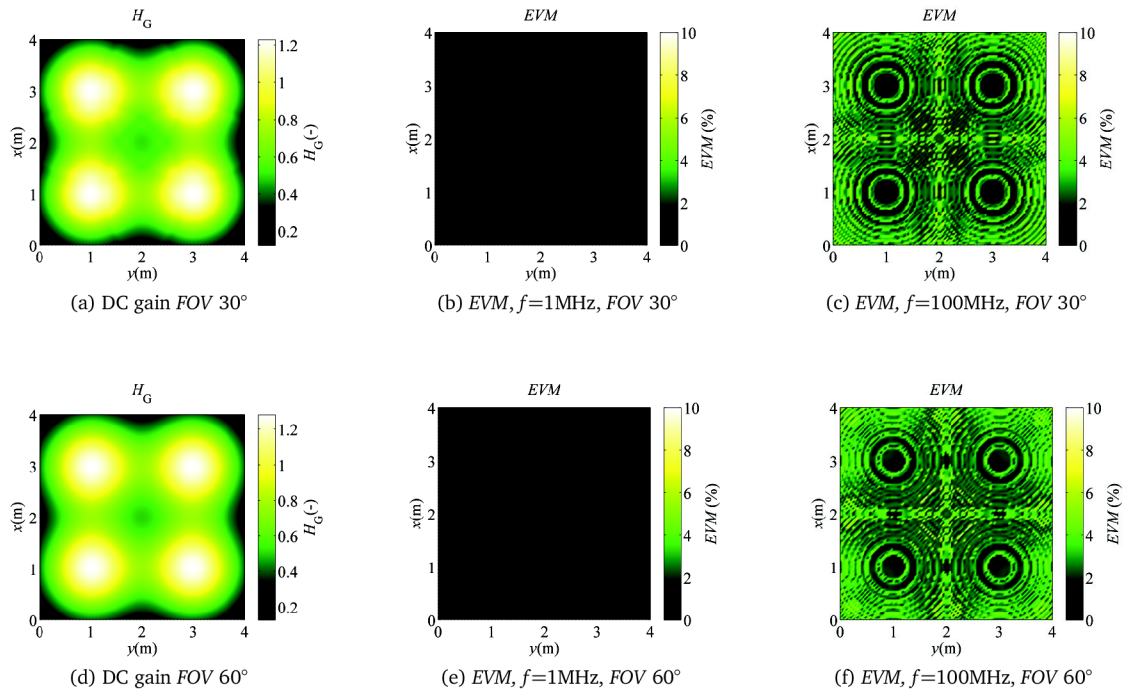
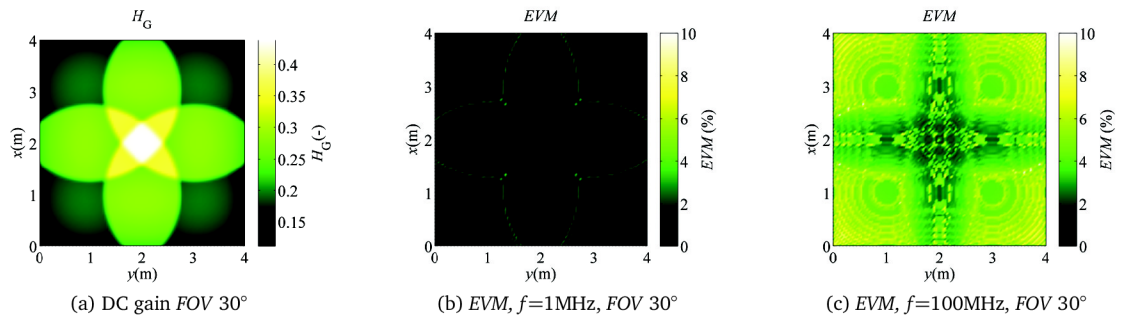


Figure 3.22: Four luminaires indoor set-up, *HPA* 15°



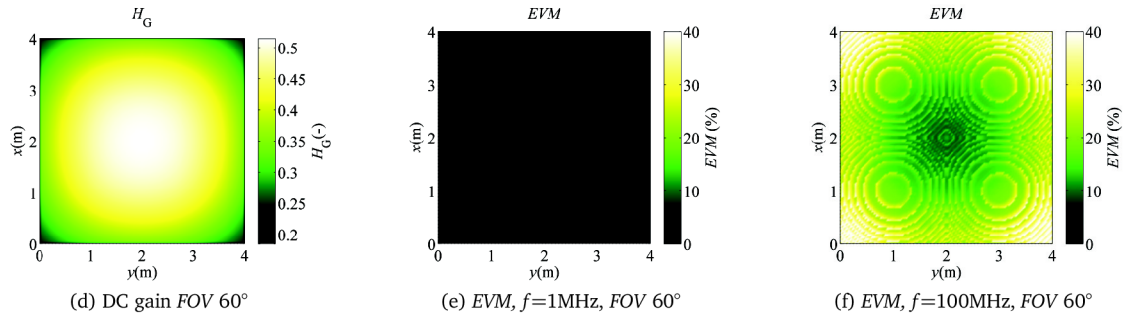


Figure 3.23: Four luminaires indoor set-up, HPA 45°

Figure 3.24b shows how the CIR affected the signal reconstruction for a 100MHz sinusoid at the three different receiver positions depicted in figure 3.24a (black dots inside the black circles). As explained before, the reconstruction error EVM was computed between the originally transmitted signal $v(t)$ and the reconstructed signal $\bar{v}(t)$ on the receiver side. Similarly, figure 3.25b shows the signal reconstruction for a composite signal (sum of two sinusoids with 100MHz and 200MHz frequencies) at the three positions illustrated in figure 3.25a. The phase shift effect caused by the multiple peaks in the CIR is clearly visible. This effect was more pronounced in the corner and under the luminaire cases, where the peaks due to longer paths had higher power, leading to pronounced phase distortion for the composite signal. Figure 3.26 depicts EVM dependence on signal frequency, where the EVM 's averaged value inside each circle was considered (the circles are illustrated in figure 3.24a). Specifically, the averaging areas under inspection were defined by the coherence distance between two error fringes representing local maximum errors.

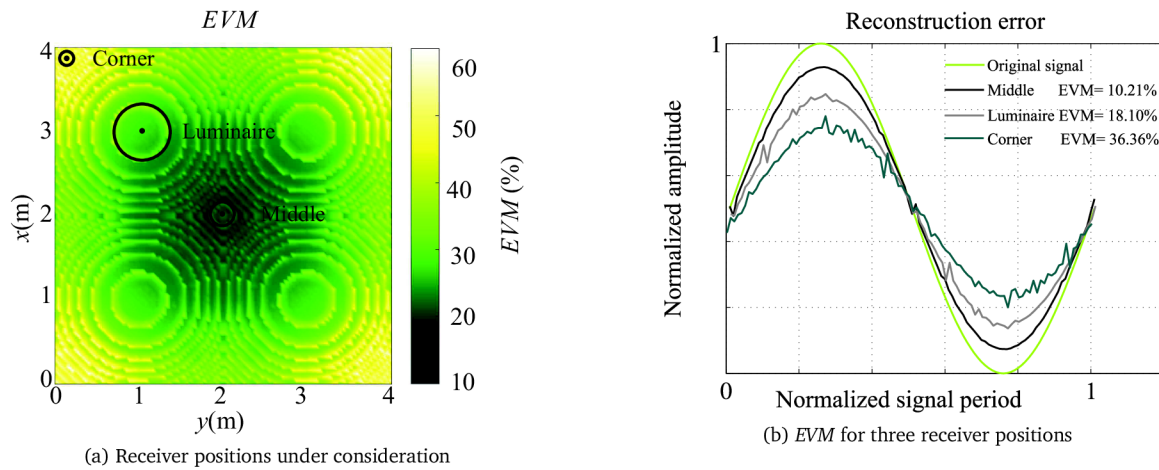


Figure 3.24: EVM , $f = 100\text{MHz}$, HPA45°, FOV60°

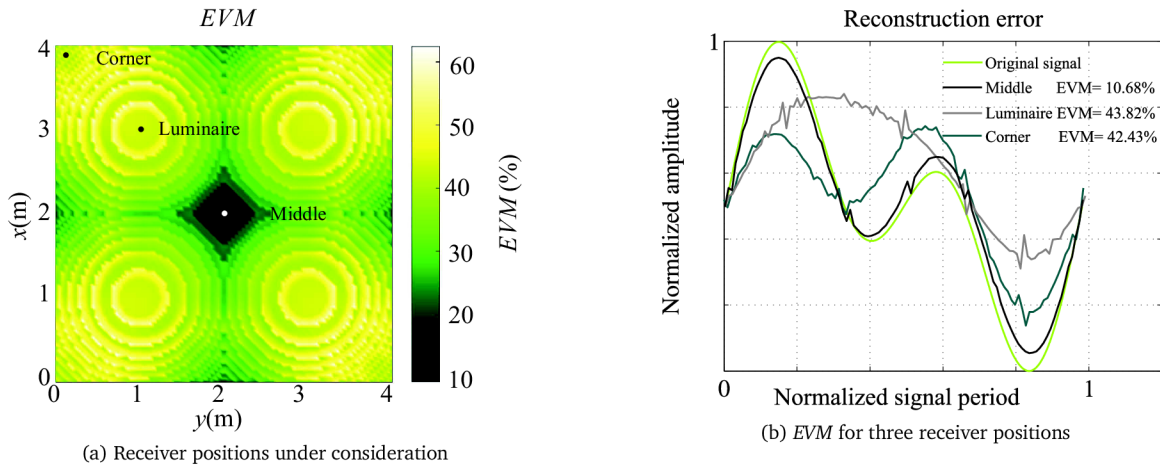


Figure 3.25: EVM , $f = 100\text{MHz}+200\text{MHz}$, $HPA45^\circ$, $FOV60^\circ$

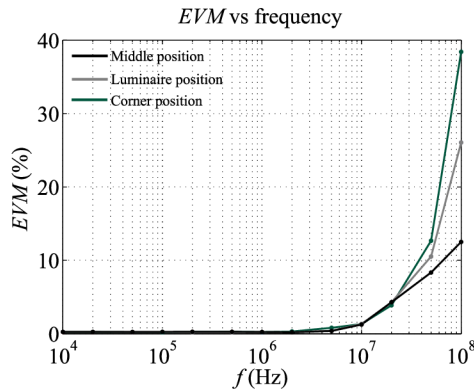


Figure 3.26: EVM frequency dependence

The performance was evaluated using the EVM of the reconstructed signal by means of comparison. Simulated conditions included geometrical set-up considerations, emitter and receiver relevant parameters and channel impulse response. The achieved results revealed that standard lighting conditions, advocating the usage of dispersive lighting sources, posed severe limitations on bandwidth for systems employing this concept. On the other hand, light sources with low HPA , that is, with confined lighting patterns, offered better conditions for high bandwidth achievement [23].

4 ODAC FRONT-END DESIGN AND PERFORMANCE EVALUATION

This chapter is dedicated to the ODAC transmitter hardware design and its experimental performance testing. Specifically, two ODAC samples proposed in previous simulations are considered where the first transmitter employs white LEDs in a compact PLCC6 package while the second sample uses square-shaped 7.62mm blue LEDs. The performance evaluation is based on both dynamic and static tests. The experimental work looks into linearity errors, impulse, and frequency response of both ODAC samples. Moreover, the PLCC6 ODAC sample is evaluated as a part of an FPGA-based real time VLC system.

4.1 VLC ODAC emitter

The ODAC concept is based on using groups of LEDs arranged in an array to transmit discrete optical signal levels. The radiation pattern of these LED groups adds together on the optical domain enabling the transmission of optical analog signals. Since the LED driving signals are digital, both constant current and PWM dimming schemes can be easily implemented.

4.1.1 ODAC concept

In terms of the ODAC architecture, basically, it is possible to distinguish two basic ODAC architectures as was mentioned earlier. The first approach uses a fixed number of LEDs per bit. Because the number of LEDs per group, n , is identical, the DAC operation is achieved by driving each group with different current levels, following the usual distribution of binary weights. The transmitted optical signal results from the combination of the output light of k groups. Thus, the overall number of LEDs inside the array is directly given by $k \cdot n$.

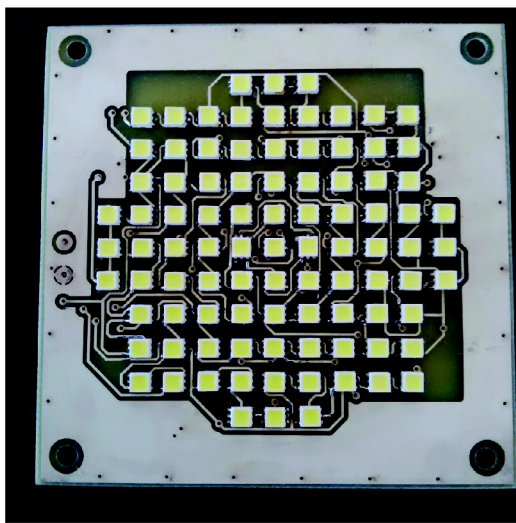
The second approach used in this case employs LED groups with a different number of LEDs. This means that the LEDs are driven with the same current and the binary weights are set by the number of LEDs in each group. The total number of LEDs inside the array corresponds to $2^k - 1$, where k is the ODAC front-end resolution in bits. This latter ODAC architecture is the one chosen for this work since it imposes the same operating conditions for all LEDs in the array. Unlike a conventional VLC emitter, where performance is affected by the LEDs inherent nonlinearity, the ODAC-based transmitter offers better linearity and no need of EDAC in the driver stage. Furthermore, the recent trends in general lighting seems to be in line with the ODAC concept in terms of multiple LED array designs or the use of COB LEDs for higher luminous output. On the other hand, the ODAC concept may suffer from a significant quantization error for small resolutions (arising from the ODAC bit depth, i.e. the total number of LED groups in the ODAC emitter array), lower modulation bandwidth, and geometrical distortion.

4.1.2 ODAC hardware sample design

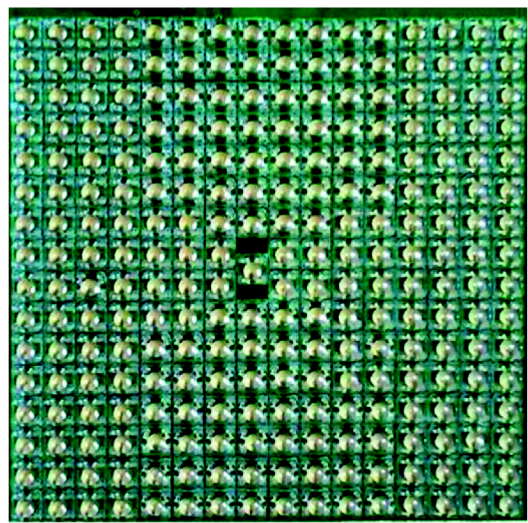
Figure 4.1 depicts the hardware implementation of both proposed ODAC front-ends for VLC applications. Specifically, the first ODAC front-end (figure 4.1a) employs off-the-shelf white LEDs in a PLCC6 housing. The second ODAC front-end uses conventional discrete blue LEDs encapsulated in a 7.62mm square package as depicted in figure 4.1b. The front-ends are made of double layered FR4 printed circuit board (PCB), where the top layer is dedicated to the LEDs and the bottom layer to the driving circuits.

As both front-ends have 8-bit depth, the overall LED number inside each emitter array is 255 which corresponds to $2^k - 1$. In the array, the LSB is represented by one LED, while the most significant bit (MSB) is formed by 128 LEDs. The second ODAC emitter (see figure 4.1b) is formed by 255 LED packages having an active area 122mm x 122mm.

The PLCC6 ODAC front-end(figure 4.1a) comprises of 93 PLCC6 LED packages, each containing three LED chips. In order to keep the ODAC front-end symmetry, the outer LED triplets are placed on the PCB having just one LED chip wired as can be seen in figure 3.4e. Thanks to the PLCC6 surface mount technology, the circular active area dimensions of the second front-end are reduced to 60mm x 60mm. This supports a better uniformity of the optical intensity displacement in the near field radiation area.



(a) PLCC6 white LED ODAC front-end



(b) 7.62mm square blue LED ODAC front-end

Figure 4.1: ODAC hardware samples

Figure 4.2 depicts the ODAC emitter electrical driving circuit common for both designs. For the reason of circuit simplicity and due to the LEDs' low modulation bandwidth, a simple NPN transistor down side switch (black rectangle in figure 4.2) was chosen as a sufficient LED driver circuit. Each driver element contains: a fast switching BJT NPN transistor MMBT 2369A (Q), a resistor (R_B) that sets the current to the transistor base, a resistor (R_S) that acts as shunt resistor to discharge electrons from transistor base and speed up the transistor

turn-off time, and a Schottky diode (D) connected as a Baker clamp to prevent the transistor from saturating and thus improving its recovery time.

The ODAC emitter contains 19 of these driver elements, where the first five bits have one driver per LED group, while the more significant LED groups require more driver blocks. Specifically, the maximum switching load for one driver element in the ODAC array was experimentally set to two LED strings in parallel, each containing 8 LEDs, per one driver. Thus, 2, 4 and 8 driver block elements were employed for the 6th, 7th and 8th bit, respectively.

In the case of the PLCC6 white LED ODAC front-end the value of resistors R1-R8 was chosen with regard to the LED forward current, here set approximately to 20mA per one LED string. For these driving conditions, the average luminous intensity of one LED ASMT-YWB1-NGJB2 (6500K) is 7600mcd, according to the manufacturer datasheet.

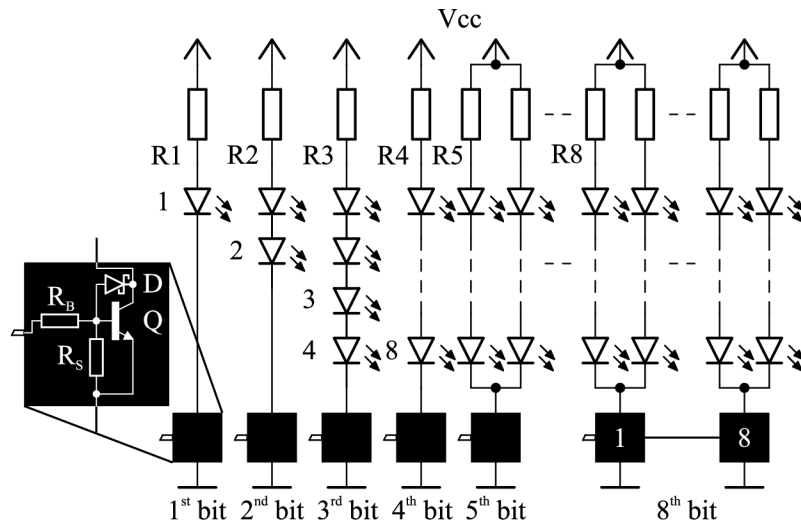


Figure 4.2: ODAC front-end electrical driver circuit

4.2 VLC optical receiver

Figure 4.3 depicts a simple low noise wide-band VLC optical receiver simulated and designed particularly for this experimental performance testing. The key part of the receiver forms a PIN PD FDS100 with large active area of 3.6x3.6mm suitable for VLC applications. The key part of the receiver forms a PIN PD FDS100 with a large active area of 3.6x3.6mm suitable for VLC applications. The signal amplification is carried out by an operational amplifier (OPA657) in transimpedance stage having variable gain setting. The second amplification and filtering stage exploits the operational amplifier OPA657 as well. The receiver offers a bandwidth of more than 30MHz, in this case a sufficient bandwidth, depending on transimpedance gain settings.

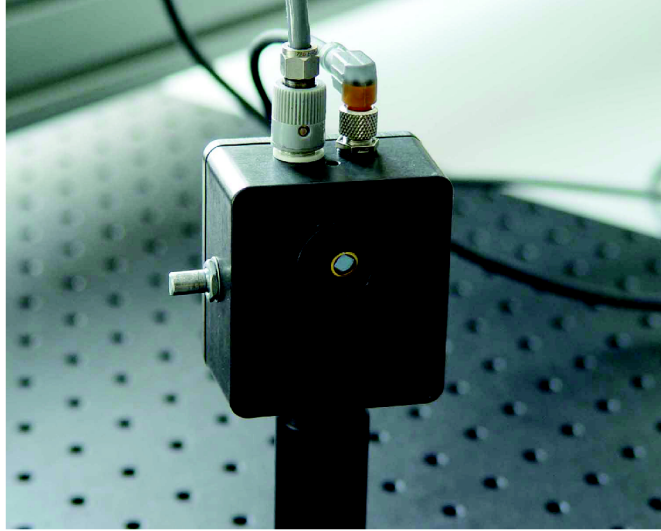


Figure 4.3: Wide-band optical receiver

4.3 Signal reconstruction error performance

This section explores the ODAC error performance in terms of signal reconstruction error considering both static and dynamic reconstruction tests.

4.3.1 Static signal reconstruction tests

The ODAC performance tests evaluated the static on-axis signal reconstruction error dependence on the distance x between emitter and receiver. A measurement chain set-up for the static scenario is illustrated in figure 4.4. Reconstruction error performance evaluation was based on periodic signals, more specifically, a ramp-shaped signal was used. On the emitter side the PLCC6 LED array was sequentially fed by input digital vector ranging from 0 to 255 which represented time independent ramp input signal $\bar{v}(t)$. On the receiver side, the optical signal was captured by an optical power meter working at a dominant wavelength of 505nm.

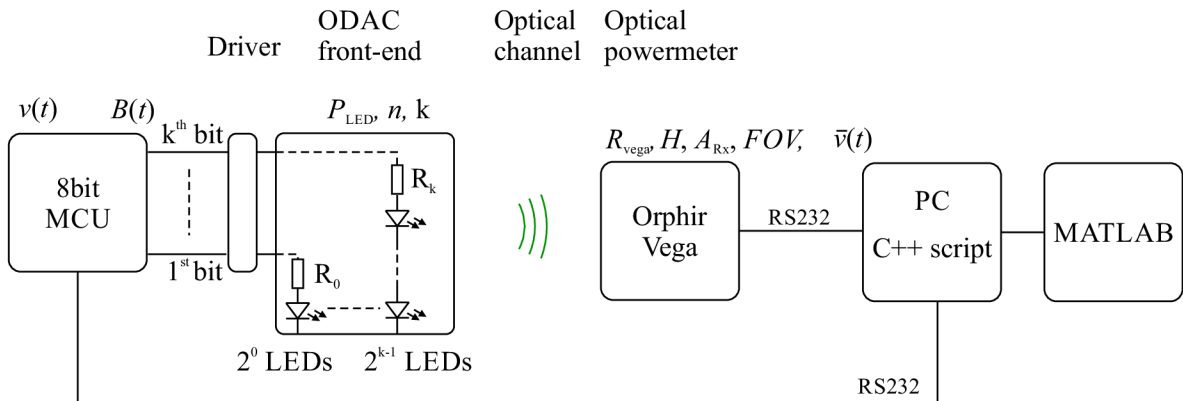


Figure 4.4: Static tests set-up

Used instruments

- 8-bit MCU-based ODAC emitter driver
- ODAC white PLCC6 LED front-end
- Ophir Vega optical powermeter
- Power supply Diametral P230R51D

The corresponding optical power was then measured on the receiver side where the receiver was placed at distances 0.05m and 0.5m on axis x , heading to the emitter array. The test under consideration inspected the time independent relation between the input signal and captured output optical power. The captured signal on the receiver side can be expressed using equation (4.1). The presented tests demonstrates the signal distortion in the near field area of the PLLCC6 emitter, which is natural for ODAC-based emitters. As can be seen in figures 4.5a and 4.5b the measured data more or less fits the simulated expectations.

$$\bar{v}(t) = \left[R_{\text{Vega}} \sum_{m=1}^k \sum_{n=1}^{2^m-1} B_m(t) H_{m,n} P_{\text{Tx},m,n} \right] + n_0, \quad (4.1)$$

where R_{Vega} is Ophir Vega responsivity and n_0 represents real noise contribution previously neglected for simulation purposes.

The black line in the figures indicates an ideal output optical power dependence on the input word represented by digital input vector $B(t)$ (see figure 4.5). The green line represents the simulated signal and the gray curve the truly captured signal. For the purpose of signal reconstruction error evaluation, the relative root mean square error E_{RMS} was used. Then, the reconstruction error E_{RMS} depends on channel impairments, ODAC quantization error and ODAC distortion error induced by the geometrical set-up between ODAC front-end and the optical receiver. Whereas the root mean square error E_{RMS} for the distance 0.5m acquired a value of 0.79%, the error at the distance 0.05m was naturally much higher, particularly 6.06%.

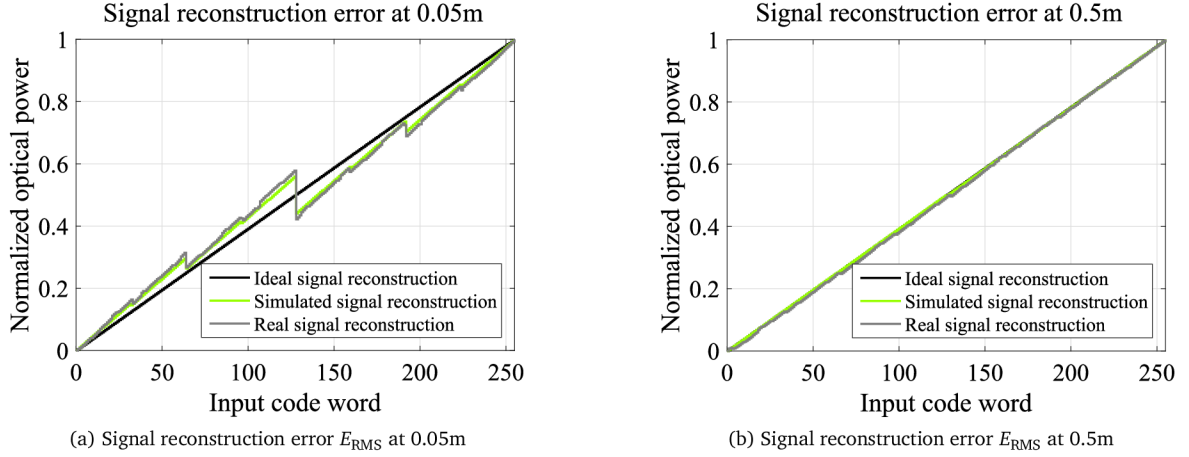


Figure 4.5: Static signal reconstruction error

4.3.2 Dynamic signal reconstruction tests

Figure 4.6 depicts a conceptual diagram of the experimental set-up. The evaluation board FPGA Virtex6 ML605 was programmed to generate a signal $v(t)$ which was represented by a set of bit streams $B(t)$, all having the same amplitude. These digital bit streams drove k independent LED groups in an ODAC emitter array. The transmitted bit streams were merged on the optical channel. Both ODAC front-ends under consideration employed a binary weighted approach as can be seen in figure 4.6. The optical signal impinged the optical receiver where the recovered signal $\bar{v}(t)$ was a reconstructed clone of original signal $v(t)$.

Reconstruction error E_{RMS} depended on optical channel impairments, ODAC quantization error, and ODAC distortion error induced by the geometrical set-up between the ODAC front-end and the optical receiver. The receiver side used PIN photo-diode FDS100 followed by an operational amplifier (OPA657) in gain variable transimpedance stage. The recovered signal $\bar{v}(t)$ was captured by a scope (Tektronix TDS2000C) and data was imported to MATLAB for further offline signal processing. Since the channel impulse response (CIR) of each LED in the array is given by $h(t)$ the recovered signal $\bar{v}(t)$ at the experimental chain end can be expressed by equation (4.2):

$$\bar{v}(t) = \left[R_{PD} \sum_{m=1}^k \sum_{n=1}^{2^m-1} B_m(t) * h_{m,n}(t) P_{Tx,m,n} \right] + n_0. \quad (4.2)$$

Performance evaluation is based on periodic signals to facilitate comparison between the original and the reconstructed signal version. In this case, a ramp-shaped signal having frequencies 1kHz and 98kHz was used. The normalized versions of $v(t)$ generated on the transmitter side and $\bar{v}(t)$ captured on the receiver side were considered.

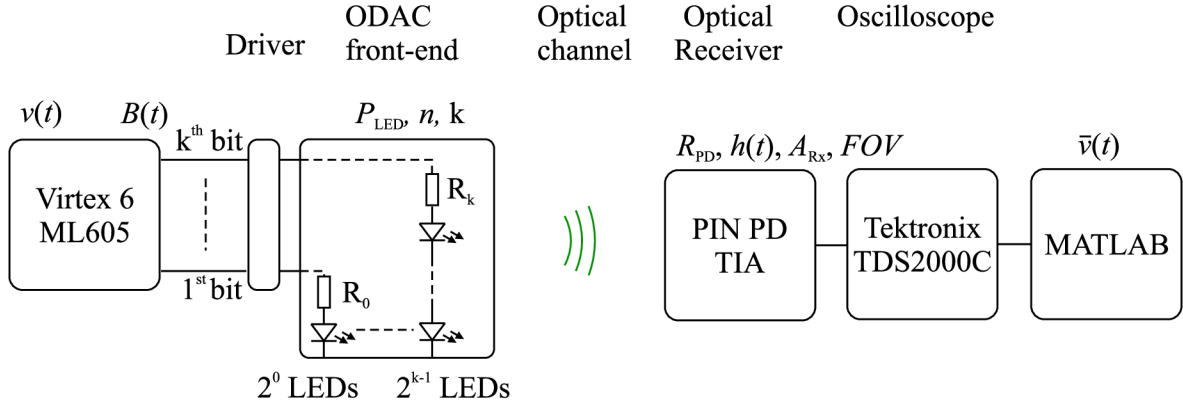


Figure 4.6: Dynamic tests set-up

Used instruments

- Xilinx Virtex 6 ML605
- ODAC white PLCC6 LED front-end
- ODAC 7.62mm blue LED front-end
- Optical receiver - FDS100 + TIA
- Tektronix TDS2000C
- Power supply Diametral P230R51D

Figure 4.7 illustrates reconstruction error of both ODAC samples. Specifically, in figure 4.7a and figure 4.7b the comparison between normalized versions of the reconstructed signal $\bar{v}(t)$ (green and gray curves) and the original signal $v(t)$ (black curve) is shown. Gray-colored curves in figure 4.7a illustrate huge E_{RMS} for the ODAC emitter employing discrete blue LEDs placed at a distance of 0.05m. This excessive error, in percentages 29.33% and 27.77% for frequencies 1kHz and 98kHz, respectively, was caused by the emitter's higher array dimensions inducing distortion in the emitter near field.

In the case of the PLCC6 ODAC emitter, the green-colored curves show typical values of E_{RMS} . Particularly, the E_{RMS} was 4.06% for signal frequency 1kHz and 4.01% for signal frequency 98kHz. As can be seen in figure 4.7b for a distance of 0.5m, the blue LED ODAC emitter does not suffer from excessive E_{RMS} anymore. This fact is confirmed in figure 4.7c showing E_{RMS} dependence on the distance between emitter and optical receiver. As an acceptable E_{RMS} limit, $E_{\text{RMS}} = 5\%$ was considered. In the case of the blue LED front-end, this limit lies around a distance of 0.4m. Naturally, E_{RMS} increases depending on signal frequency. It is obvious in the case of the PLCC6 ODAC front-end where the slow yellowish component limited the bandwidth. The E_{RMS} for the 1kHz and 98kHz ramp signal was 0.90% and 4.81%, respectively, as illustrates figure 4.7b. Furthermore, an angular E_{RMS} measured at distance 0.5m for both ODAC samples is shown in figure 4.7d. The PLCC6 ODAC emitter exhibits

better uniformity than the blue ODAC emitter regarding the error curve shape. This is a consequence of larger blue ODAC front-end active area dimensions resulting in worse optical intensity uniformity displacement in the near field radiation area [24].

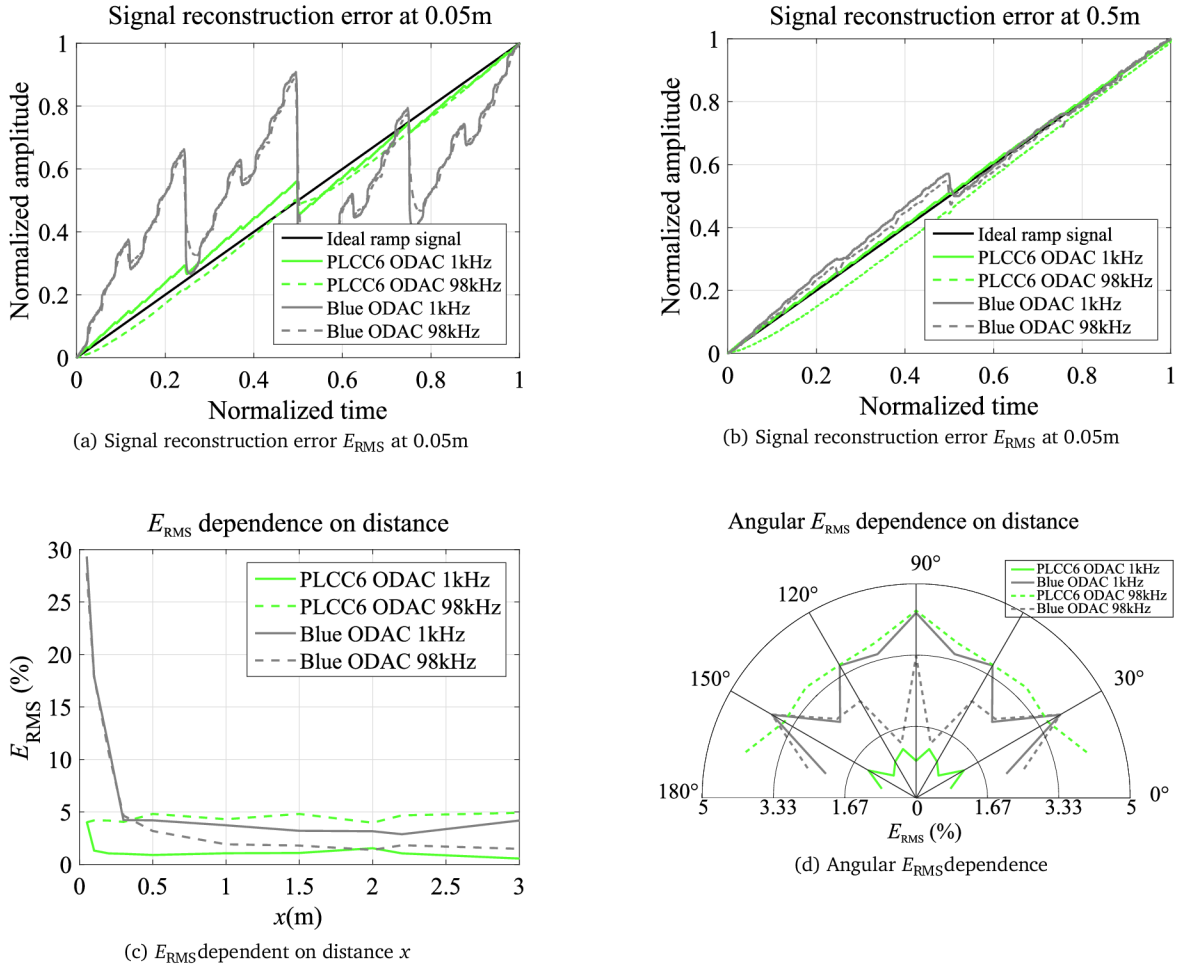


Figure 4.7: Dynamic signal reconstruction error

4.4 Channel impulse and frequency response

Frequency response can be considered as one of the key characteristics that implies overall VLC front-end performance. In conventional VLC applications the emitter is formed by a single LED or single LED array driven via a bias tee. In that case, the LED modulation bandwidth can be easily determined using a simple -3dB test. The bandwidth of an ASMT-YWB1-NGJB2 LED $B_{\text{PLCC6}-3\text{dB}}$ was merely 600kHz ascertained by a -3dB test. Since the ODAC concept has a fully digital input, the -3dB bandwidth test is not feasible anymore. In order to investigate the ODAC emitter frequency response, the time to frequency domain conversion was employed. In detail, the experiment had an identical set-up as in the previous case. The impulse signal (40ns width and period 100us) was experimentally determined as an optimal stimulus to drive the ODAC's LED groups. On the receiver side, CIR was captured.

As illustrates figure 4.8a the gray curve represents the blue ODAC emitter CIR. The green solid line and the green dashed line depict PLCC6 ODAC emitter CIRs for the non-filtered and blue-filtered signal, respectively.

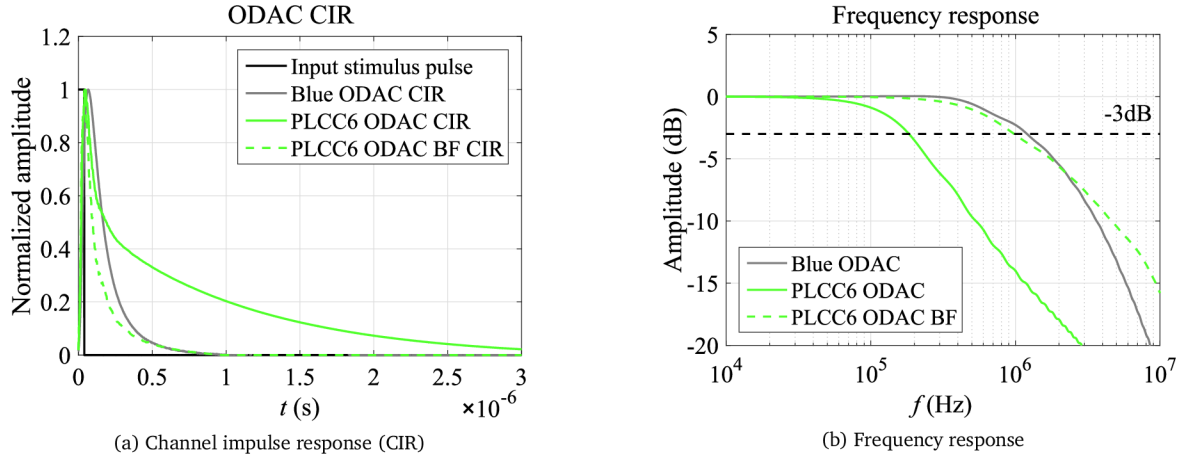


Figure 4.8: Channel impulse and frequency response

Used instruments

- Xilinx Virtex 6 ML605
- ODAC white PLCC6 LED front-end
- ODAC 7.62mm square blue LED front-end
- Optical receiver - FDS100 + TIA
- Tektronix TDS2000C
- Spectrometer Avaspec 3648
- Thermometer JUMO TDA300
- Ammeter Agilent 34405A
- Power supply Diametral P230R51D

The ODAC front-end frequency responses, illustrated in figure 4.8b, were obtained using MATLAB signal post processing based on the fast Fourier transform (FFT). The gray curve corresponds to the 1MHz blue ODAC emitter frequency response. The green solid curve illustrates PLCC6 ODAC emitter 200kHz frequency response. It should be noted that the ODAC-based front-ends exhibit worse bandwidth compared to the conventional LED front-end using a single LED chip (200kHz and 1MHz) [24].

In order to improve the bandwidth of the PLCC6 white LED front-end, an appropriate blue filter (BF) may be employed to suppress the slow yellow component. The following figure 4.9 depicts PLCC6 LED spectral characteristics for different forward currents 5mA, 10mA and 20mA, together with characteristics of blue filters under consideration. The BF

FB450/40 was chosen as the most suitable for further bandwidth investigation. Noticeably, the suggested BF improves the front-end bandwidth as illustrated in 4.8b. On the other hand, blue filtering implies significant optical power penalty [24].

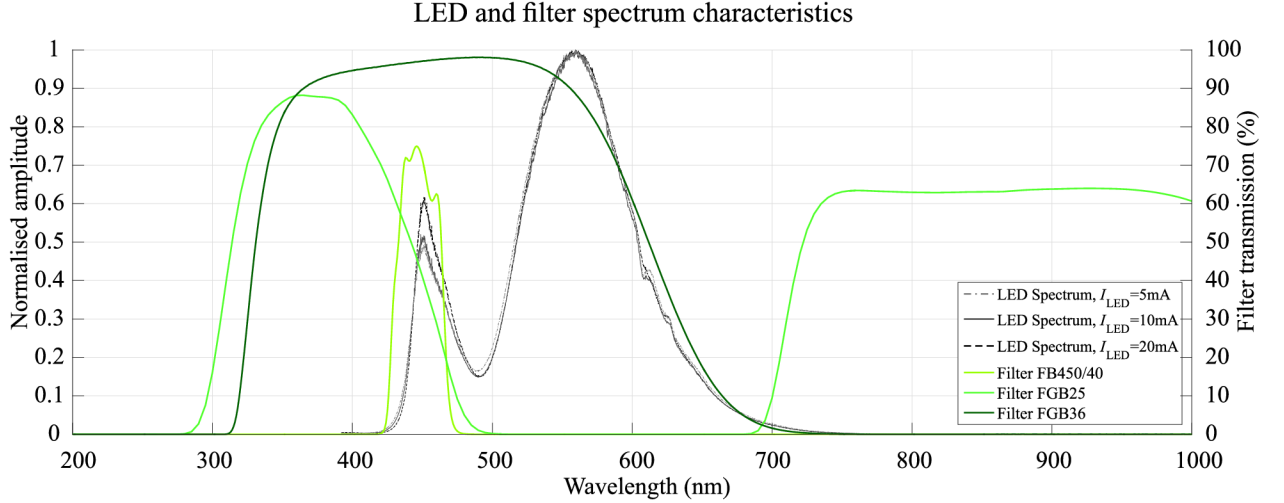


Figure 4.9: PLCC6 LED and filters optical spectrum characteristics

4.5 Linearity error performance

From the perspective of transfer function linearity, a conventional EDAC can be specified by integral non-linearity (INL) and differential non-linearity (DNL). Similarly, the same approach can be applied for ODAC specification. Integral non-linearity is defined as the maximum deviation at any point in the transfer function from an ideal characteristic which can be expressed by equation (4.3) [24]:

$$INL(t) = \frac{V_{Out}(t) - V_{Ideal}(t)}{V_{LSB}}, \quad (4.3)$$

where $V_{Out}(t)$ is voltage amplitude measured at the output of the optical receiver, $V_{Ideal}(t)$ is the ideal receiver voltage output amplitude, V_{LSB} denotes the voltage corresponding to 1LSB and t corresponds to the discrete time of input signal $v(t)$ sample [24].

Differential nonlinearity describes the maximum deviation of the actual and ideal (+1LSB) analog output step between two adjacent input codes as denotes equation (4.4). Moreover, when $DNL(t)$ exceeds -1LSB the DAC transfer function is non-monotonic [59].

$$DNL(t) = \frac{V_{Out}(t+1) - V_{Ideal}(t)}{V_{LSB}} - 1. \quad (4.4)$$

Unlike in EDAC, the linearity error in ODAC also depends on the geometrical set-up between the ODAC emitter and the optical receiver. In order to demonstrate how ODAC $INL(t)$ and $DNL(t)$ depend on geometrical considerations, the following graphs in figures 4.10, 4.11, 4.12 and 4.13 include additional information on the distance between the emitter and opti-

cal receiver. Figures 4.10 and 4.11 graphically represent $INL(t)$ and $DNL(t)$ of the 7.62mm square LED blue ODAC emitter. Apparently, $INL(t)$ dominates both signal frequencies. Needless to say, the highest $INL(t)$ is spread in front of the emitter due to optical intensity non-uniformity as was described formerly. The PLCC6 ODAC front-end shows better $INL(t)$ and $DNL(t)$ at lower frequencies (1kHz) as depicted in figure 4.12. As illustrated in figure 4.13, $INL(t)$ and $DNL(t)$ increase at higher frequencies (98kHz) is a result of PLCC6 LED bandwidth shortage [24].

Used instruments

- Xilinx Virtex 6 ML605
- ODAC white PLCC6 LED front-end
- ODAC 7.62mmblue LED front-end
- Optical receiver - FDS100 + TIA
- Tektronix TDS2000C
- Ammeter Agilent 34405A
- Power supply Diametral P230R51D

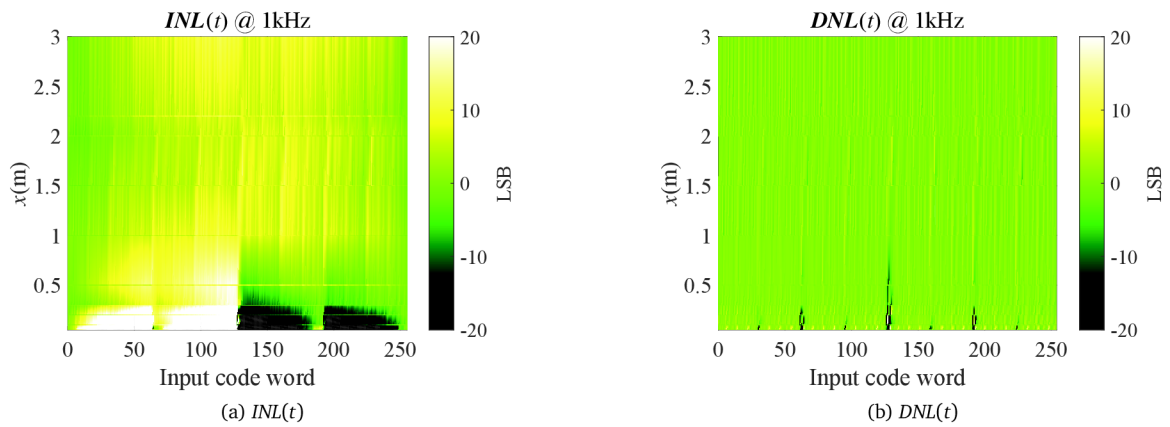


Figure 4.10: Blue 7.62mm LED ODAC front-end, $f = 1kHz$

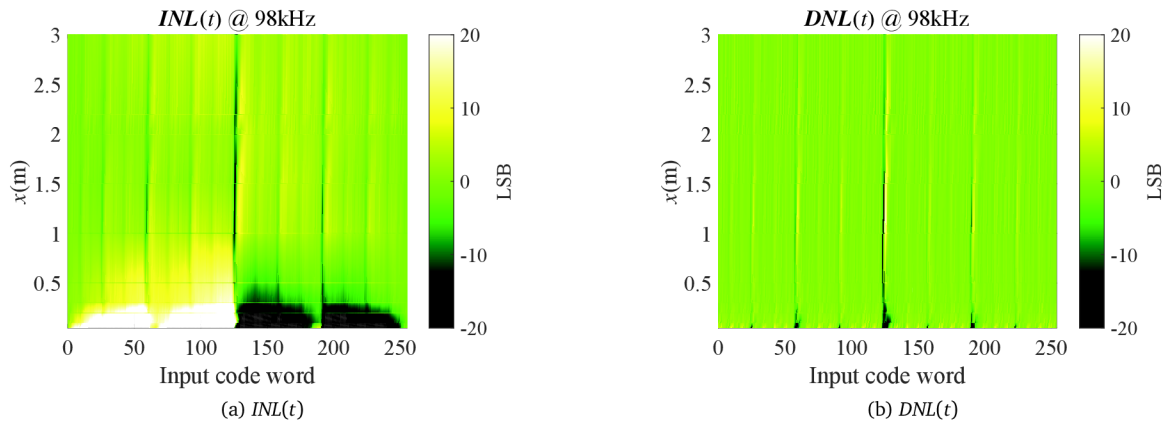


Figure 4.11: Blue 7.62mm LED ODAC front-end, $f = 98kHz$

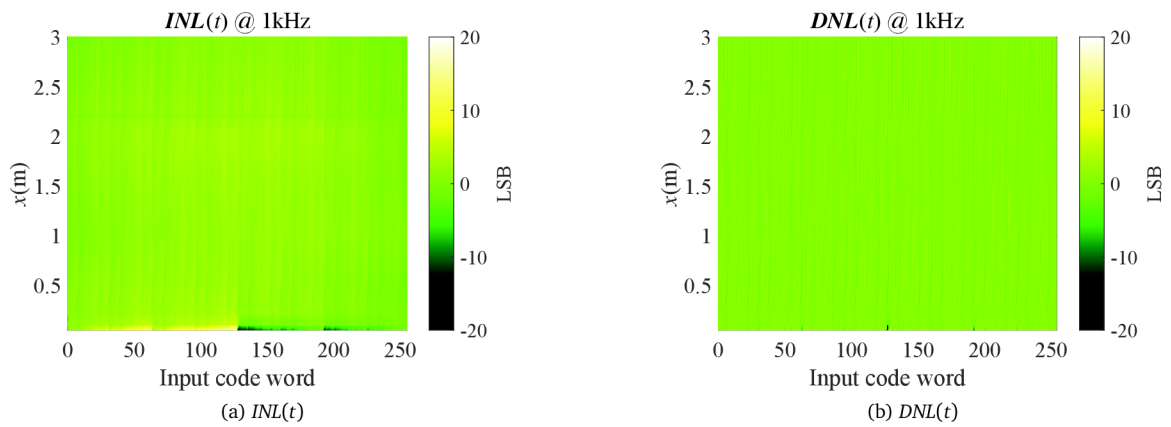


Figure 4.12: White PLCC6 LED ODAC front-end, $f = 1kHz$

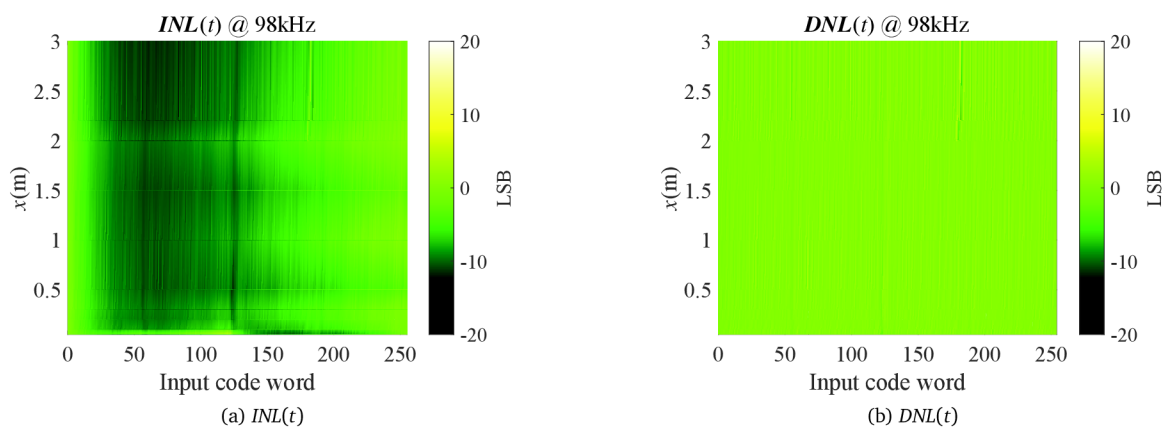


Figure 4.13: Blue 7.62mm LED ODAC front-end, $f = 98kHz$

4.6 Real time FPGA-based VLC system

Figure 4.14 shows an experimental test bed diagram of the real-time FPGA-based VLC system. The experimental setup included an FPGA-based configurable transceiver, an analog-to-digital converter (ADC) board, an 8-bit white PLCC6 LED ODAC emitter, a plano-convex lens, and a PIN PD receiver with configurable gain factors, as illustrated in figure 4.15.

The transceiver was able to generate DCO-OFDM signals with configurable bandwidth, allowing to evaluate performance for increasing data rates. The digital component of the communication system was implemented in a Xilinx Virtex-6 FPGA, while the AD conversion on the receiver side was implemented in an Analog Devices FCOMMS1 board, in a similar manner as described in [53] and used in [27].

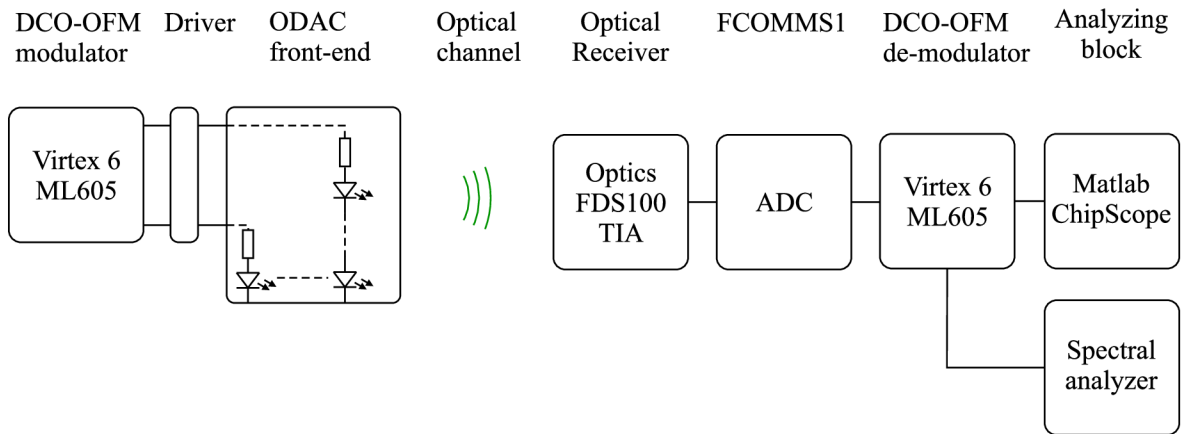


Figure 4.14: Real time FPGA-based OFDM VLC system set-up diagram

Each DCO-OFDM frame was composed of five OFDM symbols where the first one was a synchronization symbol. OFDM symbols included 1024 carriers where only 512 could be loaded (due to the Hermitian symmetry requirement). A cyclic prefix (CP) with 256 samples was appended to each OFDM symbol. Key transceiver's design and implementation parameters are given in table 2. Note that the signal bandwidth can be set either by changing the sample frequency (between 40MHz and 62MHz) or by changing the number of loaded sub-carriers. In these particular ODAC performance evaluation, the number of loaded sub-carriers was changed between 200 and 300 and the sample frequency between 50MHz and 62MHz, enabling to obtain DCO-OFDM signals with bandwidths between 10MHz and 15MHz.

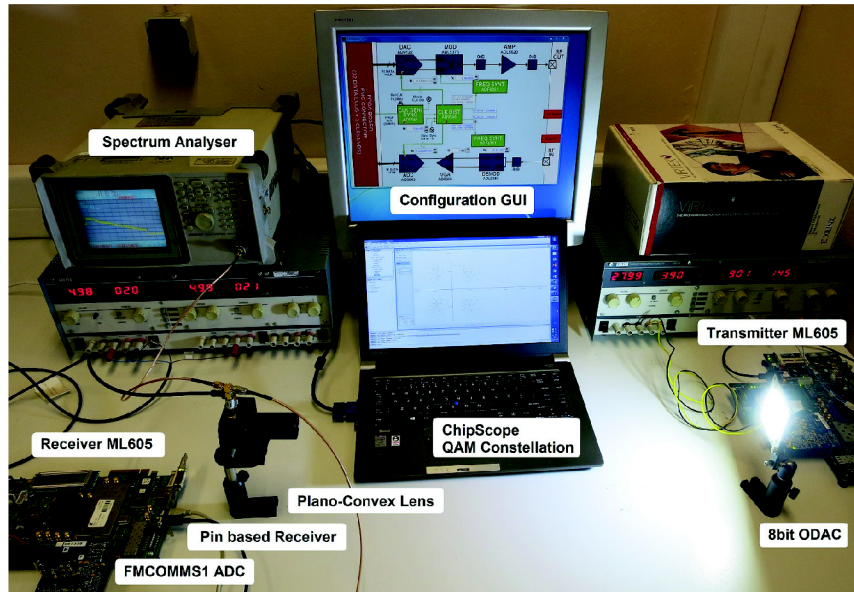


Figure 4.15: Experimental test bed

Used instruments

- 2x Xilinx Virtex 6 ML605
- Analog Devices FMCOMMS1 board
- ODAC white PLCC6 LED front-end
- Optical receiver - FDS100 + TIA
- Plano-convex lens (LA1422-A)
- KOBAN KL 1330 lux meter
- Spectrum analyzer Advantest U3641
- Powe supply Thurlby Thandar PL320QMT

Due to the AC coupled nature of the FMCOMMS1 board the low frequency carriers (carriers below 1MHz are not usable) were discarded and a band-pass synchronization sequence was designed. This sequence was implemented with a band-pass 64-tap linear feedback shift register (LFSR) pseudorandom noise (BPH-PN) sequence, with a configurable starting frequency and Hermitian symmetry. Moreover, it was designed to have an average transmitted power 3dB higher than the OFDM symbols to improve the system's timing synchronization performance.

Beyond bandwidth limitation, the proposed system (with 8-bit resolution) presents an additional challenge when used with high PAPR modulations, such as OFDM-based signals - its limited amplitude resolution. Thus, a trade off between clipping distortion and quantization noise had to be made. However, despite this clear disadvantage of OFDM-based signals, it is further shown that high-speed communication is still possible with this modulation scheme,

which is a trend followed in 5G networks and thus, should also be used in high-speed VLC for the sake of heterogeneous interoperability.

Design parameters	Implementation parameters
System Carriers	1024
Loaded Carriers	200-300
Pilot Carriers	50-75
Pilot separation	4
OFDM frame	5 symbols
Sync. Symbol	BPH_PN
CP length	256
Sample Frequency	50-62MHz
Clock Frequency	100MHz
Signal Bandwidth	10-15MHz
Carrier Separation	50-60kHz
Digital data width	32 bits
ODAC emitter resolution	8 bits
ADC resolution	14 bits

Table 2: Transceiver design and implementation parameters

ODAC performance with respect to high speed optical communication has been evaluated with an optical receiver with a plano-convex lens (LA1422-A). The received signal was fed to a 14-bit ADC and processed in the FPGA receiver. Figures 4.16a and 4.16b show the spectrum of the transmitted and received signals for the 30Mbps VLC system. The transmitted signal was obtained in the electrical domain, using a 16-bits DAC in parallel with the ODAC emitter under test, to observe the transmitted OFDM signal spectrum.

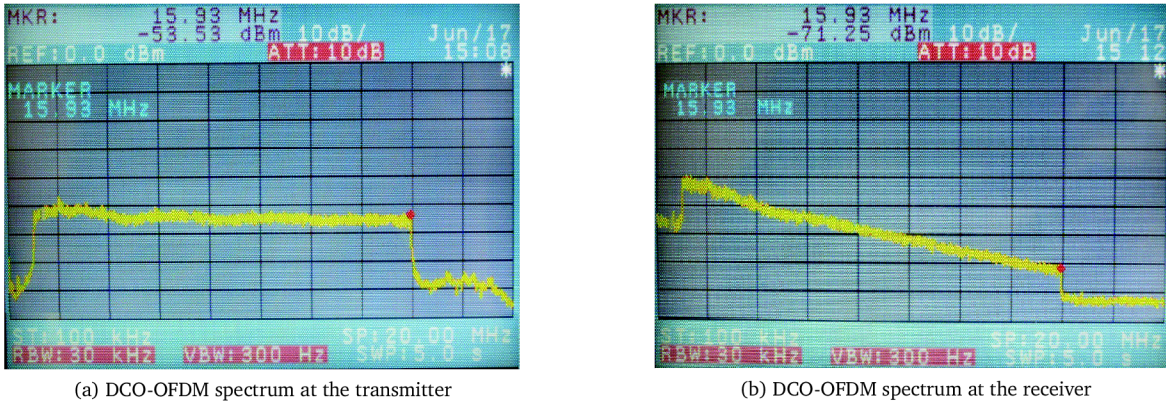


Figure 4.16: DCO-OFDM signal spectrums

The slightly higher transmitted power in the lower band of the OFDM spectrum was due to the synchronization sequence. Compared to the received spectrum (at 60cm from ODAC emitter), measured at the input of the ADC where the impact of the optical channel response could be observed, the received power difference between the first and last carrier was more than 30dB. Comparing this response with the LEDs' frequency response shown in figure 4.8b, it is reasonable to conclude that the channel response was mainly affected by the limited bandwidth of LEDs inside the front-end array.

Obviously, the SNR in upper band carriers was only about 10dB, which limited the achievable performance. Moreover, note that higher order constellations could have been used, but the OFDM bandwidth would have to be reduced accordingly (or the signal power increased

by reducing distances), and no further increase in performance would be achieved. Thus, a 4-QAM modulation was chosen, using a 15MHz bandwidth. In the digital domain, Xilinx ChipScope integrated logic analyzer (ILA) modules were used to measure the received constellation's *EVM* and obtain the data required to compute the system *BER* using an offline *BER* computation system.

Figure 4.17 shows *BER* results for increasing distances and transmitted data-rates. The figure also shows the forward error correction (FEC) limit boundary $3.8 \cdot 10^{-3}$. At shorter distances (less than 60cm), the receiver gain had to be reduced to avoid overcoming the ADC dynamic range which would result in signal clipping. The VLC system performance degraded with distance but still achieved over 19Mbps for distances compatible with the typical scenario where the luminaire is on the ceiling and the receiving devices are on a table top ($\approx 2.2\text{m}$). The maximum measured data rate was 30Mbps at 1m. Below 80cm, *BER* performance started getting affected by the ODAC emitter geometric distortion and receiver saturation in this arrangement due to the lens in the receiver, LEDs with high *HPA* and a PD with wide *FOV*. Using the same setup, distances and data-rates (figure 4.18), the received constellation's *EVM* was measured in order to infer the relationship between *BER* and *SNR*.

Figure 4.19 shows results which correlate with the measured illuminance E_v (using a KOBAN KL 1330 lux meter), for the 23.6Mbps scenario. As expected, illuminance decreased with the distance from the source and *EVM* deteriorated as distance increased. It is interesting to see the high absolute values of *EVM* which limited the overall system performance. Provided lower *EVM*, performance could be improved. This impairment results from distortion introduced by the driver arrangement, but also from the compromise between clipping distortion and quantization noise in the transmitter [28].

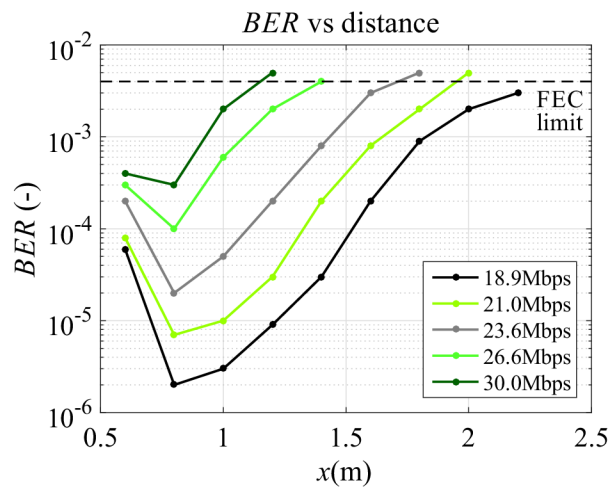


Figure 4.17: *BER* performance for increasing distances and bitrates

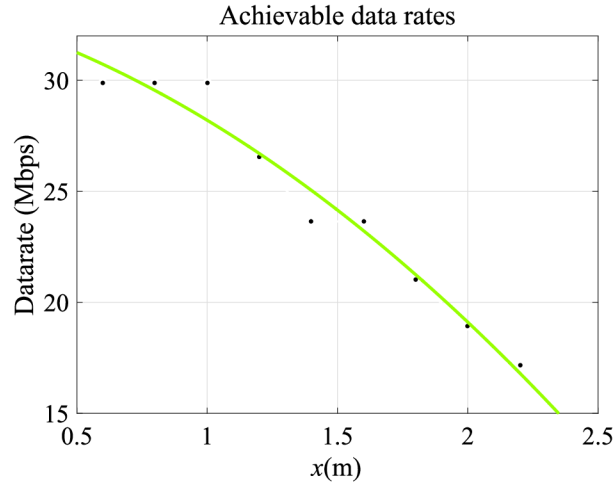


Figure 4.18: Achievable datarates for distances from 60cm to 220cm

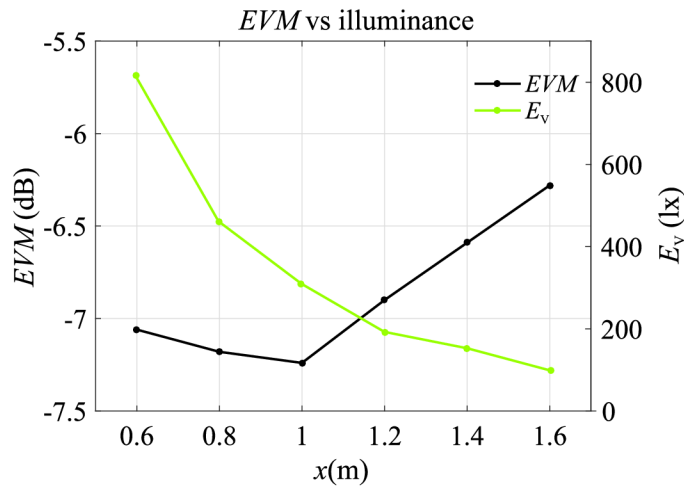


Figure 4.19: EVMs and measured illuminance E_v .

This compromise was evaluated experimentally by increasing the OFDM signal amplitude in the digital domain and measuring EVM . It was expected that higher amplitude levels would impose significant clipping distortion in the transmitted signal, while low amplitude levels would degrade the system performance due to the ODAC quantization noise. Results shown in figure 4.20 confirmed this expectation. The constellation's EVM decreased with increasing signal level only up to $3.3\sigma_{\text{OFDM}}$ ($C = 3.3$), where C is the clipping level and σ_{OFDM} is the mean standard deviation of OFDM samples. For higher clipping levels the system performance started to degrade due to quantization noise. This plot also shows that clipping impacted system performance more significantly than quantization noise, as expected from literature [64].

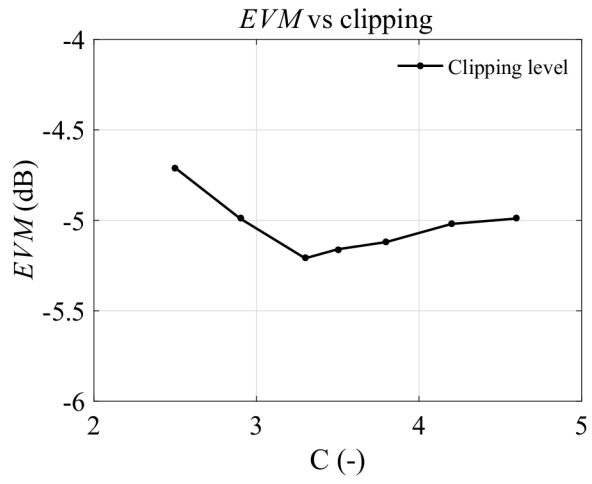


Figure 4.20: Compromise between *EVM* and clipping level at the transmitter

5 CONCLUSION

The doctoral thesis is focused on utilizing the optical D/A converter concept in optical wireless communication systems working in the area of visible light. Initially, the thesis outlines the essential introduction into VLC systems. The thesis summarizes possible types of VLC transmitters, describes particular types of receivers and presents an overview of modulations which may be utilized in VLC. In addition, the first chapter presents available channel modeling techniques suitable to characterize optical channel impairments in VLC systems.

The crucial part of the thesis is focused on optical channel modeling of the communication system employing the ODAC emitter as an appropriate alternative to the conventional VLC transmitter front-end. The proposed ODAC concept seems to be an ideal candidate to outperform the conventional approach of the transmitter front-end implementation in VLC systems. Provided an ODAC-based front-end is used, there is no need for an EDAC in the transmitter stage. Inherent LED nonlinearity is mitigated using this ODAC concept. Moreover, the ODAC concept architecture is in line with the recent trend of general lighting with respect to using multiple LED arrays.

The thesis looks into the influence of the ODAC emitter bit depth, emitter LED array topology, and the communication system geometrical arrangement as a paramount factor for the received signal quality. Furthermore, the thesis, for the first time, includes complex channel impulse response modeling of an ODAC-based VLC system, important for high data rate applications, including the first and second reflection contribution.

In the simulation part, the thesis explored several types of ODAC emitters having different topologies and dimensions. The greatest benefit of the work lies in a numerical model implemented in MATLAB able to model an optical channel of VLC systems employing the ODAC emitter on the transmitter side. The proposed channel modeling uses a deterministic ray model from the perspective of energy distribution over the channel. The thesis describes three different VLC system scenarios, in detail, with one reflection contribution ideal for slow data rates, the scenario assumes an ITS VLC system and an indoor VLC system comprising of four ODAC emitter arrays in an empty room.

In the experimental part, two ODAC functional samples were designed and implemented based on previous findings. In order to complete the VLC system for following performance evaluating, a wide-band optical receiver was developed particularly for this experimental part as well.

The ODAC-based VLC system performance is examined based on several tests. Specifically, static and dynamic signal reconstruction tests showed the ODAC emitter error performance in terms of geometrical and input signal frequency dependence. The results match expected simulation results and demonstrate typical increased signal distortion in front of the ODAC emitter. Furthermore, channel impulse response and frequency response for both

ODAC samples were explored. In order to investigate nonlinear error performance, the experimental part includes INL and DNL tests tailored especially for the ODAC-based VLC system. In other words, the tests included spatial dependence of both errors. Finally, the thesis presents, for the first time, real time an FPGA-based VLC system employing the ODAC emitter in the transmitter stage. VLC high data rate communication was demonstrated despite the ODAC emitter limited bandwidth.

All presented work has arisen based on close collaboration with the University of Aveiro. Thanks to this fruitful collaboration, several papers were published at high-level conferences and high impact journals. [20, 22, 23, 24, 21, 28].

BIBLIOGRAPHY

- [1] Lighting of indoor work places, 2002.
- [2] Traffic light signals. Technical and functional requirements. Part 1: Traffic light signals for traffic control. Printed, 1997.
- [3] Traffic light signals. Location and use of signal heads. Printed, March 1994.
- [4] Design of urban roads. Printed, January 2006.
- [5] JEITA CP-1221 Visible Light Commucation, 3 2007.
- [6] IEEE Standard for Local and metropolitan area networks-Part 15.7: Short-Range Wireless Optical Commucation Using Visible Light.
- [7] AHN, K.-I. – KWON, J. K. Color Intensity Modulation for Multicolored Visible Light Communications. *IEEE Photonics Technology Letters*. 2012, 24, s. 2254–2257.
- [8] ARMSTRONG, J. Optical domain digital-to-analog converter for visible light communications using LED arrays. *Photon*. August 2013, 1, 2, s. 92–95.
- [9] ARMSTRONG, J. OFDM for Optical Communications. *Journal of lightwave technology*. 2009, 27, s. 189–204.
- [10] BARRY, J. R. et al. Simulation of Multipath Impulse Response for Indoor Wireless Optical Channels. *IEEE Journal on selected areas in communications*. April 1993, 11, 3, s. 367–379.
- [11] BERMAN, S. et al. Human electroretinogram responses to video displays, fluorescent lighting, and other high frequency sources. *Optometry and Vision Science*. 1991, 68, s. 645–662.
- [12] BOUCHET, O. et al. *Free-Space Optics: Propagation and Communication*. ISTE Ltd, 2006.
- [13] BURTON, A. et al. Experimental Demonstration of 50-Mb/s Visible Light Communication Using 4x4 MIMO. *IEEE P*. 2014, 26, s. 945–948.
- [14] CARRUTHERS, J. B. – CARROLL, S. M. Statistical impulse response models for indoor optical wireless channels. *International Journal of Communications Systems*. March 2005, 18, 3, s. 267–284. doi: 10.1002/dac.703.
- [15] CARRUTHERS, J. B. – KAHN, J. M. Modeling of Nondirected Wireless Infrared Channels. *IEEE Transactions on Communications*. October 1997, 45, 10, s. 1260–1268.

- [16] CARRUTHERS, J. B. – KANNAN, P. Iterative Site-Based Modeling for Wireless Infrared Channels. *IEEE Transactions on Antennas and Propagation*. May 2002, 50, 5, s. 759–765.
- [17] HSIEH, C. – SHIU, D. Single Carrier modulation with frequency domain equalization for intensity modulation-direct detection channels with intersymbol interference. In *The 17th Annual IEEE International Symposium on Personal, Indoor and Mobile Radio Communications (PIMRC06)*, s. 1–5, 2006.
- [18] CHOW, C.-W. – CHEN, C.-Y. – CHEN, S.-H. Visible light communication using mobile-phone camera with data rate higher than frame rate. *Optics Express*. 2015, 23, 20, s. 1–6.
- [19] CREE. Cree First to Break 300 Lumens-Per-Watt Barrier. Technical report, Cree, Inc., 2014.
- [20] DOBESCH, A. – ALVES, L. N. – WILFERT, O. On the Performance of Digital to Analog Conversion in the Optical Domain for Low Data Rate Communications. In *Transparent Optical Networks (ICTON), 2014 16th International Conference*, s. 1–4, August 2014. doi: 10.1109/ICTON.2014.6876676.
- [21] DOBESCH, A. – ALVES, L. N. – WILFERT, O. Spatial ODAC performance for indoor environment. In *Optical Wireless Communications (IWOW), 2014 3rd International Workshop*, s. 1–5, September 2014. doi: 10.1109/IWOW.2014.6950779.
- [22] DOBESCH, A. et al. ODAC-based traffic lights for intelligent transport systems. In *26th Conference Radioelektronika 2016*, s. 1–5. IEEE, May 2016. doi: 10.1109/RADIOELEK.2016.7477401.
- [23] DOBESCH, A. et al. Optical Digital to Analog Conversion Performance Analysis for Indoor Set-up Conditions. *Optics Communications*. May 2017, 400, s. 115–122. doi: 10.1016/j.optcom.2017.05.021.
- [24] DOBESCH, A. et al. Performance analysis of 8-bit ODACs for VLC applications. *Radioen*. June 2017, 26, 2, s. 418–422. doi: 10.13164/re.2017.0418.
- [25] ELDOLED. Why you need dimming curves. Technical report, eldoLED B.V., 2016.
- [26] FATH, T. – HELLER, C. – HAAS, H. Optical Wireless Transmitter Employing Discrete Power Level Stepping. *Journal of Lightwave Technology*. June 2013, 31, 11, s. 1734–1743. doi: 10.1109/JLT.2013.2257984.
- [27] FIGUEIREDO, M. – ALVES, C. R. L. N. Live demonstration: 150Mbps+ DCO-OFDM VLC. In *Circuits and Systems (ISCAS)*, s. 457. IEEE, August 2016. doi: 10.1109/ISCAS.2016.7527275.

- [28] FIGUEIREDO, M. et al. Consumer LED lamp with ODAC technology for high-speed Visible Light Communications. *IEEE Transactions on Consumer Electronics*. Accepted for publication.
- [29] FUKUDA, T. – TANIGUCHI, Y. *Fast-Response Organic Light-Emitting Diode for Interactive Optical Communication*. INTECH, 2011.
- [30] GOTO, Y. et al. A New Automotive VLC System Using Optical Communication Image Sensor. *IEEE Photonics Journal*. June 2016, 8, 3, s. 1–17. doi: 10.1109/JPHOT.2016.2555582.
- [31] HAAS, H. et al. What is LiFi? *Journal of Lightwave Technology*. March 2015, 34, 6, s. 1–12. doi: 10.1109/JLT.2015.2510021.
- [32] HAIGH, P. A. et al. A multi-CAP visible light communications system with 4.85 b/s/Hz spectral efficiency. *IEEE Journal on Selected Areas in Communications*. May 2015, 33, 9, s. 1771–1779. doi: 10.1109/JSAC.2015.2433053.
- [33] HAUS, J. *Optical sensors*. WILEY-VCH Verlag GmbH & Co. KGaA, 2010.
- [34] HEROLD, M. – ROBERTS, D. Spectral characteristics of asphalt road aging and deterioration: implications for remote-sensing applications. *Applied Optics*. 2005, 44, 20, s. 4327–4334.
- [35] INAN, B. et al. Impact of LED Nonlinearity on Discrete Multitone Modulation. *IEEE/OSA Journal of Optical Communications and Networking*. September 2009, 1, 5, s. 439–450. doi: 10.1364/JOCN.1.000439.
- [36] ISLIM, M. S. – HAAS, H. Modulation Techniques for Li-Fi. *ZTE COMMUNICATIONS*. April 2016, 14, s. 29–40. doi: 10.3969/j.issn.1673.
- [37] JANG, Y. M. Current status of IEEE 802.15.7r1 OWC standardization. Technical report, Short-range optical wireless communications task group, 2015.
- [38] JUNGNICHEL, V. et al. A European View on the Next Generation Optical Wireless Communication Standard. In *Standards for Communications and Networking (CSCN)*, s. 106–111. IEEE, 2015. doi: 10.1109/CSCN.2015.7390429.
- [39] KAHN, J. M. – BARRY, J. R. Wireless infrared communications. *Proceedings of the IEEE*. 1997, 85, s. 265–298.
- [40] LEE, K. – PARK, H. Modulations for Visible Light Communications With Dimming Control. *IEEE Photonics Technology Letters*. May 2011, 23, 16, s. 3. doi: 10.1109/LPT.2011.2157676.

- [41] LO, S. et al. Channel Characterization for Indoor Visible Light Communications. In *Optical Wireless Communications (IWOW)*, s. 75–79. IEEE, 2014. doi: 10.1109/IWOW.2014.6950780.
- [42] LOPEZ-HERNANDEZ, F. – BETANCOR, M. DUSTIN: Algorithm for calculation of impulse response on IR wireless indoor channels. *Electronics letters*. October 1997, 33, 21, s. 1804–1806.
- [43] LOPEZ-HERNANDEZ, F. – PCREZ-JIMCNEZ, R. – SANTAMARIA, A. Monte Carlo calculation of impulse response on diffuse IR wireless indoor channels. *Electronics Letters*. June 1998, 34, 12, s. 1260–1262.
- [44] MCKENDRY, J. J. D. et al. Visible Light Communications Using a CMOS-Controlled Micro-Light-Emitting-Diode Array. *Journal of lightwave technology*. 2012, 30, s. 61–67.
- [45] MENEGHINI, M. et al. Degradation Mechanisms of High-Power LEDs for Lighting Applications: An Overview. *IEEE Transactions on Industry Applications*. 2014, 50, s. 78–85. doi: DOI:10.1109/TIA.2013.2268049.
- [46] MORGAN, F. Gauging the lifetime of an LED. Technical report, Digital Lumens, 2012.
- [47] MUKISH, P. – ROSINA, M. – BOULAY, P. OLED for Lighting. Technical report, Yole développement, 2016.
- [48] OKON, T. M. – BIARD, J. R. The First Practical LED. Technical report, Edison Tech Center, 2015.
- [49] PEREZ-JIMENEZ, R. – BERGES, J. – BETANCOR, M. Statistical model for the impulse response on infrared indoor diffuse channels. *Electronics Letters*. July 1997, 33, 15, s. 1298–1300. doi: 10.1049/el:19970866.
- [50] PROAKIS, J. – SALEHI, M. *Digital Communications*. McGraw-Hill Education, 5th edition, 2007.
- [51] RANJHA, B. – KAVEHRAD, M. Hybrid Asymmetrically Clipped OFDM-Based IM/DD Optical Wireless System. *IEEE/OSA Journal of Optical Communications and Networking*. 2014, 6, s. 387–396. doi: 10.1364/JOCN.6.000387.
- [52] RAZAVI, B. *Design of analog CMOS integrated circuits*. McGraw-Hill Education, 1 edition, August 2000.
- [53] RIBEIRO, C. – FIGUEIREDO, M. – ALVES, L. N. A Real-Time Platform for Collaborative Research on Visible Light Communication. In *Optical Wireless Communications (IWOW)*, s. 112–116. IEEE, 2015. doi: 10.1109/IWOW.2015.7342277.
- [54] SADIKU, M. N. O. *Optical and wireless Commucations*. CRC Press LLC, 2002.

- [55] SALAMANDRA, L. et al. Time-Resolved Response of Polymer Bulk-Heterojunction Photodetectors. *IEEE Photonics Technology Letters*. 2011, 23, 12, s. 780–782. doi: 10.1109/LPT.2011.2124451.
- [56] SARBAZI, E. – UYSAL, M. Ray Tracing Based Channel Modeling for Visible Light Communications. In *Signal Processing and Communications Applications Conference (SIU)*, s. 702–705. IEEE, 2014. doi: 10.1109/SIU.2014.6830326.
- [57] TANAKA, Y. – HARUYAMA, S. – NAKAGAWA, M. Wireless optical transmissions with white colored LED for wireless home links. In *Personal, Indoor and Mobile Radio Communications*, 2, s. 1325–1329, 2000. doi: 10.1109/PIMRC.2000.881634.
- [58] UEMOTO, K. L. – SATO, N. M. N. – JOHN, V. M. Energy and Buildings. *International Conference on Building Energy and Environment*. 2010, 42, s. 17/22.
- [59] BOSCH, A. – STEYAERT, M. – SANSEN, W. *Static and Dynamic Performance Limitations for High Speed D/A Converters*. Springer Science & Business Media, 2004.
- [60] WANG, P. et al. A Few Key Technologies of Quantum Dot Light-Emitting Diodes for Display. *IEEE Journal of Selected Topics in Quantum Electronics*. September/October 2017, 23, 5, s. 1–12. doi: 10.1109/JSTQE.2017.2665779.
- [61] WILLTEK. EVM measurement design for 3G test equipment. Technical report, EVM measurement design for 3G test equipment, 2003.
- [62] XIANSONG, F. et al. Design and Properties Analysis of a Single-chip White InGaN/GaN LED. In *Mechanical and Electrical Technology (ICMET)*, s. 413–416. IEEE, 2010. doi: 10.1109/ICMET.2010.5598465.
- [63] XIAO, X. et al. Utilizing CdSe/ZnS Core/Shell QDs to Improve the Modulation Bandwidth of WLED for Visible Light Communication. In *Electronic Packaging Technology (ICEPT)*. IEEE, 2016. doi: 10.1109/ICEPT.2016.7583352.
- [64] YEW, J. – DISSANAYAKE, S. D. – ARMSTRONG, J. Performance of an experimental optical DAC used in a visible light communication system. In *Globecom Workshops (GC Wkshps)*, s. 1110–1115. IEEE, 2013. doi: 10.1109/GLOCOMW.2013.6825141.
- [65] ZHANG, S. et al. 1.5 Gbit/s Multi-Channel Visible Light Communications Using CMOS-Controlled GaN-Based LEDs. *Journal of Lightwave Technology*. April 2013, 31, 8, s. 1211–1216. doi: 10.1109/JLT.2013.2246138.

Nomenclature

Acronyms A

ACO-OFDM	Asymmetrically Clipped Optical OFDM
ADC	Analog to digital converter
APD	Avalanche Photo Diode
AWG	Arbitrary Waveform Generator
BF	Blue Filter
BPH-PN	Pseudorandom Noise
CdSe	Cadmium Selenide
CIM	Color Intensity Modulation
CIR	Channel Impulse Response
COB	Chip on Board
CP	Cyclic Prefix
CSK	Color Shift Keying
DAC	Digital to Analog Converter
DCO-OFDM	DC Biased Optical OFDM
DFE	Nonlinear Decision Feed-back Equalizers
DFT	Discrete-time Fourier Transform
DMT	Discrete Multi Tone
DNL	Differential Non-linearity
EDAC	Electrical Digital to Analog Converter.
EVM	Error Vector Magnitude
FDE	Frequency Domain Equalizer
FEC	Forward Error Correction
FFE	Feed Forward Equalizer
FFT	Fast Fourier Transform
FIR	Finite Impulse Response
FOV	Field of View
FPGA	Field Programmable Gate Array
FSK	Frequency Shift Keying
FSO	Free Space Optics
HPA	Half Power Angle

I2V	Infrastructure to Vehicle
IFFT	Inverse Fast Fourier Transform
ILA	Integrated Logic Analyzer
IM/DD	Intensity Modulation/Direct Detection
INL	Integral Non-linearity
IR	Infra Red
ISC	Image Sensor Communication
ISI	Intersymbol Interference
ITS	Intelligent Transportation System
LED	Light Emitting Diode
LFSR	Linear Feedback Shift Register
Li-Fi	Light Fidelity
LoS	Line of Sight
LSB	Least Significant Bit
m-CAP	Multi-band Carrier-less Amplitude and Phase
MFTP	Maximum Flickering Time Period
MIMO	Multiple In Multiple Out
mLED	Micro LED
MLSD	Maximum Likelihood Sequence Detection
MOCVD	Cerium-doped Yttrium aluminum garnet
MSB	Most Significant Bit
OCI	Optical Communication Image
ODAC	Optical Digital to Analog Conversion
OFDM	Orthogonal Frequency Division Multiplexing
OLED	Organic Light Emitting Diode
OOK	On-Off Keying
OPD	Organic Photo Diode
OWC	Optical Wireless Communication
PAM	Pulse Amplitude Modulation
PAPR	Peak to Average Power Ratio
PCB	Printed Circuit Board
PD	Photo Diode

PLED	Polymer LED
PPM	Pulse Position Modulation
PWM	Pulse Width Modulation
QLEDs	Quantum dots LED
SMOLED	Small Molecule LED
SSL	Solid State Lighting
TIA	Transimpedance Amplifier
U-OFDM	Unipolar OFDM
VLC	Visible Light Communication
VLCC	Visible Light Communication Consortium
VPANs	Visible-Light Personal Area Networks
VPPM	Variable Pulse Position Modulation
WDM	Wavelength Division Multiplex
YAG	Cerium-doped Yttrium Aluminum Garnet
Symbols	S
α	Angle of incidence
β	Angle of reflection
Δt	Minimum time delay (time resolution)
Δt_{LoS}	Direct path time delay
Δt_{Ref1}	The first order reflection time delay
Δt_{Ref2}	The second order reflection time delay
$\delta()$	Dirac delta function
$DNL(t)$	Differential non-linearity
$INL(t)$	Integral non-linearity
$V_{\text{Ideal}}(t)$	Ideal receiver voltage output amplitude
$V_{\text{Out}}(t)$	Measured voltage amplitude
ΔA	Surface differential element
G_{Ref1}	Number of grid elements for the first reflection order
G_{Ref2}	Number of grid elements for the second reflection order
μ	Mean excess delay
$\bar{v}(t)$	Normalized signal replica
ϕ	Transmitter viewing angle




ψ	Receiver viewing angle
ρ	Reflection coefficient
σ_{OFDM}	Mean standard deviation of OFDM samples
σ_{EVM}^2	EVM variance
$\theta_{1/2}$	Half power angle
$\vec{d}_{\text{Rx}}^{\text{Ref2}}$	Second reflection to receiver direction
\vec{d}_{Rx}	Transmitter to receiver direction
\vec{n}_{Ref}	Reflection Normal Vector
$\vec{d}_{\text{I}}^{\text{Ref1}}$	Incident direction of the first order reflection
$\vec{d}_{\text{I}}^{\text{Ref2}}$	Incident direction of the second order reflection
$\vec{d}_{\text{Rx}}^{\text{Ref1}}$	First reflection to receiver direction
\vec{n}_{Rx}	Receiver normal vector
\vec{n}_{Tx}	Emitter Normal Vector
A_{Rx}	Photodetector active area
$B(t)$	Set of digital bitstreams
$B_{\text{PLCC6-3dB}}$	PLCC6 white LED bandwidth
BER	Bit error ratio
C	Clipping level
D	Near field area boundary
D_{RMS}	Channel RMS delay spread
E_{V}	Illuminance
E_{RMS}	Relative RMS error
FOV	Receiver field of view
$g(\psi)$	Concentrator gain
H	DC channel gain
$h(t)$	Channel Impulse Response
$h^{(r)}(t)$	Multipath CIR
$h^{\text{LoS}}(t)$	Direct path CIR
H^{LoS}	Direct path DC channel gain
H^{Ref1}	First order reflection path DC channel gain
$h^{\text{Ref1}}(t)$	First order reflection CIR contribution
H^{Ref2}	Second order reflection path DC channel gain

$h^{\text{Ref}2}(t)$	First order reflection CIR contribution
H_{Rx}	Receiver general function
H_{G}	General DC channel gain
h_{Rx}	Receiver Height
h_{Tx}	Transmitter height
$H_{f-3\text{dB}}$	Channel cut of frequency
H_f	Channel frequency response
H_{Tx}	Transmitter general function
I_0	Radiant Intensity
$I_{\text{Tx}}(\theta)$	Radiant intensity pattern
n	Directivity index
n_0	Noise contribution
n_{Err}	Number of error bits
n_{Total}	Total number of bits
P_0	Total optical power
P_n	Noise power level
P_{Sig}	Signal power level
P_{Tx}	Optical power emitted by an LED
r_d	Percentage of incident signal reflected diffusely
R_{Lambert}	Lambertian reflection model
R_{PD}	Photodiode responsivity
R_{Phong}	Phong reflection model
R_{Vega}	Ophir Vega responsivity
$rect(x)$	FOV bounding function
s	LED array dimension
SNR	Signal to noise ratio
T	Signal Period
t	Discrete time
$T(\psi)$	Filter transmission
$v(t)$	Normalized original signal
V_{LSB}	Voltage amplitude corresponding to 1LSB
a	Number of transmitter arrays

k	Number of LED groups in the ODAC array
M	Data length
m	LED array group index
n	Number of LEDs in each LED group
R	Reference signal
r	Reflection order index
s1	Number of reflection surfaces for the first reflection order
s2	Number of reflection surfaces for second reflection order
Z	Measured signal

A CURRICULUM VITAE

Ales Dobesch

 16.3.1989
 00420 541 14 6558
 xdobes05@stud.feec.vutbr.cz

Research interests

Visible light communication with special emphasis on optical channel modeling, transmitter and receiver hardware design. Free space optical communication with focus on hardware design and implementation.

Education

- Since 09/2013 Brno University of Technology, Brno, Czech Republic
- Doctor of Philosophy (Ph.D.), Electronics and Communication
 - An optical D/A converter for VLC applications
- 09/2011 - 06/2013 Brno University of Technology, Brno, Czech Republic
- Master's degree (Ing.), Electronics and Communication
 - IR Thermometer with Automatic Emissivity Correction
 - Dean's award
- 09/2008 - 06/2011 Brno University of Technology, Brno, Czech Republic
- Bachelor's (Bc.) degree: Radioelectronics
 - Design and Realization of D Class Audio Amplifier Controlled by Microcontroller
 - Dean's award

Academic appointments

- Since 09/2013 Department of Radioelectronics, Brno University of Technology
- Since 09/2013 Sensor, Information and Communications Systems (SIX) research group

Research stays

- 1/2014 - 2/2014 Short Time Scientific Mission within COST IC1101 project University of Aveiro, Portugal.
- Optical channel modeling of the ODAC concept
 - Supervised by: Prof. Luis Nero Alves
- 11/2015 - 12/2015 Internship within University of Leiria, Portugal.
- Real time FPGA-based VLC communication system
 - Supervised by: Prof. Luis Nero Alves, Prof. Carlos Gaspar Ribeiro, Monica de Figueiredo

Computer skills

- Matlab, Simulink, C/C++, VHDL
- Microsoft office, LYX, LaTeX
- CorelDraw Suite, Adobe Photoshop
- AutoCAD, PSPICE, Eagle CADsoft
- Labview, AVR Studio, VEE Agilent

Languages

- Czech - Native speaker
- English - Upper intermediate
- German - Intermediate

B LIST OF PUBLICATIONS

2017

FIGUEIREDO, M.; RIBEIRO, C.; DOBESCH, A.; ALVES, L.; WILFERT, O.; Consumer LED lamp with ODAC technology for high-speed Visible Light Communications. IEEE Transactions on Consumer Electronics, 2017, Conditionally accepted for publication.

DOBESCH, A.; ALVES, L.; WILFERT, O.; RIBEIRO, C. Optical Digital to Analog Conversion Performance Analysis for Indoor Set-up Conditions. Optics Communications, 2017, č. 400C, s. 115-122. ISSN: 0030-4018.

DOBESCH, A.; FIGUEIREDO, M.; ALVES, L.; WILFERT, O. Performance analysis of 8-bit ODACs for VLC applications. Radioengineering, 2017, roč. 2017, č. 2, s. 418-422. ISSN: 1210-2512.

DOBESCH, A.; JANÍK, L.; NOVÁK, M.; WILFERT, O.; ALVES, L.; RIBEIRO, C. On Real Time VLC Channel Emulators. In 18th Conference on Microwave Techniques COMITE 2017. Brno: 2017. s. 1-5. ISBN: 978-1-5090-4594-5.

JANÍK, L.; NOVÁK, M.; DOBESCH, A.; HUDCOVÁ, L. Retroreflective Optical Communication. In 18th Conference on Microwave Techniques COMITE 2017. Brno: 2017. s. 1-4. ISBN: 978-1-5090-4594-5.

2016

DOBESCH, A.; ALVES, L.; WILFERT, O.; RIBEIRO, C. ODAC-based traffic lights for intelligent transport systems. In Proceedings of the 26th International Conference RADIOELEKTRONIKA 2016. Košice, Slovakia: Department of Electronics and Multimedia Communications, 2016. s. 345-349. ISBN: 978-1-5090-1673-0. (The best student paper award)

JANÍK, L.; NOVÁK, M.; HUDCOVÁ, L.; WILFERT, O.; DOBESCH, A. LwIP Based Network Solution for MicroBlaze. In Proceedings of the 2016 International Conference on Broadband Communications for Next Generation networks, and Multimedia Applications. Graz university of technology, Institute of Microwave and Photonic Engineering, Inffeldgasse 12/ I, 8010 Graz, AUSTRIA: Graz University of Technology, 2016. s. 1-4. ISBN: 978-1-5090-2269-4.

NOVÁK, M.; JANÍK, L.; HUDCOVÁ, L.; WILFERT, O.; DOBESCH, A. Improvement of Bit Error Rate in Free Space Optical Link. In 2016 International Conference on Broadband Communications for Next Generation Networks, and Multimedia Applications. Graz: Graz University of Technology, 2016. s. 1-4. ISBN: 978-1-5090-2269-4.

2015

WILFERT, O.; BARCÍK, P.; DOBESCH, A.; PAVLŮ, M. Nové trendy v oblasti bezkabelové komunikace. In XXV konference, Radiokomunikace, sborník přednášek. říjen 2015. Pardubice: UNIT s.r.o., 2015. s. 169-183. ISBN: 978-80-905345-6-8.

WILFERT, O.; KOLKA, Z.; BARCÍK, P.; DOBESCH, A.; PAVLŮ, M. The use of photonic technology in optical wireless links. In 14th Conference on Microwave Techniques, COMITE 2015. 2015. s. 135-138. ISBN: 978-1-4799-8121-2.

WILFERT, O.; BARCÍK, P.; DOBESCH, A. Současný stav a perspektivy optické bezkabelové komunikace. In 43. Seminář Pravidelné setkání zájemců o mikrovlnnou techniku. Praha: Česká elektrotechnická společnost, z. s., ÚOS Mikrovlnná technika, 2015. s. 1-4. ISBN: 978-80-02-02627- 3.

2014

DOBESCH, A.; ALVES, L.; WILFERT, O. Spatial ODAC performance for indoor environment. In 3rd International Workshop in Optical Wireless Communications (IWOW). Funchal, Madeira Island, Portugal: 2014. s. 70-74. ISBN: 978-1-4799-6676- 9.

DOBESCH, A.; ALVES, L.; WILFERT, O. On the Performance of Digital to Analog Conversion in the Optical Domain. In Proceedings of the 16th International Conference on Transparent Optical Networks ICTON 2014. Warsaw, Poland: National Institute of Telecommunications, 2014. s. 1-4. ISBN: 978-1-4799-5600- 5.

HUDCOVÁ, L.; WILFERT, O.; DOBESCH, A. Interferometric method for the relative variance of the optical power measurement. In Proceedings of the 24th International Conference Radioelektronika 2014. Bratislava: Slovak University of Technology, 2014. s. 1-4. ISBN: 978-1-4799-3714- 1.

2013

DOBESCH, A.; POLIAK, J. IR Thermometer with Automatic Emissivity Correction. Radioengineering, 2013, roč. 22, č. 4, s. 1301-1306. ISSN: 1210- 2512.

C LIST OF RESEARCH PRODUCTS

DOBESCH, A.: ODAC; 8bitový optický digitálně analogový převodník. Fyzicky je spoj umístěn na VUT v Brně. Adresa: Vysoké učení technické v Brně, FEKT, UREL, Technická 12, 616 00 Brno, Česká republika.

DOBESCH, A.; WILFERT, O.: VLC přijímač; Optický přijímač pro VLC aplikace. Fyzicky je VLC přijímač umístěn na VUT v Brně. Adresa: Vysoké učení technické v Brně, FEKT, UREL, Technická 12, 616 00 Brno, Česká republika.

KOLKA, Z.; KINCL, Z.; BIOLKOVÁ, V.; WILFERT, O.; POLIAK, J.; DOBESCH, A.; BIOLEK, D.: FSO; Optický bezdrátový spoj. Fyzicky je spoj umístěn na VUT v Brně. Adresa: Vysoké učení technické v Brně, FEKT, UREL, Technická 12, 616 00 Brno, Česká republika.

KOLKA, Z.; BIOLKOVÁ, V.; WILFERT, O.; DOBESCH, A.; BARCÍK, P.; NOVÁK, M.: EPCOM FSO- IDU; Vnitřní jednotka fotonického bezvláknového spoje. Fyzicky je jednotka umístěna na VUT v Brně. Adresa: Vysoké učení technické v Brně, FEKT, UREL, Technická 12, 616 00 Brno, Česká republika.